

A comparison between short GRB afterglows and kilonova AT2017gfo: shedding light on kilonovae properties

A. Rossi^{1,2}, G. Stratta^{1,3}, E. Maiorano¹, D. Spighi¹, N. Masetti^{1,4}, E. Palazzi¹, A. Gardini⁵, A. Melandri⁶, L. Nicastro¹, E. Pian¹, M. Branchesi⁷, M. Dadina¹, V. Testa², S. Brocato^{2,8}, S. Benetti⁹, R. Ciolfi^{9,10}, S. Covino⁶, V. D’Elia^{11,2}, A. Grado¹², L. Izzo⁵, A. Perego¹³, S. Piranomonte², R. Salvaterra¹⁴, J. Selsing¹⁵, L. Tomasella⁹, S. Yang⁹, D. Vergani¹, L. Amati¹, J. B. Stephen¹,
on behalf of the Gravitational Wave Inaf TeAm (GRAWITA),

¹INAF - Osservatorio di Astrofisica e Scienza dello Spazio, via Piero Gobetti 93/3, 40129 Bologna, Italy

²INAF - Osservatorio Astronomico di Roma, via Frascati 33, 00040 Monte Porzio Catone, Italy

³INFN-Firenze, via Sansone 1, I-50019, Firenze, Italy

⁴Departamento de Ciencias Físicas, Universidad Andrés Bello, Fernández Concha 700, Las Condes, Santiago, Chile

⁵Instituto de Astrofísica de Andalucía (IAA-CSIC), Glorieta de la Astronomía s/n, E-18008 Granada, Spain

⁶INAF - Osservatorio Astronomico di Brera, Via E. Bianchi 46, I-23807, Merate (LC), Italy

⁷Gran Sasso Science Institute, Viale F. Crispi 7, I-67100 L’Aquila, Italy

⁸INAF - Osservatorio Astronomico d’Abruzzo, Via M. Maggini snc, I-64100 Teramo, Italy

⁹INAF - Osservatorio Astronomico di Padova, Vicolo dell’Osservatorio 5, I-35122 Padova, Italy

¹⁰INFN-TIFPA, Trento Institute for Fundamental Physics and Applications, via Sommarive 14, I-38123 Trento, Italy

¹¹ASI-Science Data Center, via del Politecnico snc, 00133 Rome, Italy

¹²INAF - Osservatorio Astronomico di Capodimonte, salita Moiariello 16, I-80131 Napoli, Italy

¹³Università degli Studi di Milano-Bicocca, Piazza dell’Ateneo Nuovo, 1 - 20126, Milano, Italy

¹⁴INAF, Istituto di Astrofisica Spaziale e Fisica Cosmica di Milano, via E. Bassini 15, I-20133 Milano, Italy

¹⁵Dark Cosmology Centre, Niels Bohr Institute, Juliane Maries Vej 30, 2100 Copenhagen Ø, Denmark

Accepted XXX. Received YYY; in original form ZZZ

ABSTRACT

Multi-messenger astronomy received a great boost following the discovery of kilonova AT2017gfo, the optical counterpart of the gravitational wave source GW170817 associated with the short gamma-ray burst GRB 170817A. AT2017gfo was the first kilonova that could be extensively monitored in time both photometrically and spectroscopically. Previously, only few candidates have been observed against the glare of short GRB afterglows. In this work, we aim to search the fingerprints of AT2017gfo-like kilonova emissions in the optical/NIR light curves of 39 short GRBs with known redshift. For the first time, our results allow us to study separately the range of luminosity of the blue and red components of AT2017gfo-like kilonovae in short GRBs. In particular, **the red component is similar in luminosity to AT2017gfo**, while the blue kilonova can be more than 10 times brighter. **Finally, we find further evidence to support all the claimed kilonova detections and we exclude an AT2017gfo-like kilonova in GRBs 050509B and 061201.**

Key words: gamma-ray burst: general, gravitational waves, stars: neutron

1 INTRODUCTION

Gamma-ray bursts (GRBs) are divided in two populations consisting of long and short GRBs (e.g., Kouveliotou et al. 1993). Long GRBs (i.e. GRBs with a burst duration longer

than ~ 2 s) have been conclusively linked to the explosive deaths of massive stars (e.g., Hjorth et al. 2003). For a long time only indirect evidence associated short GRBs to the merging of compact objects, however a watershed occurred after the simultaneous detection of the gravitational

wave (GW) source GW170817 (Abbott et al. 2017a) by aLIGO/AdVirgo (LIGO Scientific Collaboration et al. 2015; Acernese et al. 2015) and the short GRB 170817A (Goldstein et al. 2017; Savchenko et al. 2017; Abbott et al. 2017c). Their identification with the same astrophysical source has provided the first direct evidence that at least a fraction of short GRBs is associated with the merging of two neutron stars (NSs). At the same time, the discovery of the optical counterpart of GW170817, AT2017gfo (Coulter et al. 2017), and its identification with the elusive “kilonova” (KN) emission (e.g., Li & Paczyński 1998; Metzger et al. 2010), has indirectly told us that these poorly sampled astrophysical phenomena can potentially be detected as a possible additional component to the optical and near-infrared (NIR) afterglow of (nearby) short GRBs in the temporal window that goes from about a few hours to a few weeks after the onset of the burst (e.g., Kasen et al. 2015; Barnes et al. 2016; Fernández & Metzger 2016; Metzger 2017).

AT2017gfo was discovered during its brightening phase at ~ 11 hours after the gravitational wave event (Coulter et al. 2017) and was followed up by several groups both photometrically and spectroscopically in the optical and NIR bands (Andreoni et al. 2017; Arcavi et al. 2017; Covino et al. 2017; Chornock et al. 2017; Drout et al. 2017; Evans et al. 2017; Pian et al. 2017; Smartt et al. 2017; Tanvir et al. 2017; Drout et al. 2017; Kasliwal et al. 2017a; Troja et al. 2017). This enormous observational effort, well summarised in Abbott et al. (2017b), allowed several of these groups to recognise a thermal emission in the data, with a black-body temperature evolving from ~ 7300 K at ~ 0.6 days (Evans et al. 2017) to ~ 5000 K at 1.5 days after the GW event (Pian et al. 2017; Smartt et al. 2017). At ~ 6 days, the maximum moved to the longer wavelengths peaking in the J band, indicating rapid cooling. This behaviour was markedly different not only from an afterglow but also from a supernova event. Instead, both the light curve evolution and the early (< 15 days) spectra nicely matched the expected kilonova modelling, i.e. a thermal emission powered by the radioactive decay of elements formed via r-process nucleosynthesis in the ejecta of the NS-NS merger (e.g., Kasen et al. 2017; Metzger et al. 2018). In particular, the observations are consistent with a kilonova characterised by a blue, rapidly decaying, component and a red, more slowly evolving, component. Moreover, Covino et al. (2017) reported a low degree of linear polarization of the optical blue component which is consistent with a symmetric geometry of the emitting region and with low inclination of the merger system.

At the same position of AT2017gfo, a non-thermal emission consistent with a GRB afterglow was first identified in the X-ray and radio bands no more than one week after the GW event (Troja et al. 2017; Hallinan et al. 2017), and only months later in the optical (Lyman et al. 2018; Margutti et al. 2018; Rossi et al. 2018b; Piro et al. 2019) due to Sun observational constraints. Afterwards, the multi-wavelength follow-up continued for up to one year after the GW event (D’Avanzo et al. 2018; Troja et al. 2018b; Piro et al. 2019). The observations show an achromatic slow rising flux up to ~ 150 days after the explosion followed by a decay and are interpreted as emission from a structured jet expanding in the ISM and observed off-axis from a viewing angle of ~ 20 deg with respect to the jet axis (Kathirgamaraju et al. 2018, 2019; Mooley et al. 2018a; Troja et al. 2018b;

Ghirlanda et al. 2019; Salafia et al. 2019). This is consistent with the inclination of the system derived combining the GW signal and the distance of the source (Abbott et al. 2017c; Mandel 2018). Such a scenario predicts a late-time rising afterglow, in contrast with the on-axis case (i.e. when the viewing angle is along, or very close to, the jet axis). The afterglow observations and their consistency with the off-axis model further confirm that all the early (i.e. < 1 month after the GW event) optical/NIR data of AT2017gfo are not contaminated by the afterglow emission, as the latter is initially much fainter as it was already noticed (e.g., Pian et al. 2017).

The precise nature of the different ejection mechanisms and of the different ejecta components is still under debate (Tanaka et al. 2018; Kasen et al. 2017; Metzger et al. 2018; Perego et al. 2017; Radice et al. 2018). Numerical simulations show that, during the merger of two NSs, a small fraction ($\sim 0.05 M_{\odot}$ or less) of the total mass is ejected into space with a latitude-dependent pattern of density, velocity and opacity. Specifically, it is thought that along the polar regions the ejecta have lower velocities and opacities (the *blue* kilonova component; Kasen et al. 2017) with respect to the equatorial region if a NS remnant is formed after the merger. If a **black hole** (BH) is promptly formed, the ejecta are mostly concentrated on the equatorial plane and have high velocity and large opacities (the *red* kilonova component; Kasen et al. 2017). The analysis of the complete set of data of AT2017gfo has clearly demonstrated that **early** ultraviolet and optical observations are of key importance to disentangle the different thermal contributions that are present in the observed emission (e.g., Pian et al. 2017; Arcavi 2018; Villar et al. 2017; Cowperthwaite et al. 2017; Bulla et al. 2018) and at least two, possibly three, different emitting components have been identified (e.g., Perego et al. 2017).

The most plausible evidence of a kilonova before AT2017gfo is that observed as an emerging component **in the light curve of the NIR afterglow of the short GRB 130603B at $z=0.356$** (Tanvir et al. 2013; Berger et al. 2013b). Other possible kilonova signatures were found in the optical counterpart **light curves of GRBs 050709 at $z=0.161$** (Jin et al. 2016), 060614 at $z=0.125$ (Yang et al. 2015; Jin et al. 2015), 080503 (Perley et al. 2009; Gao et al. 2017) at unknown redshift, 150101B at $z=0.134$ (Troja et al. 2018b), and **both in the NIR and (perhaps less clearly) in the optical counterpart light curve of 160821B at $z=0.16$** (Jin et al. 2018; Kasliwal et al. 2017b; Troja et al. 2019; Lamb et al. 2019). Gao et al. (2017) found three other possible kilonova candidates associated to GRBs 050724, 070714B and 061006. However, their peak luminosity at ~ 1 day after the burst are more than one order of magnitude brighter than the typical predicted values of the kilonova associated with GRBs 050709 and 130603B. It should also be noted that in all these possible kilonova identifications (but GRB 150101B), the emission was preceded by a bright GRB **afterglow** indicating an on-axis configuration, thus suggesting that the kilonova emission may exceed the afterglow luminosity even for on-axis GRBs.

After the discovery of AT2017gfo, Gompertz et al. (2018) compared the optical/NIR light curves of AT2017gfo with those of all 23 short GRBs with redshift below 0.5. They were able to firmly exclude the presence of an AT2017gfo-like component in three GRBs (050509B, 061201 and 080905A).

At the same time, they confirmed that AT2017gfo was much fainter than the **claimed** kilonova candidates (see also Fong et al. 2017). These results suggest that kilonovae may display very different luminosity, colours and timescale **evolutions**.

To further investigate the possible range of kilonova luminosity, we compare the optical/NIR light curves of all short GRB with known redshift up to June 2019 with those of AT2017gfo. This paper is organised as follows. In § 2 we describe the AT2017gfo data used in this work and the short GRB sample selection. In § 3 we describe the methods we used to compare AT2017gfo with other short GRB optical/NIR counterparts. Section 4 then illustrates the results about the most compelling short GRBs. These results are then discussed in § 5. Finally, our conclusions are given in § 6.

Throughout this work, we adopt the notation according to which the flux density of a counterpart is described as $F_\nu(t) \propto t^{-\alpha} \nu^{-\beta}$ and we use a Λ CDM world model with $\Omega_M = 0.308$, $\Omega_\Lambda = 0.692$, and $H_0 = 67.8 \text{ km s}^{-1} \text{ Mpc}^{-1}$ (Planck Collaboration: Ade et al. 2016).

2 DATA

In this section we describe spectroscopic and photometric data of AT2017gfo, and the optical/NIR photometric data of short GRBs with known redshift that we compiled and used in this work.

2.1 AT2017gfo data

The follow-up with VLT/X-Shooter of AT2017gfo is not only the first spectroscopic observation of a kilonova, but it also provided the first temporal sampling of this new class of sources. The 10 spectra, described in Pian et al. (2017) and Smartt et al. (2017), were taken between ~ 1.5 and ~ 10.5 days after the GW trigger and have a coverage from UV to NIR bands. We did not consider Gemini-S/GMOS and VLT/FORS spectroscopic observations which are limited only to the optical window. All but two epochs are obtained from Pian et al. (2017). The two epochs at ~ 2.5 and ~ 4.5 after the GW trigger are from Smartt et al. (2017)¹ and have been taken from the last version available on *WISEREP* (Yaron & Gal-Yam 2012).

At epochs earlier than the first spectrum (i.e. < 1.5 days after the GW trigger), we have collected photometric observations from the works of Tanvir et al. (2017), Drout et al. (2017), Evans et al. (2017), Covino et al. (2017), Coulter et al. (2017), Troja et al. (2017), Pian et al. (2017), Cowperthwaite et al. (2017); see also the Kilonova Project: Guillochon et al. (2017). We interpolated the photometric light curves using a cubic spline to build the spectral energy distribution (SEDs) at three epochs. The first epoch at ~ 0.5 days after the trigger roughly corresponds to the first optical/NIR observations, the second epoch at 0.66 days is the first one with UV data, and the third epoch at ~ 1 day after the trigger lays between the first photometric and the first X-Shooter observations (Fig.1). Note that we did not use

Table 1. The 39 short GRBs used in this work.

GRB	z	$P_{cc}(< \delta R)$ a	References	Accurate redshift
050509B ^b	0.225	5×10^{-3}	1-2	y
050709 ^b	0.161	3×10^{-3}	1	y
050724 ^b	0.258	2×10^{-5}	1	y
051221A	0.546	5×10^{-5}	1	y
060502B	0.287	0.03	1-3	n
060614 ^c		0.125 ^d	1-4	y
060801	1.13	0.02	1-3	n
061006 ^b	0.438	4×10^{-4}	1	y
061201 ^b	0.111	0.08	1-5-6	n
061210 ^b	0.41	0.02	1-3	y
061217	0.827	0.24	1-5	n
070429B	0.902	3×10^{-3}	1	y
070714B ^b	0.923	5×10^{-3}	1	y
070724A ^b	0.456	8×10^{-4}	1	y
070729	0.8	0.05	1-5-7	y
070809	0.473	0.03	1-4-6	n
071227 ^b	0.381	0.01	1	y
080905A ^b	0.122	0.01	1	n
090510 ^b	0.903	8×10^{-3}	1-5	y
090515	0.403	0.15	1-4	n
100117A	0.915	7×10^{-5}	1	y
100206A	0.407	1×10^{-3}	1-8	y
100625A	0.452	0.04	1	y
100816A ^c	0.805 ^d	---	9	y
101219A	0.718	0.06	1	y
111117A	2.211	0.02	1-10-11	y
120804A	1.3	210 – 4	12	y
130603B ^b	0.356 ^d	–	13	y
131004A	0.717 ^d	–	14-15	y
140903A ^b	0.351	3×10^{-4}	16	y
141212A	0.596	0.03	17-18-This work	n
150101B	0.134	4.8×10^{-4}	19	y
150120A	0.46	0.02	20-21-This work	n
150423A ^c	1.394 ^d	see text	22-23	n
150424A ^c	0.3	0.02	24-25-26-This work	n
160410A ^c	1.717 ^d	–	22	y
160624A ^c	0.483	0.01	27-This work	y
160821B ^c	0.16	0.02	28-29	y
170428A ^c	0.454	4×10^{-3}	30-This work	y

^a probability of chance coincidence (Bloom et al. 2002).

^b light curve updated with respect to Fong et al. (2015) with new data. See Table A2.

^c not in Fong et al. (2015), photometry in Table A2.

^d redshift measured from the afterglow spectrum. In these cases association with a host galaxy was not necessary and therefore not reported.

References for the probability of chance association and redshift: (1) Fong et al. (2013); (2) Bloom et al. (2006); (3) Berger et al. (2007); (4) (Price et al. 2006); (5) Berger (2010); (6) Stratta et al. (2007); (7) Fong & Berger (2013); (8) Perley et al. (2012); (9) (Tanvir et al. 2010); (10) Margutti et al. (2012); (11) Selsing et al. (2018); (12) Berger et al. (2013a); (13) de Ugarte Postigo et al. (2014); (14) Chornock et al. (2013); (15) D’Elia et al. (2013); (16) Troja et al. (2016); (17) Malesani et al. (2014); (18) Chornock et al. (2014); (19) Fong et al. (2016); (20) Chornock & Fong (2015); (21) Perley & Cenko (2015); (22) (Selsing et al. 2019); (23) (Malesani et al. 2015); (24) (Castro-Tirado et al. 2015); (25) Jin et al. (2018); (26) Tanvir et al. (2015); (27) (Cucchiara & Levan 2016); (28) (Levan et al. 2016); (29) Troja et al. (2019); (30) (Izzo et al. 2017).

¹ They are limited to $\sim 22000 \text{ \AA}$ due to the presence of K-band blocking filter.

all data available in the literature, because these data show great variation in values, even though the single data points have in most cases very small uncertainties. This can be ascribed to different calibration and the problematic removal of light from the underlying host galaxy. Therefore, we decided to use only photometric data from large telescopes and from the restricted number of works given above.

All data have been corrected for the Galactic absorption using the interstellar extinction curve derived by [Cardelli et al. \(1989\)](#), the dust maps of [Schlafly & Finkbeiner \(2011\)](#), and an optical total-to-selective extinction ratio $R_V = 3.1$. All observations have been converted to flux densities F_V using transmission curves or instrument-specific conversion factors when available, or the standard conversions following [Blanton & Roweis \(2007\)](#).

2.2 The short GRB data sample

Our starting sample of short GRBs is that presented by [Fong et al. \(2015\)](#) which includes 87 short GRBs with optical and NIR counterparts observed between November 2004 and March 2015. We considered only the 33 events that have a redshift determination. We extended this sample by including 6 short GRBs with known redshift, detected between March 2015 and December 2018.

In addition, we took into account many works that show that the short/hard versus long/soft division does not map directly onto what would be expected from the two classes of progenitors (e.g., [Kann et al. 2011](#)). For instance, [Bromberg et al. \(2012\)](#) showed that the 2 s duration commonly used to separate collapsars and non-collapsars is inconsistent with the duration distributions of Swift and Fermi GRBs and only holds for old BATSE GRBs. For this reason we included the two peculiar long GRBs 060614 and 100816A, because their spectral hardness and negligible spectral lags are typical of short GRBs (see also [Bernardini et al. 2015](#)). With respect to the [Fong et al. \(2015\)](#) sample we removed GRB 140622A because only very early upper limits exist (i.e. < 0.1 hours after trigger) that could not be compared with AT2017gfo observations that started 0.5 days after the trigger. We also excluded GRB 090426 which, although having a duration shorter than 2 seconds, has features similar to collapsar events (soft spectra, dwarf blue host, very luminous afterglow, [Antonelli et al. 2009](#); [Nicuesa Guelbenzu et al. 2011, 2012b](#)). In addition, we have also updated the light curves of the whole short GRB sample by adding photometric measurements that were not included in the original [Fong et al. \(2015\)](#) data set (see Tab. A2). Finally, we have updated the redshift of GRB 111117A with the more refined measure of $z=2.211$ ([Selsing et al. 2018](#); [Sakamoto et al. 2013](#)). Note that, contrary to [Gompertz et al. \(2018\)](#), we decided to not include GRB 051210 because, according to the most recent literature, only a lower limit on the redshift exists ($z > 1.4$, see [Berger et al. 2007](#); [Fong et al. 2015](#)). The final sample thus consists of 39 short GRBs within the redshift range $0.1 \leq z \leq 2.2$ and is summarised in Table 1.

In all cases we pay particular attention to not include photometry that was dominated by the host according to the literature from which we obtained the data. In the case the origin of the emission was not specified or was not certain in the literature, then we considered only data that showed to be fading. However, in all cases we have not considered

necessary to model the light curves to search for a constant component, i.e., the host.

2.3 On the redshift accuracy

Accurate and reliable redshift determination through optical/NIR spectroscopy of short GRB afterglows have been obtained only in **three cases (GRBs 100816A, 130603B, 160410A)**. In case of GRBs 060614 and 131004A the redshift is measured from emission lines of the host superposed from the afterglow spectrum². In all other 34 cases, the redshifts have been obtained through spectroscopy of the associated host galaxies. **To assess the probability that the burst originated from a host candidate, we have collected or calculated the probability of chance coincidence, $P_{cc}(< \delta R)$ ([Bloom et al. 2002](#)), at a given angular separation (δR), and apparent magnitude (m) for galaxies candidates.**

In table 1 we indicate redshifts, probabilities, and their references. In few cases the probabilities are not negligible (larger than 1%), but given the lack of any other possible galaxy with similarly low chance association, they are considered as good association. They are GRBs 061210, 070729, 100625A, 101219A, 111117A. In 9 cases no clear association can be made with a galaxy in the field (GRBs 060502B, 060801, 061201, 061217, 070809, 090515, 141212A, 150120A, 150424A). Therefore, they do not have well-defined redshift measurements.

In almost all other cases the association with the host is well defined following the criteria of [Bloom et al. \(2002\)](#) and it was possible to measure a redshift (table 1). Only two cases deserve more caution: GRBs 080905A and 150423A. In the first case, [D’Avanzo et al. \(2014\)](#) find that its properties are not consistent with the E_{peak} - L_{iso} ([Yonetoku et al. 2004](#)), and the E_{peak} - E_{iso} relations ([Amati et al. 2002](#)). They conclude that either GRB 080905A is really a peculiar sub-luminous (and sub-energetic) burst, or the associated host galaxy is just a foreground source, and the distance is underestimated. In the case of GRB 150423A we adopted the redshift of $z = 1.394$ measured by [Malesani et al. \(2014\)](#) and [Selsing et al. \(2019\)](#). However, as noted in [Malesani et al. \(2014\)](#) the redshift is based only on a tentative detection of an absorption doublet in the faint afterglow continuum, and identified as Mg ii at $z = 1.394$. Our independent analysis of the reduced spectrum, have not permitted us to confirm the presence of the absorption lines. We note that [Perley \(2015\)](#) reports the presence of a galaxy at redshift of $z = 0.456$ with $r = 23.3$ ([Varela et al. 2015](#)) and $4''$ away from the afterglow position (with $P_{cc} = 0.13$) and thus leaving the distance measurement for this burst still uncertain.

Finally, we note that in the case of GRB 061201 we used the redshift of 0.111 of the nearest galaxy ([Stratta et al. 2007](#)), used also by [Fong et al. \(2015\)](#), which is different from $z = 0.084$ used by [Gompertz et al. \(2018\)](#) that is the redshift of the galaxy cluster within which this GRB happened. In

² In case of GRB 131004A possible weak absorption lines at this same redshift are also present ([Chornock et al. 2013](#)).

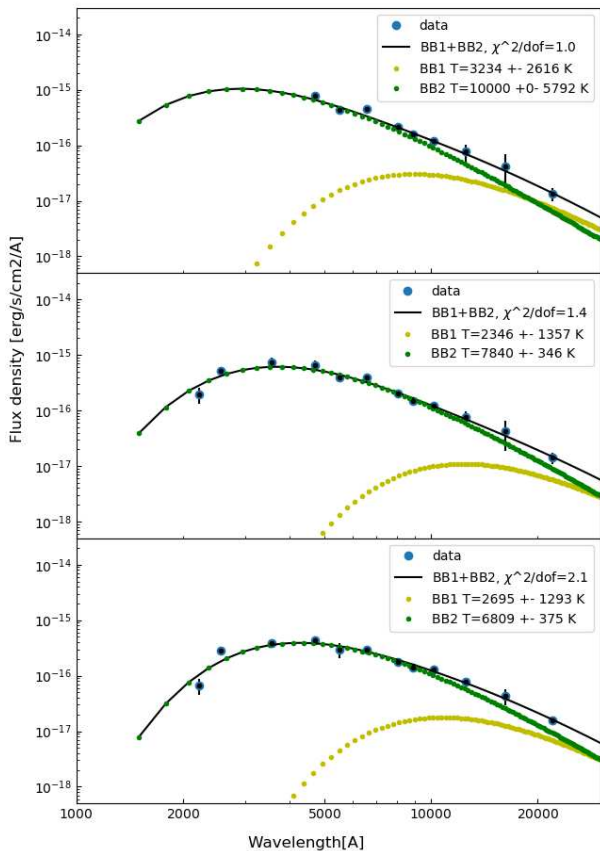


Figure 1. Photometry at 0.5, 0.66 and 1 days after trigger (blue dots with error-bars) of AT2017gfo modelled with a double black-body model (in black), with single black-body components in green and yellow; see § 3.1).

summary, we estimate that for 28 short GRBs out of 39 events, the associated redshift is highly reliable.

3 DATA ANALYSIS

In order to compare AT2017gfo with GRB optical counterparts, we computed the AT2017gfo luminosity in the GRB rest-frame filters. This approach allows us to use the exceptionally high quality data set of AT2017gfo which provides much better spectral accuracy and coverage than that of typical GRB afterglows, enabling a more precise flux estimate in the redshifted frequencies. We thus first built a set of rest-frame AT2017gfo spectra at different epochs, which hereafter we will refer as kilonova spectral templates. We then convolved these spectra with the optical/NIR filters scaled to the GRB rest frames and proceeded with the luminosity comparison.

This procedure is similar to that used by Gompertz et al. (2018). However, the use of X-Shooter spectra allows us to simplify the approach. First of all, except for the black-body modelling of the photometry for the first 3 epochs, we do not interpolate the SED to obtain the photometry in a specific filter, because the X-Shooter spectroscopy guarantees full spectral coverage. Secondly, we do not need to make any special assumption for the bluer part of the spectra of

AT2017gfo, because the X-Shooter spectra extends down to 3500 Å (including half of the *U*-band). With our method we can give robust constraints to the rest-frame optical data (< 6000 Å) up to redshift ~ 0.7 . We also note that, in our case, we do not use an analytical function to model the light curves, since we have better temporal sampling. Instead, we interpolate the photometry derived from the spectral templates when we need to compute the luminosity ratio (Table A1). Below we explain all the steps of this analysis in more detail.

3.1 Kilonova spectral templates

After including the three SEDs built at 0.5, 0.66 and 1 days after the trigger, we have a total of 13 epochs that we use to build the kilonova spectral templates.

We modelled the SEDs (at 0.5, 0.66 and 1 days after the trigger) following the current theoretical interpretation of AT2017gfo, where the observed emission is the combination of at least two different black body components³. Results are plotted in Fig. 1. We note that even in the early phase when matter is extremely dense, opaque and hot, strong line blanketing can be at work and the absorption in the UV may not be negligible and thus the real temperature of the blue component can be higher. In the first epoch at 0.5 days after the trigger, the peak of the black-body is at much bluer wavelengths than the available photometry and cannot be constrained, therefore, in this case, we have only extrapolated the model to the NIR, after imposing the black-body temperatures to be ≤ 10000 K. For this reason, the *U* and *B* band KN template light curves start at 0.66 and not at 0.5 days after the trigger, like the other bands.

In order to maximise the possibilities of comparison with GRB counterparts down to the UV and up to the NIR regimes, we then modelled the UV and NIR extremes of the spectra, leaving untouched the rest of the spectral interval already covered. At the time of the X-shooter spectra (>1.5 days) it is likely that the ejected matter becomes more transparent and absorption features starts to dominate the spectra. Therefore, modelling the data with one or more black-body components without considering absorption is not possible. However, given that we are only interested in expanding the spectral interval of the templates in the case of the X-Shooter spectra we have modelled the data with two power-laws, one below 5000 Å and one above 21000 Å (see Fig. 2). The best fit models have been used to extrapolate the AT2017gfo flux down to 1,500 Å and up to 26,000 Å. Finally, we have computed the best fit spectral models in the kilonova rest-frame. For AT2017gfo we have adopted the redshift $z_{KN} = 0.0098$ (Hjorth et al. 2017) that, with the assumed PLANCK cosmology, corresponds to a luminosity distance of $D_L = 43.7$ Mpc.

The result of this procedure is a set of spectral templates, covering the UV to NIR range, computed at differ-

³ We note that a more sophisticated model has been used by other authors (Villar et al. 2017; Cowperthwaite et al. 2017) who found some evidence of an intermediate black-body component. However, given that our goal is only to model the extremes of the spectral interval, we considered that an intermediate component is too sophisticated for the aim of this work.

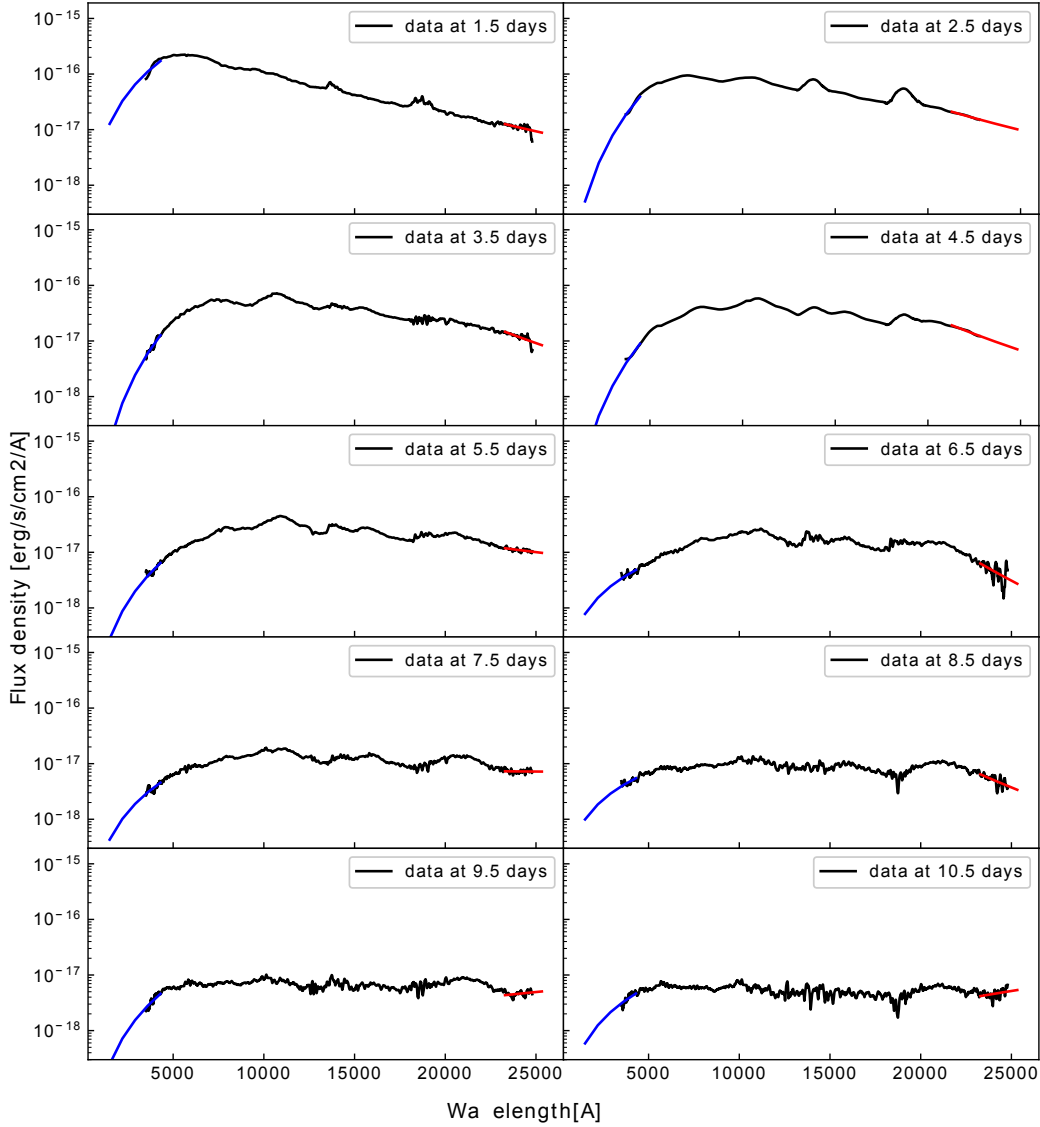


Figure 2. X-Shooter spectra between 1.5 and 10.5 days after the trigger (black) of AT2017gfo. The blue and NIR tails have been modelled with a power-law $F(\nu) \propto \nu^a$ (blue and red lines; see § 3.1).

ent epochs between 0.5 and 10 days after the GW trigger. We then used these templates to produce rest-frame light curves of AT2017gfo for all the GRB filters as explained in the next section (Table A3). In Figure 3 we show a sample of light curves for few selected optical/NIR filters, computed also assuming a luminosity distance of 40.7 Mpc, as found by [Cantiello et al. \(2018\)](#). It is clear that the peak of the optical emission lies in the first day after the trigger, while the NIR emission is almost constant during the first 6 days and dominates the emission after 2 days.

3.2 Comparison with short GRBs

To proceed with the AT2017gfo - short GRBs comparison, each short GRB flux F_ν measured at the time t_{GRB} was converted to a luminosity and, for each filter, a rest-frame light curve was built. In order to compare the AT2017gfo

and GRB luminosity in the same frequency, we proceeded as follows. For each GRB of our sample, we have a set of filters used for the observations. Given a GRB at redshift z_{GRB} , for each filter X centred at the observed frequency ν_X , we computed an effective rest-frame filter X_{eff} centred at $\nu_{X,eff} = \nu_X \times (1 + z_{GRB})$. By integrating the AT2017gfo luminosity spectra taken at different epochs (t) over the effective rest-frame filter ⁴ X_{eff} , we were able to build a AT2017gfo luminosity light curve $L_{X,eff}(t)$ in the rest frame filter X_{eff} , i.e., the same in which the GRB was observed.

With this procedure, we built a set of AT2017gfo luminosity light curves in the same set of filters used to observe a given GRB. In this way we could proceed in a straightforward manner to the comparison of the luminosity

⁴ The effective rest-frame filter was obtained by multiplying the filter response matrix by $(1 + z_{GRB})$

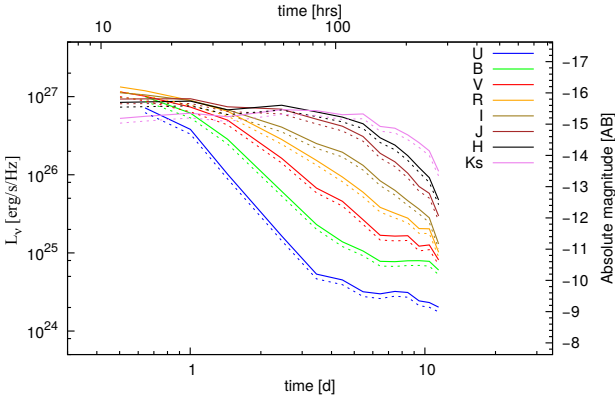


Figure 3. Rest frame light-curves of AT2017gfo in few selected filters. The *U* and *Ks*-band light curves were obtained by extrapolating photometry and spectroscopy to obtain a full coverage of the filter transmissions (see § 3.1 and Table A3). The dashed-line curves have been obtained assuming a distance of 40.7 Mpc as found by Cantiello et al. (2018).

of AT2017gfo and the GRB afterglow in each filter. Note that using the distance of 40.7 Mpc found by Cantiello et al. (2018) AT2017gfo would become fainter of a factor ~ 1.15 and therefore the luminosity ratios would change. However, this would not change qualitatively our conclusions.

4 RESULTS

In the following we present the results obtained from the comparison in each filter of the AT2017gfo luminosity and those of the optical and NIR counterparts of our selected sample of short GRBs.

The GRB counterparts and AT2017gfo light curves in different bands are plotted as luminosity (left side) and apparent magnitude (right side) versus rest-frame time in Figs. A1, A2, A3, A4. Note that several filters with similar wavelength have been grouped into a single one in the plots for visualisation purposes, and that the filters quoted in each plot are the “effective” ones, i.e. the observed filters shifted to the GRB rest frame (§3.2).

In order to avoid any model-dependent temporal extrapolation, in this work we limited the comparison to the short GRBs observations that fall in the sampled AT2017gfo temporal window (0.5–10.5 days in rest-frame). For this reason, for 13 short GRBs the comparison with AT2017gfo was not possible. However, we still show their light curves as illustrative examples of the magnitude range of AT2017gfo-like emission in comparison with those of the observed GRB counterparts (see Fig. A4). In the case of GRB 100206A, albeit not covered by the KN templates, the gap is negligible and the observations are clearly fainter than the kilonova template (see below § 4.1). In Table A1 we quote the luminosity as well as the ratios between GRB counterpart and AT2017gfo luminosity in the spectral bands and at the time of the observations at which such comparison was possible.

On the basis of the luminosity ratios and on the temporal behaviour of the GRB counterpart luminosity, we built three main groups as described below (see §4.1, §4.2, and

Table 2. Summary of the GRB to kilonova luminosity ratios in the effective rest-frame filters (§3.2) of short GRBs that stand out for their properties (full Table in A1). The sample is divided between events fainter (first part of the table) and brighter (second part of the table) than AT2017gfo. GRBs with accurate redshift (§2.3) are quoted in bold.

GRB	time ^a (hrs)	Band ^b (eff)	λ_{eff} ^b (nm)	L -ratio ^c GRB/KN	ID ^d	Com. ^e
050509B	21.2	R/(1+z)	523	<0.3	blue	–
	36.6	R/(1+z)	523	<0.2	blue	
	52.2	R/(1+z)	523	<0.7	blue	
050709	50.8	I/(1+z)	681	0.8	blue	S,KN
061201	29.8	I/(1+z)	712	<0.3	blue	–
	73.3	I/(1+z)	712	<0.7	blue	
080905A ^f	12.8	R/(1+z)	572	0.3	blue	–
090515	17.8	r/(1+z)	446	0.4	blue	S
160821B	22.1	r/(1+z)	539	0.9	blue	S,KN
	42.0	r/(1+z)	539	0.6	blue	
	78.1	J/(1+z)	1081	0.5	red	
	102.8	K/(1+z)	1863	0.9	red	
100206A	~ 10	i/(1+z)	544	< 1	blue	–
050724	27.7	I/(1+z)	628	6.0	blue	S,MKN
	66.1	I/(1+z)	628	2.4	blue	
	27.8	R/(1+z)	510	9.1	blue	
060614	12.8	R/(1+z)	570	16.9	blue	S,KN
	143.8	R/(1+z)	570	8.6	blue	
070714B	54.9	R/(1+z)	333	263	blue	MKN
070809	23.8	R/(1+z)	435	3.4	blue	KN
130603B	28.3	r/(1+z)	462	1.3	blue	KN
	164.7	H/(1+z)	1218	3.0	red	
150101B	35.1	r/(1+z)	552	2.1	blue	KN
150424A	16.4	r/(1+z)	481	15.2	blue	S
	12.4	J/(1+z)	964	37.2	red	

^a rest-frame time

^b rest-frame effective band and effective wavelength (§3.2)

^c GRB optical counterpart to AT2017gfo luminosity ratio

^d This column indicates if the effective wavelength is below (blue) or above (red) 9000 Å.

^e ‘S’= evidence of shallow decay from this work; ‘KN’= evidence of kilonova from the literature; ‘MKN’= evidence of magnetar-powered KN from Gao et al. (2017)

^f In the case of GRB 080905A, the decay index of the optical/NIR light curve is $\alpha = 0.4 \pm 1.3$ between 7 and 16 hours after the trigger (rest-frame), i.e., not enough to be constrained.

§4.3). The first group includes 7 GRBs with a counterpart fainter than AT2017gfo in at least one filter. The light curves of these GRBs are shown in Figure A1 and two examples are plotted in Figure 4. The 19 short GRB counterparts brighter than AT2017gfo are plotted in Figure A2 and Figure A3. Moreover, we distinguish between the *blue* and *red* components, depending on whether the rest-frame effective wavelength is below or above 9000 Å, respectively. In Table 2 we summarise the short GRBs that stand out for their properties.

4.1 Short GRBs with optical counterpart fainter than AT2017gfo

We find that in seven cases (namely GRBs 050509B, 050709, 061201, 080905A, 090515, 100206A and 160821B) the lumi-

Table 3. Summary of the GRBs with evidence of an anomalous shallow decay and/or with a claimed kilonova in the literature. GRBs with well defined redshift (§2.3) are quoted in bold and represent our golden sample (§5.2).

GRB	Band ^a (eff)	α^b	t_{start}^c (hrs)	t_{end}^c (hrs)	Com. ^d
050709	$I_{/(1+z)}$	0.6 ± 0.2	50.7	115.8	KN, S
	$I_{/(1+z)}$	1.2 ± 0.1	115.8	202.1	
050724	$R_{/(1+z)}$	< 0	4.4	9.4	MKN, S
	$R_{/(1+z)}$	1.5 ± 0.1	9.4	27.8	
060614	$R_{/(1+z)}$	0.2 ± 0.1	1.0	10.0	KN, S
090515	$r_{/(1+z)}$	0.1 ± 0.1	1.2	17.8	S
150423A	$r_{/(1+z)}$	0.4 ± 0.2	0.4	1.7	S
150424A	$R_{/(1+z)}$	0.09 ± 0.03	1.2	10.1	S
160821B	$R_{/(1+z)}$	0.0 ± 0.1	1.0	1.6	KN,S
	$R_{/(1+z)}$	0.40 ± 0.03	1.6	22.1	
070714B	$R_{/(1+z)}$	1.0 ± 0.3	12.3	54.9	MKN
130603B	$H_{/(1+z)}$	1.6 ± 0.1	10.7	164.7	KN
	$R_{/(1+z)}$	2.7 ± 0.1	10.9	28.3	
150101B	$r_{/(1+z)}$	1.0 ± 0.3	35.1	56.1	KN

^a rest-frame effective band (§3.2)

^b decay index ($F_\nu(t) \propto t^{-\alpha}$)

^c rest-frame time interval within which α was computed

^d 'S'= evidence of shallow decay from this work; 'KN'= evidence of kilonova from the literature; 'MKN'= evidence of magnetar-powered KN from Gao et al. (2017)

nosity of the optical counterparts is smaller than that of AT2017gfo in at least one filter. This is also true in the case of GRB 100206A although the photometric monitoring ending before the temporal window of the light curve of AT2017gfo.

In the first part of Table 2 we report the rest-frame time after the GRB event (together with the effective rest-frame filters and wavelengths; see §3.2) in which we find that AT2017gfo was fainter than the optical/NIR counterpart of the GRB by a factor quoted in the fifth column as the luminosity ratio. We note that for 2 of these 7 short GRBs (namely GRB 050709 and GRB 160821B) a kilonova emission has been invoked in the literature (Jin et al. 2016, 2018; Kasliwal et al. 2017a; Troja et al. 2019; Lamb et al. 2019). These GRBs have been labelled in the last column of Table 2 with "KN". The cases with evidence of magnetar-powered KN (see Gao et al. 2017) have been labelled with "MKN". Moreover, for 3 GRBs we find evidence of a shallow decay not consistent with the standard fireball model (see next Section). The latter ones are labelled with "S" in Table 2. For all the short GRBs belonging to this group we could probe the *blue* kilonova component and constrain its luminosity within a range of 0.2-1 times the AT2017gfo luminosity. In the NIR, only the red counterpart of GRB 160821B is fainter (0.4-0.9 times) than At2017gfo (Tab.2).

4.2 Short GRB counterparts with shallow decay

A kilonova is expected to show a shallow evolution close to its maximum brightness. Therefore, it can be distinguished from the standard afterglow decay, which at the typical observing time (i.e., $>$ min after the burst) has a constant power-law decay (e.g., Sari et al. 1998, 1999; Zhang & Mészáros 2004; Zhang et al. 2006).

Kilonova peak brightness is typically estimated around a few days after the merger assuming simple one-component modelling and fiducial values (e.g., Metzger et al. 2010). However, according to more sophisticated models (e.g. Radice et al. 2018), the kilonova maximum brightness can be as early as <0.1 days, depending on the nature of the central remnant (i.e. if a black hole or a neutron star is generated, see their Fig. 28). Thus, we considered as possible evidence of a kilonova a shallow evolution in the optical counterpart of the short GRBs that can happen from a few hours after the burst up to a few days. **Our simple method of kilonova identification is effective only near the kilonova peak epoch. In fact, it is not suited to find events where the kilonova is dominating but its decay is too steep to be distinguished from an afterglow (for example see the case of GRB 150101B in §4.3). A shallow decay simultaneous to a X-ray plateau can possibly indicate the presence of a MKN (see Gao et al. 2017), although other explanations are possible (e.g., Mangano et al. 2007). Therefore, we also describe the simultaneous behaviour of the X-ray light curve.**

Under the reasonable assumption of a slow cooling regime for the electrons producing the observed afterglow radiation (see Sari et al. 1998, 1999) the predicted shallowest flux decay power law index is $\alpha = 3(p-1)/4$ where p is the power law index of the electron energy distribution. In this context, using a minimal electron index $p = 2$ in the slow cooling regime, we considered a decay to be anomalously shallow when $\alpha < 0.75$. We computed the decay index α for all GRBs for which two or more observations were available. We note that the flattening in the GRBs 071027 and 061006 is due to the contribution from the host (D'Avanzo et al. 2009), and thus they are not considered here.

In 7 cases we have found a suspicious shallow decay that can indicate the presence of a kilonova emission dominating over the afterglow component. **We quote them in Table 2.** Note that in all cases, we could measure a shallow decay only in the optical filters, i.e. in the regime of the blue component. The results are summarised in Table 3. In Figure 5 we compare the estimated decay indexes with those of AT2017gfo, computed assuming a power-law evolution between consecutive template epochs (Fig. 3). Note that the decay index of the kilonova is always smaller in the *J*-band than in optical bands thus reflecting the expected smoother evolution in the red band with respect to the blue one.

In the following, we discuss in more detail these bursts. Note that 3 of them (GRBs 050709, 090515, 160821B) are also part of the first group, i.e., those GRB optical counterparts that are fainter than AT2017gfo. **According to AT2017gfo templates (Fig.3), the blue component dominates during the first 24 hours, therefore we first list those short GRBs for which we measured a shallow decay before 1 day. We include also those short GRBs for which we measured a shallow decay at epochs earlier than the first AT2017gfo observation (i.e. before ~ 11 hours).**

- **GRB 050724.** Its early *R*-band light curve is rising between 5.6 and 11.8 hours after the trigger (4.4 and 9.4 hours rest-frame), with $\alpha \sim -0.5$. **Simultaneous X-**

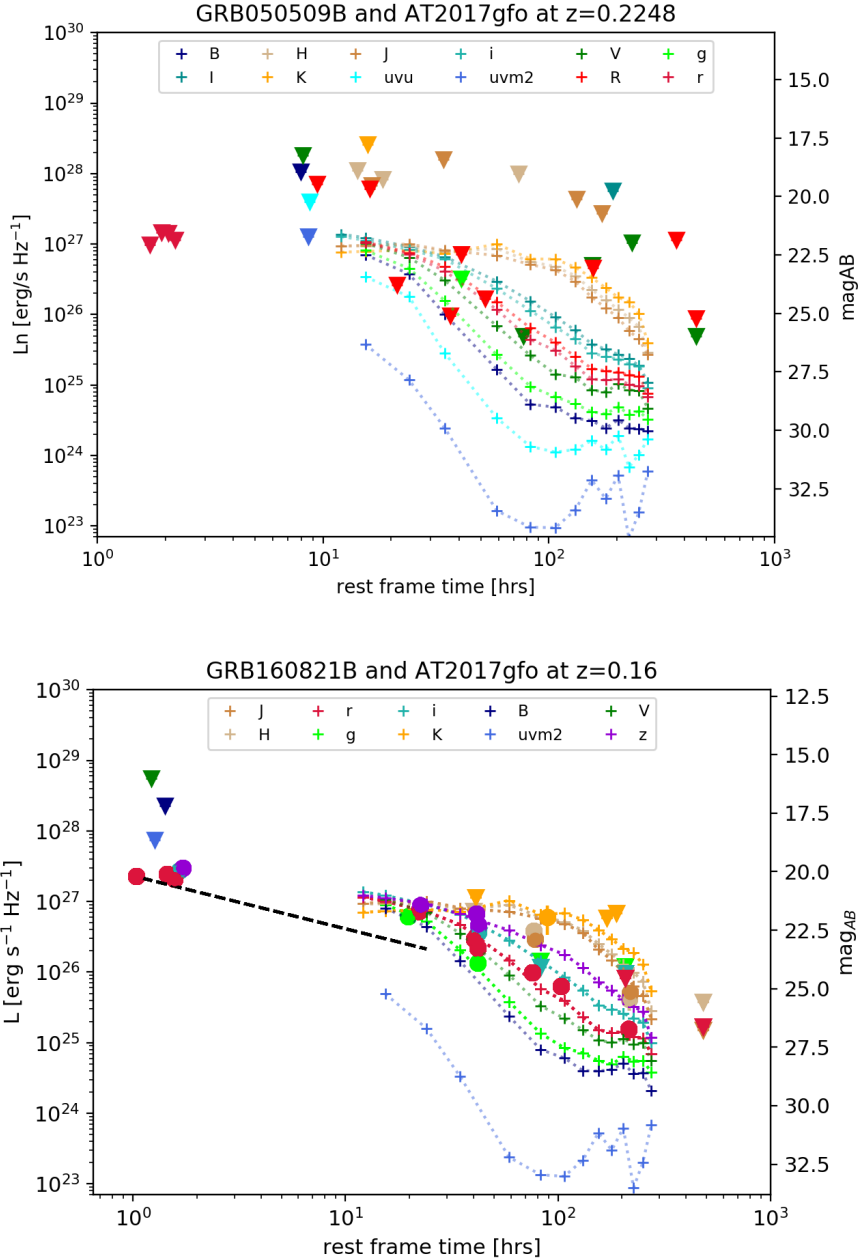


Figure 4. Two examples of short GRBs for which the optical counterpart luminosity (circle for a detection and triangle for an upper limit) are fainter than AT2017gfo luminosity (dotted lines with crosses) in at least one effective rest-frame filter (see §3.2 for effective rest-frame filter definition). See figure A1 for the full sample of short GRBs with similar properties. Note that GRB 160821B (right) shows evidence of a temporal decay index lower than the shallowest index predicted by the fireball model (i.e. $\alpha = 0.75$, see §4.2, black dashed line). If this anomalous shallow decay is due to an emerging kilonova emission, its NIR luminosity is a factor of 1.2-2 fainter than AT2017gfo at epochs later than 3 days after the merger time (see Tab.2).

ray and radio data show a similar trend. Gao et al. (2017) interpreted this behaviour as evidence for a kilonova powered by a magnetar. We find that, if it were an emerging kilonova, its blue component is brighter than AT2017gfo up a factor 9 and 6 in *R* and *I* bands at ~28 hours (rest-frame), respectively. This factor decreases to ~2.4 at ~66 hours.

- GRB 060614A. In this case the *R*-band light curve

shows a clear shallow decay phase between 1.5 and 11 hours (1 and 10 hours in rest-frame) simultaneous with an X-ray plateau feature, with a brightening peaking at ~4 hours after the trigger. In this case, the detected luminosity are a factor of ~16 larger than the *R*-band luminosity of AT2017gfo at ~12.8 hours after the trigger. Jin et al. (2015); Yang et al. (2015) found a kilonova component for this burst at more than ~3 days after

the trigger from an optical excess in the afterglow. At this time we find no clear evidence of an optical shallow decay (see § 5.2.1).

- **GRB 090515.** In this case the r -band light curve has a decay index $\alpha \sim 0.1$ between 1.7 and 25 hours after the trigger (**1.2 and 17.8 hours rest-frame**). Moreover, a very late ($\sim 10^3$ hrs) deep upper limit confirms that no emission from an underlying host is affecting the early data. **The X-ray afterglow is very weak and no data is available for a comparison after the first hour.** If a kilonova is emerging from the afterglow emission, it is fainter than AT2017gfo by a factor of 2.3 at ~ 18 hours after the trigger. Note that this case was already presented in §4.1.

- **GRB 150423A.** This burst shows a shallow decay behaviour in the i - and z -bands, with index $\alpha = 0.4 \pm 0.2$ in the r -band before 4 hours after the trigger (**1.7 hours in rest-frame**). The temporal mismatch with the AT2017gfo light curves prevents us from performing a more quantitative comparison. **We note that during the same time interval the X-ray light curve is much steeper** ($\alpha_X \sim 0.96 \pm 0.07$), thus suggesting a different origin with respect to the optical counterpart.

- **GRB 150424A.** In this case the r -band light curve has an atypical shallow decay with index $\alpha \sim 0.1$ between 1.6 and 13 hours after the trigger (**1.2 and 10.1 hours in rest-frame**), simultaneous with an X-ray plateau feature. If a kilonova is the dominant component, its blue component is brighter than AT2017gfo by a factor of ~ 15 at ~ 16.4 hours after the trigger (rest-frame), i.e. at the end of the shallow phase. At the same time in the J, H bands the light curve is brighter than AT2017gfo by a factor ~ 30 and falls to ~ 2.3 times brighter at ~ 124 hours after the trigger.

- **GRB 160821B.** For this event, the presence of a kilonova emission was claimed by Troja et al. (2019). In this case, the R -band counterpart shows a brightening at ~ 1 hour after the trigger ($\alpha \sim -0.3$), which then steepens to $\alpha \sim 0.9$ between 1 and 86 hours after the trigger (**1.6 and 74.5 hours in rest-frame**). A very weak X-ray afterglow possibly show evidence of a plateau lasting ~ 1 day after the burst. If an underlying blue kilonova component is peaking at ~ 1 day after the trigger, the kilonova is fainter than AT2017gfo by a factor in the range 1.1-2.5 (see Tab.2). As also noted by Troja et al. (2019) the late J and H -band light curves have a behaviour similar to that of KN170817, but have a decay index larger than one (see also Lamb et al. 2019). This case was already presented in §4.1.

Below we list those short GRBs for which we measured a shallow decay at more than 24 hours after the trigger.

- **GRB 050709A.** For this burst the presence of a kilonova was claimed by Jin et al. (2016). In this case the R -band light curve is very shallow with $\alpha \sim 0.7$ between 59 and 134 hours after the trigger (**51 and 116 hours rest-frame**) and no straightforward comparison with X-ray data was possible due to the lack of enough statistics in the data (Fox et al. 2005). From the comparison with AT2017gfo, if the claimed kilonova signature is real, then its luminosity is comparable within the uncertainties in the K, I and V -bands, although afterglow contamination is still possible. This case was already presented in the previous section.

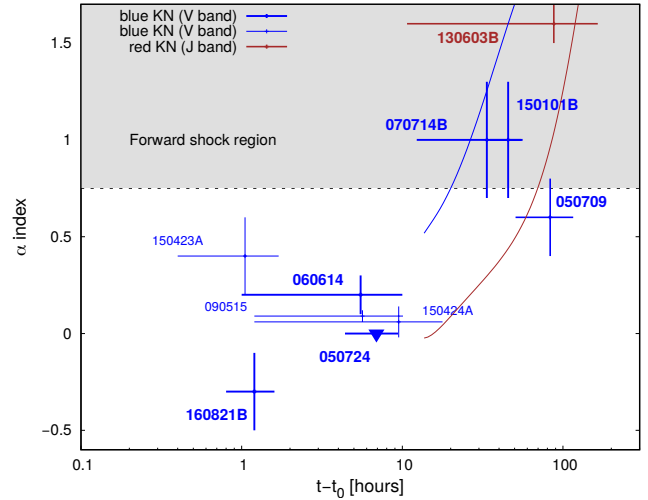


Figure 5. The lowest decay indices of the GRB optical counterparts with shallow decay. See Table 3. The short GRBs labels are coloured following the band in which the decay index was computed. Upper limits are indicated as downward triangles. **GRBs in the golden sample are highlighted in bold.** The horizontal line indicates the lowest possible decay index predicted by the afterglow theory ($\alpha = 0.75$; see §4.2). The curves are the smoothed splines of the decay indices of AT2017gfo in the V and J-bands, from top to bottom, computed in the 13 epochs. These are derived by computing the decay between two epochs in the template light curves shown in §3 with a time step of 0.5 days.

4.3 Short GRBs with known kilonova candidates

In few cases a kilonova component has been found in the optical/NIR GRB counterpart **light curves** and published in the literature. Two of them (GRBs 050709 and 160821B) have an optical counterpart fainter than AT2017gfo and are already part of the first group in Table 2. Others (namely GRBs 050724, 060614, 070714B, 070809, 130603B and 150101B) have an optical/NIR counterpart brighter than AT2017gfo and we report them in the second part of Table 2.

Gao et al. (2017) found evidence of kilonova in GRBs 050724 (see §4.2), 061006 and 070714B by modelling the X-rays and optical light curves with a MKN model. However, as we noted in §4.2, D’Avanzo et al. (2009) found that the optical light curve of 061006 is dominated by the host galaxy, thus we have included only GRB 050724 and GRB 070714B in our analysis (see Tab. 3). In case of 070714B, we cannot identify a shallow phase, but Gao et al. (2017) found a MKN peaking at ~ 2 days (observer frame; ~ 1 day in rest-frame). During the time when this component is dominating there are two photometric epochs, one at ~ 11 hours (just earlier than the first AT2017gfo photometric measurement) and one at ~ 55 hours. During the first epoch the blue counterpart is clearly more than 10 times brighter than AT2017gfo, and the ratio increases to ~ 260 times at the second epoch.

In the case of GRB 070809, recently Jin et al. (2019) discovered a kilonova in its optical light

curve. Unfortunately, its redshift is not well determined and therefore it cannot be used to constrain the optical luminosity of the kilonova with confidence.

For GRBs 130603B and 150101B a kilonova component was claimed in the literature (Tanvir et al. 2013). The kilonova was detected with an observation taken ~ 7 days after the burst in the H -band (Tanvir et al. 2013). At that time, its luminosity in the same band is ~ 3 times brighter than AT2017gfo (see Fig. A3).

In the case of GRB 150101B the r -band light curve has a decay index $\alpha \sim 1$ between 35 and 56 hours after the trigger which is above the shallow decay limit. Troja et al. (2018a) show that this light curve is compatible with the late evolution of the blue component of AT2017gfo, well after the peak emission. We find that if a blue kilonova is the dominant component, it is brighter than AT2017gfo by a factor ~ 2 at ~ 35 hours after the trigger. Moreover, the deep and late upper limits confirm that no emission from an underlying host is affecting the early data.

5 DISCUSSION

In the following we first discuss those GRBs that are fainter than AT2017gfo, without considering those with uncertain redshift. Afterwards, we will discuss the cases with shallow decay or with a claimed kilonova, by defining a golden sample of GRBs with accurate redshifts and by using their luminosity to constrain that of AT2017gfo-like blue and red kilonova components.

5.1 Upper limits to AT2017gfo-like kilonovae

In the previous section (§4.1) we show that in seven cases an AT2017gfo-like emission could have been detected since its expected luminosity is well above the observed optical counterpart luminosity (see Tab. 2 and Tab. A1). In particular, we note that in two cases (GRBs 050509B and 061201) if a kilonova was present, it should be less luminous than AT2017gfo up to more than a factor of 5 for the blue component (see also Gompertz et al. 2018). In the following, we will consider only those with accurate redshift determination (see §2.3), which are GRB 050509B, 050709, 100206A and 160821B. The counterpart luminosity of these four GRBs enable us to robustly set constraining upper limits to a possible underlying kilonova component that is fainter than AT2017gfo (see also Dichiaro et al. 2019).

In Figure 6 we compare their optical and NIR counterpart luminosity with the blue and red component of AT2017gfo (the spectral bands of the blue and red component have been defined in §4). In the blue component spectral band, the strongest constrain is given by GRB 050509B that is more than 5 times fainter than AT2017gfo ~ 35 hours after the trigger. GRBs 100206A and 050709 are marginally fainter and still comparable in luminosity to AT2017gfo at 12 and ~ 50 hours after the trigger, respectively.

For the red component, GRB 160821B was fainter than AT2017gfo, although its blue component has similar luminosity. The deepest and earliest constraint is a factor ~ 2

fainter than AT2017gfo at $\sim 1000\text{nm}$ at ~ 78 hours after the burst, close to the actual NIR peak of AT2017gfo, indicating that in this case the red kilonova is at least partially suppressed. Intriguingly, in the bottom right panel in figure 6 we show that there are no NIR upper limits below AT2017gfo luminosity after ~ 50 hours (see also §5.2.1). The same is not true in the left panel, where upper limits exist below AT2017gfo luminosity level, thus possibly suggesting a larger range of luminosity for the blue counterpart with respect to the red one.

5.2 Golden sample of GRBs with kilonova candidates

Past evidence of kilonova emission was found in the GRB optical counterparts of 6 short GRBs (050709A, 060614A, 080503, 130603B, 150101B, and 160821B; see §1 and references therein). In addition to those, there are the magnetar-powered kilonovae identified by Gao et al. (2017) (GRBs 050724, 070714B). In all cases but GRB 080503 the redshift is well defined. Therefore, we define a golden sample that includes all 7 GRBs with kilonova candidates claimed in the literature that have accurate redshift.

5.2.1 Interesting extreme events

We define "extreme" events those cases in our golden sample that are more than 10 times brighter or fainter than AT2017gfo either in the blue and/or in the red bands. We find two cases with a bright blue counterpart, namely GRBs 060614 and 070714B.

Concerning GRB 060614, in this work we show that its optical light curve has a shallow decay until 10 hours after the trigger (rest-frame; see §4.2) and the blue counterpart is 17 times brighter than AT2017gfo at 13 hours (i.e. at the end of the shallow decay). We note that a kilonova has been found by Yang et al. (2015) but dominating 3 days after the GRB, with a peak in the infrared (Jin et al. 2015). In Mangano et al. (2007) the early optical behaviour of GRB 060614 is explained as the counterpart of the plateau observed in X-rays. However, the similarity of the optical and X-ray light curves of GRB 060614 with GRB 050724 (see also Fig. A2), for which a MKN was claimed by Gao et al. (2017), may support the blue component interpretation of the early emission for both cases.

The blue counterpart of GRB 070714B is between 10 and ~ 260 times brighter than AT2017gfo between 11 and 55 hours (§4.3). During this time Gao et al. (2017) propose that a MKN is dominating. They show that the peak bolometric luminosity of MKNs is $\gtrsim 10$ times more luminous than other kilonovae like the one associated to 050709, which we find more similar to AT2017gfo. This is also the case for the MKN associated GRB 050724, which instead is more similar to AT2017gfo in our analysis (see §5.2). However, the proposed MKN peaks at ~ 0.5 days, i.e. too early for a comparison with AT2017gfo

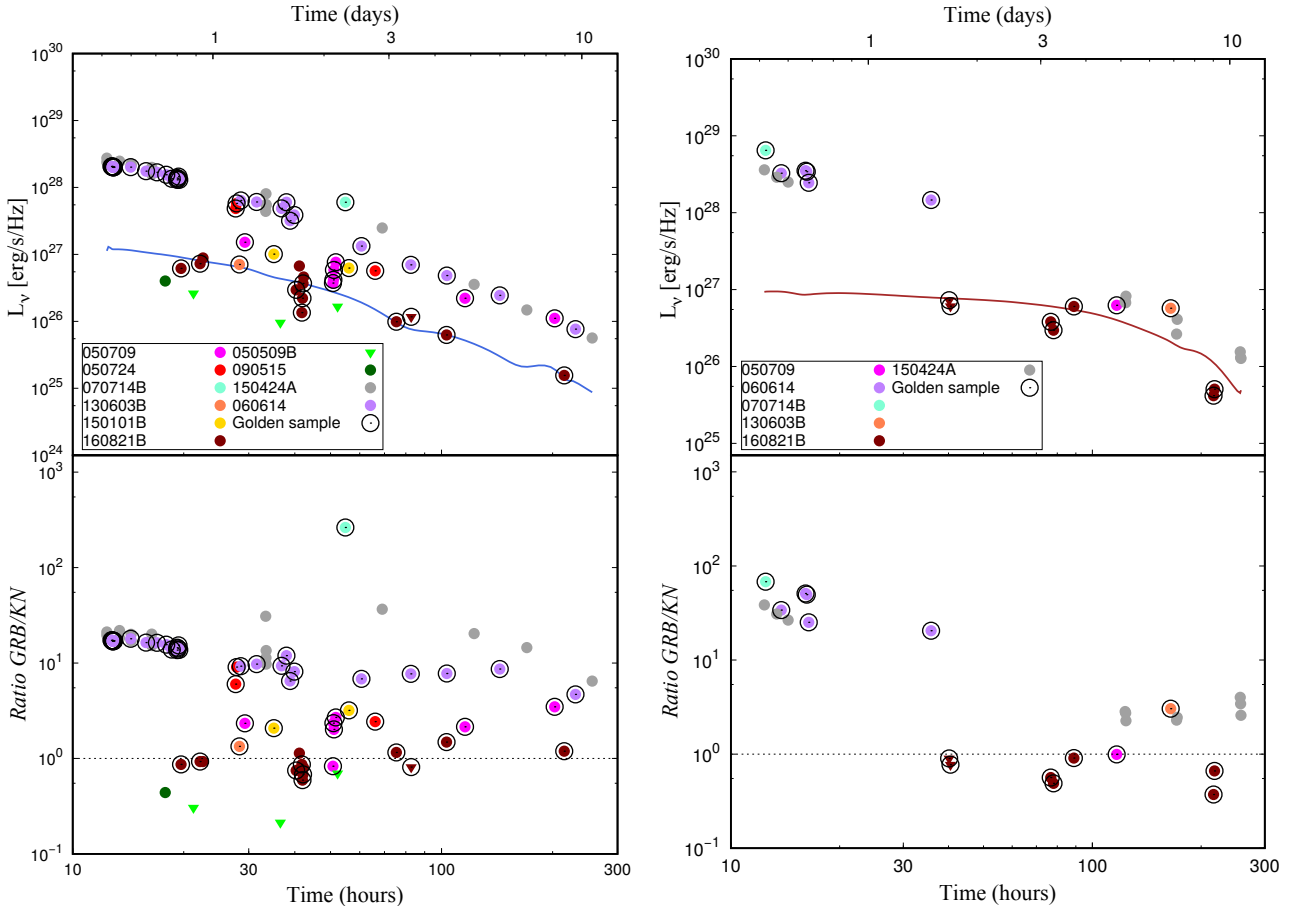


Figure 6. luminosity (*top*) and luminosity ratios (*bottom*) of GRB and AT2017gfo versus time from merger. Data are taken from Table A1 after shifting the effective wavelengths of the filter bands to the rest frame value. The whole analysed sample is plotted in blue (*left*) and red (*right*) where the colour code indicates two different spectral bands (blue: < 900 nm, red: > 900 nm). Upper limits are indicated as downward triangles and **only when below AT2017gfo luminosity**. Short GRBs with anomalous shallow decay are highlighted with different colours, including those without a well defined redshift. Bursts which belong to our golden sample are highlighted with a black circle (see 5.2). The blue and red solid lines in the top panels indicate the AT2017gfo luminosity at 800 nm and 1600 nm wavelength, respectively.

templates, and afterwards it decays rapidly. Therefore, our analysis cannot constrain the peak bolometric luminosity.

In the NIR band, all the kilonovae detected (GRBs 050709, 130603B, 160821B, §4.3), are no more than 3 times brighter or fainter than AT2017gfo during the time where the red kilonova dominates (after 1 day, see Jin et al. 2016; Tanvir et al. 2013; Lamb et al. 2019). Moreover, as we noted already in § 5.1, there are no upper limits in the NIR comparable to AT2017gfo luminosity after ~ 2 days. In other words, in all cases when observations comparable to AT2017gfo NIR emission exist the kilonova counterpart has been detected. This suggests that all red kilonova detected so far have similar luminosity, although we are aware that the numbers are not high enough for a meaningful statistic.

5.3 Interesting events without accurate redshifts

The redshifts of GRBs 090515 and 150424A are not well defined (see § 2.3), nevertheless they can be useful to constrain the luminosity of AT2017gfo-like kilonovae since both show evidence of shallow decay that can suggest the presence of a kilonova component. In particular, GRB 090515 is the most interesting because the blue component have a well constrained luminosity 2.3 times fainter than AT2017gfo (Fig. 5). If its redshift is correct, together with 050509B it would provide the strongest and earliest constraints to the blue component of an AT2017gfo-like kilonova (Fig. 6).

GRB 150424A has a shallow decay but its blue component is ~ 15 -40 times brighter than AT2017gfo in the optical (Fig. 6). During the same time interval the X-ray light curve shows evidence of a plateau feature. This could be a MKN similar to GRBs 050724, 070714B and 060614 (§ 5.2.1), although Knust et al. (2017) found that energy injection from a down spinning magnetar can explain X-rays, optical, and NIR data without invoking a kilonova.

A more detailed analysis is needed to separate the kilonova and afterglow components modelling together both optical and X-ray data (see e.g., Jin et al. 2019; Gao et al. 2017; Lamb et al. 2019). Unfortunately, in case of GRB 090515 the X-ray data is weak and detected only during the first hour.

5.4 Interpreting the large range of luminosity

AT2017gfo is the only kilonova that has been very well sampled and studied so far, but it is a one-of-its-kind example and other kilonovae may differ for their evolution and colours. Providing a theoretical explanation for kilonovae tens times brighter than AT2017gfo is beyond the scope of this paper. However, in the following we describe the possible causes to the large range in luminosity that we have found.

According to the most accredited model (e.g., Mooley et al. 2018b; Ghirlanda et al. 2019), AT2017gfo was observed ~ 15 degrees off-axis while here we are comparing it with likely on-axis events (see also Bulla et al. 2018; Mandel 2018). A kilonova luminosity gradient at a given wavelength is expected between the polar and the equatorial direction of the binary plane system, and many parameters including its magnitude depend on the fate of the central remnant (e.g., Kasen et al. 2017; Radice et al. 2018). According to recent numerical computations (see e.g., figure 24 in Radice et al. 2018), in the case of a binary NS system (BNS) promptly forming a BH the result is an overall decrease of luminosity by less than a factor 2 (i.e., ~ 0.5 mag) **in the polar direction with respect to the equatorial one. Accounting for an off-axis inclination like AT2017gfo, then the polar emission should be less than 2 times fainter.** This is not enough to explain the low luminosity ratio of those GRBs with optical counterpart fainter than AT2017gfo (Tab. 2). In the case of an hyper massive NS (HMNS) or a stable NS being formed, then the polar luminosity should increase in the rest-frame g and z bands by a factor of less than 1.5 **with respect to the equatorial direction** (i.e., a decrement of $\Delta g \leq 0.4$ mag and $\Delta z \leq 0.2$ mag). **Again,** this factor is not high enough to explain the measured large luminosity ratios for the peculiar events we describe in § 5.2.1. We conclude that, in the prompt BH formation case we cannot explain the measured luminosity gradient for any viewing angle and even assuming a central HMNS formation before the collapse to a BH, the viewing angle correction factors are not large enough to recover the observed luminosity gradients (Tab. 2).

A possible solution to explain the faint emission of the kilonova associated with the 7 GRBs for which the optical counterpart was fainter than AT2017gfo may invoke not only a different viewing angle but also a different progenitor, i.e. NS-BH instead of BNS, where larger opacities are expected with respect to a NS-NS merger case (Kasen et al. 2015; Metzger 2017; Barbieri et al. 2019). Although in the most dramatic cases lower masses and velocities of the ejecta can play an important role (e.g., Dichiaro et al. 2019), any further investigation is beyond the scope of this paper.

On the other side, a possible explanation for the largest luminosity ratios may invoke the presence of a long-lived NS remnant that can alter the kilonova luminosity. In this case, its spin-down emission could illu-

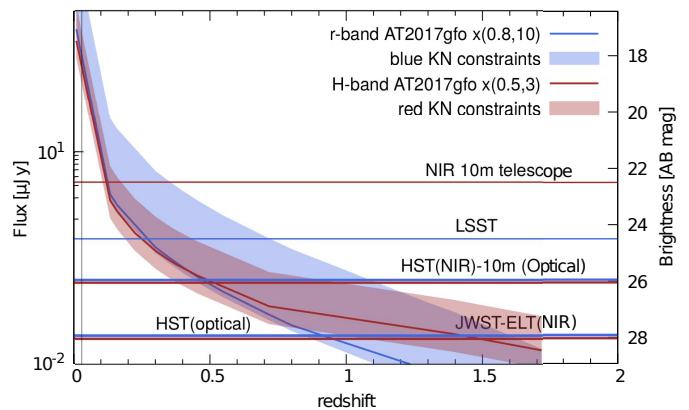


Figure 7. Peak brightness of AT2017gfo in the r (green) and H (red) bands at different redshifts, within the constraints we derived for an AT2017gfo-like kilonova from the golden sample. The redshift range is limited to $z \sim 2$ at which ET will be able to observe a GW signal from a merging BNS. The vertical line is the aLIGO/AVirgo detection limits for a BNS event. The horizontal lines are different detection limits for different class of telescopes with an exposure time of 10 minutes.

minate the ejecta on timescales much longer (up to hours or even more) than the typical timescale of baryon wind ejection and neutrino irradiation (less than few seconds), effectively increasing the ejecta kinetic and thermal energy and thus potentially altering the brightness of the corresponding KN (e.g., Metzger & Piro 2014; Gao et al. 2017).

A highly magnetised millisecond pulsar (a magnetar) has been previously proposed to explain the plateaus observed in the X-ray light curves of GRBs, where the magnetar loses energy via dipole radiation and thus provides the energy to sustain the X-ray plateau phase (Zhang & Mészáros 2001; Yu et al. 2013; Metzger & Piro 2014; Siegel & Ciolfi 2016a,b). Note that an X-ray plateau was found in the light curves of GRBs 060614A (Mangano et al. 2007; Stratta et al. 2018b), and 150424 (Knust et al. 2017) that show a blue component brighter than AT2017gfo. Therefore, it is possible that what we observed in these cases was a BNS merger exploding as a short GRB with a bright X-ray plateau and an luminosity-enhanced blue kilonova, leaving a magnetar as the final remnant of the merger, **similarly to what proposed by Gao et al. (2017) for GRB 050724.**

5.5 Future perspectives for high redshift events

In the following, we want to investigate up to which redshift a kilonova can be followed-up, considering the current and future optical and NIR facilities. In doing so we do not consider the challenge to search and identify a kilonova within the error boxes given by the GW detectors (e.g., Brocato et al. 2018).

In Fig. 7 we show the maximum brightness of AT2017gfo in the observed r -band (at 12 hours in the rest frame) and H -band (at 58 hours in the rest frame) up to the redshift at which the future Einstein Telescope (ET; Sathyaprakash et al. 2012) will be able to observe a GW signal from a merging BNS ($z \sim 2$). In light of the results from the section 5.2, and conservatively assuming that the

blue kilonova is brighter up to 10 times AT2017gfo, we can constrain the peak luminosity of the blue kilonova between 0.8 and 10 times that of AT2017gfo and for the red component between 0.5 and 3 times. These constrain identify blue and red colored regions in figure 7. We put a lower limit to the $3\text{-}\sigma$ detection with the current largest ground-based and orbiting telescopes dedicated to the characterization of the source: e.g., VLT, LBT ($r = 26$, $H = 23$ mag in the AB system), and the Hubble space telescope (HST) along with the forthcoming LSST (Ivezić et al. 2019; $r = 25$) and ELT (Spyromilio et al. 2008) ground-based telescopes and the JWST (Gardner et al. 2006) space telescope ($H \sim 28$ mag, AB system) assuming 10 min exposure time (see also Maiorano et al. 2018). An AT2017gfo-like kilonova would be detectable up to redshift 0.5 in the optical and 0.2 in the NIR by ground-based very large telescopes. The JWST will be able to detect AT2017gfo at redshift larger than one.

From figure 7, we note that a AT2017gfo-like kilonova would be brighter in NIR bands at redshift larger than ~ 0.5 , but only the JWST or the ELT would be able to detect this emission. Note that the current largest telescopes are able to detect the brightest AT2017gfo-like blue kilonovae above $z = 1$, a distance at which only HST is able to detect the brightest red kilonovae. The situation will improve when, thanks to JWST and ELT, we will be able to detect a kilonova up to $z \sim 0.7 - 1.6$ for the blue component and $z \sim 1 - 2$ for the red component (Fig. 7). This shows that follow-up of GRB/kilonovae with large-size ground-based telescopes and space observatories at redshifts beyond that of AT2017gfo is possible, although in most cases it can be difficult to distinguish the GRB afterglow from the kilonova component.

Again, we stress that the real challenge will be to search and identify a kilonova within the error boxes given by the GW detectors. Distant GW sources ($z > 0.5$) will be discovered only with interferometers of third generation as ET and will be localised within several thousands square degrees with a single interferometer and within few tens of square degrees with three detector network (e.g. Chan et al. 2018). Therefore, only the association with a GRB will permit to localize high-redshift kilonovae with enough accuracy. This can be provided by future space-based GRB dedicated missions as for example THESEUS (Amati et al. 2018; Stratta et al. 2018a; Rossi et al. 2018a).

6 SUMMARY AND CONCLUSIONS

The discovery of GW170817 and GRB 170817A has provided the first direct evidence of the association of at least a fraction of short GRBs with binary NS merging systems. It also provided the most compelling evidence that kilonova emission may be an additional component in sGRB optical/NIR afterglows. Motivated by this discovery, we have searched for AT2017gfo-like kilonova emissions in the optical/NIR light curves of 39 short GRBs with known redshift, using optical and NIR rest-frame light curves obtained from the spectroscopic and photometric data-set of AT2017gfo.

In addition to past works, due to the large spectral coverage of our data sample, we were able to confirm the presence of a significant kilonova luminosity gradient for both

the blue and red components. Our main results and conclusions are summarized in Figure 8 and below:

- *We find robust evidence that not all short GRBs are associated with a AT2017gfo-like kilonova. Indeed, we find 7 events in which the GRB optical counterpart is less luminous than AT2017gfo in at least one filter (pink slices in Fig. 8). For these cases, if an AT2017gfo-like kilonova were present, it should had been detected. In particular for two GRBs with accurate redshift (050509B and 061201), the optical counterpart luminosity is fainter than AT2017gfo by a factor up to > 5 for the blue component (see Figure 6 and Tab.2).*

- *We find evidence for a significant kilonova luminosity gradient for the blue component. In 7% of the cases with well-defined redshift (GRBs 050709 and 160821B), the kilonova luminosity is fainter than AT2017gfo (violet slice in Fig. 8) while 18% is brighter (bright cyan slice), providing evidence for a luminosity range of $\sim [0.6 - 17]$ times the AT2017gfo luminosity for the blue component and more than 200 times in the case of the claimed magnetar-powered kilonova of GRB 070714B. (see Fig. 6 and Tab.2). These percentages become 8% (fainter) and 20% (brighter) if we consider all the sample (i.e., also those GRBs with not well-defined redshift). As noted by others, a different observer angle is not sufficient to explain the measured luminosity range (e.g., Gompertz et al. 2018), and the central remnant can play a role (e.g., Metzger et al. 2018; Ascenzi et al. 2019). In particular, it is possible that if a magnetar forms after the merger even for a short time, it can inject energy in the blue kilonova emission (e.g., Gao et al. 2017).*

- *We find evidence for a similar kilonova luminosity for all kilonovae detected in the NIR (the red component). In three cases (GRBs 050709, 130603B, 160821B) the kilonova is detected in the NIR after ~ 2 days, and it is less than a factor $\sim [0.5 - 3]$ times the AT2017gfo luminosity. Although the numbers are small, this suggests that the red component is similar in luminosity to AT2017gfo.*

By taking into account a conservative range of blue luminosity for the kilonova, we estimate up to which redshift the kilonova peak brightness can be detected with current and future facilities. We find that for example with the ELT and JWST we will be able to follow-up a kilonova with redshift $z \sim 1 - 2$ (Fig. 7). The precise sky localization for the kilonova follow-up will be provided by the associated GRB and afterglow that will be detected by future space-based GRB dedicated missions as for example THESEUS.

ACKNOWLEDGEMENTS

The authors thank the anonymous referee for a very constructive report. We thank D. Radice for useful discussion about the kilonova models, and G. Raimondo for valuable suggestions. A. Rossi acknowledges support from Premiale LBT 2013. We acknowledge support from the PRIN-INAF SKA-CTA 2016 project ‘‘Toward the SKA and CTA era: discovery, localization, and physics of transient sources’’. This work made use of the Weizmann interactive super-

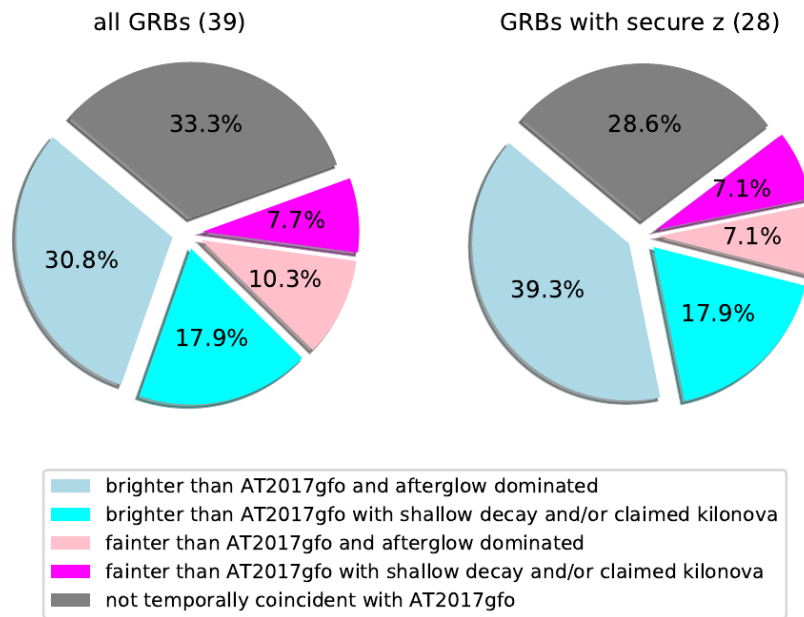


Figure 8. Pie-chart summary of analysed short GRBs with optical counterpart brighter, or fainter in at least one filter, than AT2017gfo, and with claimed evidence of kilonovae and/or evidence of shallow decay. We also show all short GRBs with no evidence of kilonova or shallow decay, that we call *afterglow dominated*, and those with no data in the temporal window where AT2017gfo was sampled, that we call *not temporally coincident with AT2017gfo*.

nova data repository - <http://wiserep.weizmann.ac.il>. This research has made use of the NASA/IPAC Infrared Science Archive, which is operated by the Jet Propulsion Laboratory, California Institute of Technology, under contract with the National Aeronautics and Space Administration.

REFERENCES

- Abbott B. P., et al., 2017a, *Physical Review Letters*, **119**, 161101
- Abbott B. P., et al., 2017b, *ApJ*, **848**, L12
- Abbott B. P., et al., 2017c, *ApJ*, **848**, L13
- Acernese F., et al., 2015, *Classical and Quantum Gravity*, **32**, 024001
- Amati L., et al., 2002, *A&A*, **390**, 81
- Amati L., et al., 2018, *Advances in Space Research*, **62**, 191
- Andreoni I., et al., 2017, *Publ. Astron. Soc. Australia*, **34**, e069
- Antonelli L. A., et al., 2009, *A&A*, **507**, L45
- Arcavi I., 2018, *ApJ*, **855**, L23
- Arcavi I., et al., 2017, *Nature*, **551**, 64
- Ascenzi S., et al., 2019, *MNRAS*, **486**, 672
- Barbieri C., Salafia O. S., Perego A., Colpi M., Ghirlanda G., 2019, *A&A*, **625**, A152
- Barnes J., Kasen D., Wu M.-R., Martínez-Pinedo G., 2016, *ApJ*, **829**, 110
- Berger E., 2010, *ApJ*, **722**, 1946
- Berger E., et al., 2007, *ApJ*, **664**, 1000
- Berger E., et al., 2013a, *ApJ*, **765**, 121
- Berger E., Fong W., Chornock R., 2013b, *ApJ*, **774**, L23
- Bernardini M. G., et al., 2015, *MNRAS*, **446**, 1129
- Blanton M. R., Roweis S., 2007, *AJ*, **133**, 734
- Bloom J. S., Kulkarni S. R., Djorgovski S. G., 2002, *AJ*, **123**, 1111
- Bloom J. S., et al., 2006, *ApJ*, **638**, 354
- Brocato E., et al., 2018, *MNRAS*, **474**, 411
- Bromberg O., Nakar E., Piran T., Sari R., 2012, *ApJ*, **749**, 110
- Bulla M., et al., 2018, *Nature Astronomy*, **2**, 102
- Cantiello M., et al., 2018, *ApJ*, **854**, L31
- Cardelli J. A., Clayton G. C., Mathis J. S., 1989, *ApJ*, **345**, 245
- Castro-Tirado A. J., et al., 2005, *A&A*, **439**, L15
- Castro-Tirado A. J., Sanchez-Ramirez R., Lombardi G., Rivero M. A., 2015, GRB Coordinates Network, Circular Service, No. 17758, #1 (2015), 17758
- Chan M. L., Messenger C., Heng I. S., Hendry M., 2018, *Phys. Rev. D*, **97**, 123014
- Chornock R., Fong W., 2015, GRB Coordinates Network, **17358**, 1
- Chornock R., Lunnan R., Berger E., 2013, GRB Coordinates Network, 15307, 1
- Chornock R., Fong W., Fox D. B., 2014, GRB Coordinates Network, **17177**, 1
- Chornock R., et al., 2017, *ApJ*, **848**, L19
- Coulter D. A., et al., 2017, *Science*, **358**, 1556
- Covino S., et al., 2017, *Nature Astronomy*, **1**, 791
- Cowperthwaite P. S., et al., 2017, *ApJ*, **848**, L17
- Cucchiara A., Levan A. J., 2016, GRB Coordinates Network, Circular Service, No. 19565, #1 (2016), 19565
- D’Avanzo P., et al., 2009, *A&A*, **498**, 711
- D’Avanzo P., et al., 2014, *MNRAS*, **442**, 2342
- D’Avanzo P., et al., 2018, *A&A*, **613**, L1
- D’Elia V., D’Avanzo P., Malesani D., di Fabrizio L., Tassinari G., 2013, GRB Coordinates Network, 15310, 1
- Della Valle M., et al., 2006, *Nature*, **444**, 1050
- Dichiara S., Troja E., O’Connor B., Marshall F. E., Beniamini P., Cannizzo J. K., Lien A. Y., Sakamoto T., 2019, arXiv e-prints, p. [arXiv:1912.08698](https://arxiv.org/abs/1912.08698)
- Drout M. R., et al., 2017, *Science*, **358**, 1570
- Evans P. A., et al., 2017, *Science*, **358**, 1565
- Fernández R., Metzger B. D., 2016, *Annual Review of Nuclear and Particle Science*, **66**, 23
- Fong W., Berger E., 2013, *ApJ*, **776**, 18
- Fong W., et al., 2013, *ApJ*, **769**, 56
- Fong W., Berger E., Margutti R., Zauderer B. A., 2015, *ApJ*, **815**, 102
- Fong W., et al., 2016, *ApJ*, **833**, 151

- Fong W., et al., 2017, *ApJ*, **848**, L23
- Fox D. B., et al., 2005, *Nature*, **437**, 845
- Fynbo J. P. U., et al., 2006, *Nature*, **444**, 1047
- Gao H., Zhang B., Lü H.-J., Li Y., 2017, *ApJ*, **837**, 50
- Gardner J. P., et al., 2006, *Space Science Reviews*, **123**, 485
- Ghirlanda G., et al., 2019, *Science*, **363**, 968
- Goldstein A., et al., 2017, *ApJ*, **848**, L14
- Gompertz B. P., et al., 2018, *ApJ*, **860**, 62
- Guillochon J., Parrent J., Kelley L. Z., Margutti R., 2017, *ApJ*, **835**, 64
- Hallinan G., et al., 2017, *Science*, **358**, 1579
- Hjorth J., et al., 2003, *Nature*, **423**, 847
- Hjorth J., et al., 2005, *ApJ*, **630**, L117
- Hjorth J., et al., 2017, *ApJ*, **848**, L31
- Ivezić Ž., et al., 2019, *ApJ*, **873**, 111
- Izzo L., Cano Z., de Ugarte Postigo A., Kann D. A., Thoene C., Geier S., 2017, GRB Coordinates Network, Circular Service, 21059
- Jin Z.-P., Li X., Cano Z., Covino S., Fan Y.-Z., Wei D.-M., 2015, *ApJ*, **811**, L22
- Jin Z.-P., et al., 2016, *Nature Communications*, **7**, 12898
- Jin Z.-P., et al., 2018, *ApJ*, **857**, 128
- Jin Z.-P., Covino S., Liao N.-H., Li X., D’Avanzo P., Fan Y.-Z., Wei D.-M., 2019, *Nature Astronomy*, p. 461
- Kann D. A., et al., 2011, *ApJ*, **734**, 96
- Kasen D., Fernández R., Metzger B. D., 2015, *MNRAS*, **450**, 1777
- Kasen D., Metzger B., Barnes J., Quataert E., Ramirez-Ruiz E., 2017, *Nature*, **551**, 80
- Kasliwal M. M., et al., 2017a, *Science*, **358**, 1559
- Kasliwal M. M., Korobkin O., Lau R. M., Wollaeger R., Fryer C. L., 2017b, *ApJ*, **843**, L34
- Kathirgamaraju A., Barniol Duran R., Giannios D., 2018, *MNRAS*, **473**, L121
- Kathirgamaraju A., Tchekhovskoy A., Giannios D., Barniol Duran R., 2019, *MNRAS*, **484**, L98
- Knust F., et al., 2017, *A&A*, **607**, A84
- Kocevski D., et al., 2010, *MNRAS*, **404**, 963
- Kouveliotou C., Meegan C. A., Fishman G. J., Bhat N. P., Briggs M. S., Koshut T. M., Paciesas W. S., Pendleton G. N., 1993, *ApJ*, **413**, L101
- LIGO Scientific Collaboration et al., 2015, *Classical and Quantum Gravity*, **32**, 074001
- Lamb G. P., et al., 2019, *ApJ*, **883**, 48
- Levan A. J., Wiersema K., Tanvir N. R., Malesani D., Xu D., de Ugarte Postigo A., 2016, GRB Coordinates Network, Circular Service, No. 19846, #1 (2016), 19846
- Li L.-X., Paczyński B., 1998, *ApJ*, **507**, L59
- Lyman J. D., et al., 2018, *Nature Astronomy*, **2**, 751
- Maiorano E., Amati L., Rossi A., Stratta G., Palazzi E., Nicastro L., 2018, *Mem. Soc. Astron. Italiana*, **89**, 181
- Malesani D., et al., 2007, *A&A*, **473**, 77
- Malesani D., D’Avanzo P., D’Elia V., Vergani S. D., Andreuzzi G., Garcia A., Escudero G., Bonomo A., 2014, GRB Coordinates Network, **17170**, 1
- Malesani D., et al., 2015, GRB Coordinates Network, **17755**, 1
- Mandel I., 2018, *The Astrophysical Journal*, **853**, L12
- Mangano V., et al., 2007, *A&A*, **470**, 105
- Margutti R., et al., 2012, *ApJ*, **756**, 63
- Margutti R., et al., 2018, *ApJ*, **856**, L18
- Metzger B. D., 2017, *Living Reviews in Relativity*, **20**, 3
- Metzger B. D., Piro A. L., 2014, *MNRAS*, **439**, 3916
- Metzger B. D., et al., 2010, *MNRAS*, **406**, 2650
- Metzger B. D., Thompson T. A., Quataert E., 2018, *ApJ*, **856**, 101
- Mooley K. P., et al., 2018a, *Nature*, **554**, 207
- Mooley K. P., et al., 2018b, *Nature*, **561**, 355
- Nicuesa Guelbenzu A., et al., 2011, *A&A*, **531**, L6
- Nicuesa Guelbenzu A., et al., 2012a, *A&A*, **538**, L7
- Nicuesa Guelbenzu A., et al., 2012b, *A&A*, **548**, A101
- Perego A., Radice D., Bernuzzi S., 2017, *ApJ*, **850**, L37
- Pérez-Ramírez D., et al., 2013, in Castro-Tirado A. J., Gorosabel J., Park I. H., eds, *EAS Publications Series Vol. 61*, *EAS Publications Series*. pp 345–349, doi:10.1051/eas/1361055
- Perley D. A., 2015, GRB Coordinates Network, Circular Service, No. 17744, #1 (2015), 17744
- Perley D. A., Cenko S. B., 2015, GRB Coordinates Network, **17312**, 1
- Perley D. A., et al., 2009, *ApJ*, **696**, 1871
- Perley D. A., Modjaz M., Morgan A. N., Cenko S. B., Bloom J. S., Butler N. R., Filippenko A. V., Miller A. A., 2012, *ApJ*, **758**, 122
- Pian E., et al., 2017, *Nature*, **551**, 67
- Piro L., et al., 2019, *MNRAS*, **483**, 1912
- Planck Collaboration: Ade P. A. R., et al., 2016, *A&A*, **594**, A13
- Price P. A., Berger E., Fox D. B., 2006, GRB Coordinates Network, **5275**
- Radice D., Perego A., Hotokezaka K., Fromm S. A., Bernuzzi S., Roberts L. F., 2018, *ApJ*, **869**, 130
- Rossi A., Stratta G., Maiorano E., Amati L., Nicastro L., Palazzi E., 2018a, *Mem. Soc. Astron. Italiana*, **89**, 254
- Rossi A., et al., 2018b, GRB Coordinates Network, Circular Service, 22763
- Rowlinson A., et al., 2010, *MNRAS*, **409**, 531
- Sakamoto T., et al., 2013, *ApJ*, **766**, 41
- Salafia O. S., Ghirlanda G., Ascenzi S., Ghisellini G., 2019, *A&A*, **628**, A18
- Sari R., Piran T., Narayan R., 1998, *ApJ*, **497**, L17
- Sari R., Piran T., Halpern J. P., 1999, *ApJ*, **519**, L17
- Sathyaprakash B., et al., 2012, *Classical and Quantum Gravity*, **29**, 124013
- Savchenko V., et al., 2017, *ApJ*, **848**, L15
- Schlaflly E. F., Finkbeiner D. P., 2011, *ApJ*, **737**, 103
- Selsing J., et al., 2018, *A&A*, **616**, A48
- Selsing J., et al., 2019, *A&A*, **623**, A92
- Siegel D. M., Ciolfi R., 2016a, *ApJ*, **819**, 14
- Siegel D. M., Ciolfi R., 2016b, *ApJ*, **819**, 15
- Smartt S. J., et al., 2017, *Nature*, **551**, 75
- Spyromilio J., Comerón F., D’Odorico S., Kissler-Patig M., Gilmozzi R., 2008, *The Messenger*, **133**, 2
- Stratta G., et al., 2007, *A&A*, **474**, 827
- Stratta G., et al., 2018a, *Advances in Space Research*, **62**, 662
- Stratta G., Dainotti M. G., Dall’Osso S., Hernandez X., De Cesare G., 2018b, *ApJ*, **869**, 155
- Tanaka M., et al., 2018, *ApJ*, **852**, 109
- Tanvir N. R., et al., 2010, GRB Coordinates Network, Circular Service, No. 11123, #1 (2010), 11123
- Tanvir N. R., Levan A. J., Fruchter A. S., Hjorth J., Hounsell R. A., Wiersema K., Tunnicliffe R. L., 2013, *Nature*, **500**, 547
- Tanvir N. R., et al., 2015, GRB Coordinates Network, Circular Service, No. 18100, #1 (2015), 18100
- Tanvir N. R., et al., 2017, *ApJ*, **848**, L27
- Troja E., et al., 2016, *ApJ*, **827**, 102
- Troja E., et al., 2017, *Nature*, **551**, 71
- Troja E., et al., 2018a, *Nature Communications*, **9**, 4089
- Troja E., et al., 2018b, *MNRAS*, **478**, L18
- Troja E., et al., 2019, *MNRAS*, **489**, 2104
- Varela K., Knust F., Greiner J., 2015, GRB Coordinates Network, **17732**, 1
- Villar V. A., et al., 2017, *ApJ*, **851**, L21
- Watson D., Hjorth J., Jakobsson P., Xu D., Fynbo J. P. U., Sollerman J., Thöne C. C., Pedersen K., 2006, *A&A*, **454**, L123
- Xu D., et al., 2009, *ApJ*, **696**, 971
- Yang B., et al., 2015, *Nature Communications*, **6**, 7323
- Yaron O., Gal-Yam A., 2012, *PASP*, **124**, 668
- Yonetoku D., Murakami T., Nakamura T., Yamazaki R., Inoue A. K., Ioka K., 2004, *ApJ*, **609**, 935

- Yu Y.-W., Zhang B., Gao H., 2013, *ApJ*, **776**, L40
Zhang B., Mészáros P., 2001, *ApJ*, **552**, L35
Zhang B., Mészáros P., 2004, *International Journal of Modern Physics A*, **19**, 2385
Zhang B., Fan Y. Z., Dyks J., Kobayashi S., Mészáros P., Burrows D. N., Nousek J. A., Gehrels N., 2006, *ApJ*, **642**, 354
de Ugarte Postigo A., et al., 2014, *A&A*, **563**, A62

APPENDIX A: ADDITIONAL MATERIAL

Table A1: Table with GRB and AT2017gfo luminosity ratios

GRB	time hr	Band eff.	L_{GRB} 10^{26} erg/s Hz $^{-1}$	L_{KN} 10^{26} erg/s Hz $^{-1}$	L_{GRB}/L_{kn}	z	λ_{rest} nm	λ_{obs} nm
050509B	40.9	g*	< 3.21	1.24	< 2.59	0.225	391.7	479.8
050509B	77.1	V	< 0.50	0.36	< 1.38	0.225	454.9	557.1
050509B	155.6	V	< 5.01	0.08	< 59.43	0.225	454.9	557.1
050509B	233.0	V	< 10.50	0.08	< 123.82	0.225	454.9	557.1
050509B	16.1	R	< 60.60	10.50	< 5.77	0.225	523.5	641.2
050509B	21.2	R	< 2.62	8.58	< 0.31	0.225	523.5	641.2
050509B	36.6	R	< 0.96	4.50	< 0.21	0.225	523.5	641.2
050509B	40.9	R	< 7.22	3.91	< 1.85	0.225	523.5	641.2
050509B	52.2	R	< 1.67	2.39	< 0.70	0.225	523.5	641.2
050509B	156.9	R	< 4.55	0.17	< 26.76	0.225	523.5	641.2
050509B	191.9	I	< 57.10	0.29	< 194.22	0.225	645.5	790.6
050509B	16.4	J	< 68.70	9.65	< 7.12	0.225	1023.5	1253.5
050509B	34.1	J	< 157.00	8.23	< 19.08	0.225	1023.5	1253.5
050509B	132.7	J	< 43.30	2.89	< 14.98	0.225	1023.5	1253.5
050509B	172.3	J	< 27.30	1.38	< 19.78	0.225	1023.5	1253.5
050509B	14.2	H	< 110.00	9.37	< 11.74	0.225	1348.3	1651.5
050509B	18.4	H	< 83.70	9.39	< 8.91	0.225	1348.3	1651.5
050509B	73.4	H	< 101.00	6.80	< 14.85	0.225	1348.3	1651.5
050509B	15.8	K	< 262.00	7.88	< 33.25	0.225	1764.6	2161.2
050709	38.2	V	< 53.60	3.17	< 16.91	0.161	480.0	557.1
050709	50.9	V	4.17 ± 0.46	1.78	2.34	0.161	480.0	557.1
050709	90.2	V	< 2.34	0.29	< 7.96	0.161	480.0	557.1
050709	216.8	V	< 3.89	0.11	< 35.36	0.161	480.0	557.1
050709	23.7	R	< 82.20	7.87	< 10.44	0.161	552.5	641.2
050709	24.5	R	< 327.00	7.64	< 42.80	0.161	552.5	641.2
050709	25.5	R	< 47.30	7.40	< 6.39	0.161	552.5	641.2
050709	29.3	R	15.20 ± 0.78	6.51	2.33	0.161	552.5	641.2
050709	51.1	R	5.86 ± 0.33	2.91	2.01	0.161	552.5	641.2
050709	51.7	R	7.62 ± 1.69	2.83	2.69	0.161	552.5	641.2
050709	137.4	R	< 1.43	0.27	< 5.28	0.161	552.5	641.2
050709	152.6	R	< 4.73	0.21	< 22.96	0.161	552.5	641.2
050709	173.2	R	< 47.30	0.18	< 259.89	0.161	552.5	641.2
050709	216.7	R	< 2.98	0.16	< 18.74	0.161	552.5	641.2
050709	25.6	i*	< 155.00	8.66	< 17.90	0.161	659.6	765.5
050709	50.8	I	3.73 ± 0.75	4.50	0.83	0.161	681.2	790.6
050709	90.4	I	< 3.73	1.67	< 2.23	0.161	681.2	790.6
050709	115.8	I	2.21 ± 0.04	1.03	2.15	0.161	681.2	790.6
050709	172.3	I	< 1.96	0.40	< 4.84	0.161	681.2	790.6
050709	202.6	I	1.11 ± 0.05	0.32	3.48	0.161	681.2	790.6
050709	116.7	K	6.24 ± 5.65	6.28	0.99	0.161	1862.2	2161.2
050724	66.1	V	< 18.00	0.49	< 36.51	0.258	442.9	557.1
050724	27.8	R	57.80 ± 5.00	6.38	9.06	0.258	509.7	641.2
050724	46.7	R	< 27.90	2.92	< 9.55	0.258	509.7	641.2
050724	65.8	R	< 19.30	1.12	< 17.23	0.258	509.7	641.2
050724	27.7	I	48.50 ± 5.69	8.07	6.01	0.258	628.5	790.6
050724	29.2	I	< 157.00	7.73	< 20.31	0.258	628.5	790.6
050724	66.1	I	5.69 ± 2.07	2.34	2.43	0.258	628.5	790.6
050724	27.7	K	< 93.10	7.93	< 11.74	0.258	1718.0	2161.2
051221A	17.4	r*	203.00 ± 15.50	7.93	25.60	0.546	404.8	625.9
051221A	33.4	r*	75.60 ± 8.95	2.34	32.31	0.546	404.8	625.9
051221A	49.0	r*	76.50 ± 22.80	1.00	76.50	0.546	404.8	625.9
051221A	80.0	r*	40.70 ± 8.95	0.15	276.87	0.546	404.8	625.9
051221A	95.6	r*	< 44.70	0.10	< 470.03	0.546	404.8	625.9

Continued on next page

Table A1 – continued from previous page

051221A	17.6	i*	187.00 ± 43.90	9.86	18.97	0.546	495.2	765.5
051221A	33.0	i*	67.50 ± 26.00	4.31	15.66	0.546	495.2	765.5
051221A	33.2	z*	89.50 ± 38.20	5.78	15.48	0.546	581.2	898.5
060502B	31.7	r*	< 11.50	4.63	< 2.48	0.287	486.3	625.9
060614	18.5	uvm2	60.60 ± 24.60	0.43	140.93	0.125	199.5	224.4
060614	23.0	uvm2	30.40 ± 22.40	0.23	129.36	0.125	199.5	224.4
060614	32.8	uvm2	5.73 ± 1.22	0.06	88.70	0.125	199.5	224.4
060614	76.0	uvm2	< 2.04	0.00	< 1020.00	0.125	199.5	224.4
060614	18.4	uvu	107.00 ± 20.50	3.75	28.53	0.125	307.8	346.3
060614	22.7	uvu	82.90 ± 14.90	2.66	31.17	0.125	307.8	346.3
060614	27.0	uvu	28.50 ± 10.80	1.79	15.92	0.125	307.8	346.3
060614	31.9	uvu	11.00 ± 2.98	0.89	12.40	0.125	307.8	346.3
060614	74.8	uvu	< 7.77	0.03	< 249.84	0.125	307.8	346.3
060614	245.7	uvu	< 1.95	0.01	< 202.70	0.125	307.8	346.3
060614	18.4	B	108.00 ± 30.60	7.21	14.98	0.125	387.4	435.8
060614	22.7	B	95.20 ± 22.50	5.33	17.86	0.125	387.4	435.8
060614	27.0	B	72.20 ± 20.40	3.90	18.51	0.125	387.4	435.8
060614	32.0	B	< 15.60	2.48	< 6.29	0.125	387.4	435.8
060614	74.8	B	< 13.00	0.17	< 76.47	0.125	387.4	435.8
060614	224.9	B	< 9.00	0.04	< 223.88	0.125	387.4	435.8
060614	18.5	V	164.00 ± 62.30	9.46	17.34	0.125	495.2	557.1
060614	22.9	V	< 107.00	7.65	< 13.99	0.125	495.2	557.1
060614	27.2	V	< 107.00	6.19	< 17.29	0.125	495.2	557.1
060614	32.0	V	26.90 ± 9.91	4.66	5.77	0.125	495.2	557.1
060614	36.7	V	42.20 ± 1.18	3.62	11.66	0.125	495.2	557.1
060614	60.5	V	10.60 ± 0.71	1.01	10.49	0.125	495.2	557.1
060614	74.9	V	< 29.50	0.61	< 48.68	0.125	495.2	557.1
060614	82.4	V	5.27 ± 0.45	0.40	13.18	0.125	495.2	557.1
060614	167.0	V	1.73 ± 0.45	0.11	15.18	0.125	495.2	557.1
060614	217.1	V	< 20.40	0.10	< 194.29	0.125	495.2	557.1
060614	12.7	R	206.00 ± 5.78	11.90	17.31	0.125	569.9	641.2
060614	12.8	R	204.00 ± 3.80	11.90	17.14	0.125	569.9	641.2
060614	12.8	R	206.00 ± 3.83	11.90	17.31	0.125	569.9	641.2
060614	12.8	R	201.00 ± 3.73	11.90	16.89	0.125	569.9	641.2
060614	12.8	R	201.00 ± 3.73	11.90	16.89	0.125	569.9	641.2
060614	12.9	R	204.00 ± 3.80	11.90	17.14	0.125	569.9	641.2
060614	12.9	R	199.00 ± 3.70	11.80	16.86	0.125	569.9	641.2
060614	12.9	R	201.00 ± 5.62	11.80	17.03	0.125	569.9	641.2
060614	12.9	R	201.00 ± 3.73	11.80	17.03	0.125	569.9	641.2
060614	14.4	R	201.00 ± 1.86	11.20	17.95	0.125	569.9	641.2
060614	15.8	R	175.00 ± 1.62	10.70	16.36	0.125	569.9	641.2
060614	16.9	R	168.00 ± 1.56	10.30	16.31	0.125	569.9	641.2
060614	17.9	R	155.00 ± 1.43	9.96	15.56	0.125	569.9	641.2
060614	18.6	R	135.00 ± 3.78	9.75	13.85	0.125	569.9	641.2
060614	19.2	R	130.00 ± 2.42	9.53	13.64	0.125	569.9	641.2
060614	19.2	R	138.00 ± 1.27	9.53	14.48	0.125	569.9	641.2
060614	19.3	R	135.00 ± 1.25	9.51	14.20	0.125	569.9	641.2
060614	19.4	R	145.00 ± 1.34	9.48	15.30	0.125	569.9	641.2
060614	19.4	R	130.00 ± 1.20	9.45	13.76	0.125	569.9	641.2
060614	28.6	R	64.00 ± 13.70	6.90	9.28	0.125	569.9	641.2
060614	31.5	R	60.60 ± 16.40	6.23	9.73	0.125	569.9	641.2
060614	36.8	R	48.70 ± 0.91	5.21	9.35	0.125	569.9	641.2
060614	38.0	R	60.20 ± 19.20	5.04	11.94	0.125	569.9	641.2
060614	38.9	R	31.80 ± 1.81	4.91	6.48	0.125	569.9	641.2
060614	39.9	R	38.70 ± 1.08	4.76	8.13	0.125	569.9	641.2
060614	60.6	R	13.30 ± 0.63	1.95	6.82	0.125	569.9	641.2
060614	82.5	R	6.98 ± 0.26	0.91	7.70	0.125	569.9	641.2
060614	103.3	R	4.83 ± 0.27	0.62	7.77	0.125	569.9	641.2
060614	143.8	R	2.44 ± 0.21	0.28	8.65	0.125	569.9	641.2

Continued on next page

Table A1 – continued from previous page

060614	230.7	R	0.76 ± 0.21	0.16	4.69	0.125	569.9	641.2
060614	13.8	I	271.00 ± 26.20	12.90	21.01	0.125	702.8	790.6
060614	37.0	I	50.30 ± 1.89	6.45	7.80	0.125	702.8	790.6
060614	60.8	I	16.00 ± 2.72	3.46	4.62	0.125	702.8	790.6
060614	82.3	I	10.00 ± 0.97	2.09	4.78	0.125	702.8	790.6
060614	167.3	I	2.50 ± 0.51	0.49	5.15	0.125	702.8	790.6
060614	13.8	J	326.00 ± 31.40	9.60	33.96	0.125	1114.3	1253.5
060614	16.4	J	245.00 ± 4.55	9.74	25.15	0.125	1114.3	1253.5
060614	16.1	K	351.00 ± 23.40	6.88	51.02	0.125	1921.1	2161.2
060614	16.2	K	341.00 ± 26.10	6.88	49.56	0.125	1921.1	2161.2
060614	35.8	K	146.00 ± 12.60	7.12	20.51	0.125	1921.1	2161.2
061006	34.6	R	77.40 ± 8.78	3.20	24.19	0.438	446.0	641.2
061006	31.9	I	129.00 ± 8.78	5.76	22.40	0.438	549.9	790.6
061006	41.7	I	134.00 ± 11.40	4.18	32.06	0.438	549.9	790.6
061201	29.8	I	< 2.76	7.97	< 0.35	0.111	711.6	790.6
061201	73.3	I	< 1.91	2.74	< 0.70	0.111	711.6	790.6
070429B	14.2	J	< 900.00	13.10	< 68.70	0.902	659.1	1253.5
070714B	54.9	R	60.20 ± 19.20	0.23	262.88	0.923	333.4	641.2
070714B	12.5	J	< 2140.00	13.90	< 153.96	0.923	651.9	1253.5
070714B	12.5	K	647.00 ± 206.00	9.51	68.03	0.923	1123.9	2161.2
070724A	14.7	I	< 272.00	10.40	< 26.15	0.456	543.0	790.6
070724A	47.0	I	< 235.00	3.32	< 70.78	0.456	543.0	790.6
070724A	81.0	I	< 257.00	0.76	< 336.83	0.456	543.0	790.6
070724A	114.1	I	< 246.00	0.39	< 622.78	0.456	543.0	790.6
070724A	163.3	I	< 742.00	0.17	< 4364.71	0.456	543.0	790.6
070724A	229.1	I	< 293.00	0.13	< 2253.85	0.456	543.0	790.6
070724A	14.7	J	< 482.00	9.55	< 50.47	0.456	861.0	1253.5
070724A	47.0	J	< 428.00	5.72	< 74.83	0.456	861.0	1253.5
070724A	81.0	J	< 1940.00	2.78	< 697.84	0.456	861.0	1253.5
070724A	114.1	J	< 1470.00	1.96	< 750.00	0.456	861.0	1253.5
070724A	163.3	J	< 954.00	0.92	< 1034.71	0.456	861.0	1253.5
070724A	229.2	J	< 902.00	0.40	< 2243.78	0.456	861.0	1253.5
070724A	18.6	K	< 3850.00	9.00	< 427.78	0.456	1484.4	2161.2
070809	23.9	g*	< 11.50	2.65	< 4.34	0.473	325.7	479.8
070809	23.8	R	21.80 ± 6.66	6.32	3.45	0.473	435.3	641.2
071227	21.0	g*	< 9.41	4.22	< 2.23	0.381	347.4	479.8
071227	21.0	r*	< 14.80	7.85	< 1.89	0.381	453.2	625.9
071227	21.0	i*	< 30.70	8.18	< 3.75	0.381	554.3	765.5
071227	21.0	z*	< 25.40	10.10	< 2.51	0.381	650.6	898.5
071227	21.0	J	< 365.00	8.96	< 40.74	0.381	907.7	1253.5
071227	21.0	H	< 913.00	9.75	< 93.64	0.381	1195.8	1651.5
080905A	15.6	r*	< 13.60	9.98	< 1.36	0.122	557.9	625.9
080905A	12.8	R	3.49 ± 1.15	11.90	0.29	0.122	571.6	641.2
080905A	32.1	R	< 1.77	6.14	< 0.29	0.122	571.6	641.2
080905A	15.6	J	< 101.00	9.70	< 10.41	0.122	1117.5	1253.5
090515	17.8	r*	4.00 ± 1.43	9.10	0.44	0.403	446.1	625.9
100625A	23.4	J	< 55.10	8.65	< 6.37	0.452	863.3	1253.5
100816A	26.6	r*	79.50 ± 16.10	2.64	30.11	0.805	346.8	625.9
100816A	53.2	r*	66.10 ± 13.40	0.24	269.80	0.805	346.8	625.9
130603B	28.2	g*	< 6.39	2.38	< 2.68	0.356	353.8	479.8
130603B	23.0	r*	< 10.10	7.14	< 1.41	0.356	461.6	625.9
130603B	23.8	r*	< 15.50	6.82	< 2.27	0.356	461.6	625.9
130603B	28.3	r*	7.06 ± 1.68	5.28	1.34	0.356	461.6	625.9
130603B	23.0	i*	< 19.50	7.59	< 2.57	0.356	564.6	765.5
130603B	28.5	i*	< 16.10	6.35	< 2.54	0.356	564.6	765.5
130603B	28.5	J	< 121.00	8.54	< 14.17	0.356	924.4	1253.5
130603B	164.7	H	5.71 ± 1.01	1.88	3.04	0.356	1217.9	1651.5
140903A	27.5	r*	< 430.00	5.57	< 77.20	0.351	463.3	625.9
140903A	44.4	r*	< 156.00	2.24	< 69.64	0.351	463.3	625.9

Continued on next page

Table A1 – continued from previous page

140903A	79.8	r*	< 89.90	0.34	< 262.10	0.351	463.3	625.9
140903A	29.0	i*	81.40 ± 10.40	6.27	12.98	0.351	566.6	765.5
150101B	35.1	r*	10.10 ± 1.52	4.86	2.08	0.134	551.9	625.9
150101B	56.1	r*	6.25 ± 1.70	1.96	3.19	0.134	551.9	625.9
150101B	226.6	r*	< 3.39	0.14	< 24.04	0.134	551.9	625.9
150101B	203.7	J	< 33.90	1.05	< 32.29	0.134	1105.4	1253.5
150423A	90.2	z*	< 7840.00	0.07	< 114956.00	1.394	375.3	898.5
150424A	21.2	uvu	< 379.00	1.87	< 202.67	0.300	266.4	346.3
150424A	39.7	uvu	< 456.00	0.17	< 2698.22	0.300	266.4	346.3
150424A	169.9	uvu	< 288.00	0.01	< 23801.70	0.300	266.4	346.3
150424A	27.6	B	< 494.00	2.28	< 216.67	0.300	335.2	435.8
150424A	33.4	g*	43.90 ± 4.23	1.42	30.92	0.300	369.1	479.8
150424A	51.0	g*	< 33.90	0.47	< 71.97	0.300	369.1	479.8
150424A	69.1	g*	< 14.80	0.12	< 118.40	0.300	369.1	479.8
150424A	88.0	g*	< 10.20	0.06	< 175.86	0.300	369.1	479.8
150424A	124.6	g*	< 40.80	0.04	< 1108.70	0.300	369.1	479.8
150424A	143.3	g*	< 25.70	0.03	< 823.72	0.300	369.1	479.8
150424A	180.1	g*	< 19.50	0.03	< 693.95	0.300	369.1	479.8
150424A	34.4	V	< 1010.00	2.59	< 389.96	0.300	428.5	557.1
150424A	16.4	r*	157.00 ± 16.70	10.30	15.24	0.300	481.4	625.9
150424A	33.5	r*	53.80 ± 3.58	3.98	13.52	0.300	481.4	625.9
150424A	51.0	r*	< 15.90	1.78	< 8.93	0.300	481.4	625.9
150424A	69.1	r*	24.80 ± 5.57	0.68	36.63	0.300	481.4	625.9
150424A	88.0	r*	< 9.18	0.32	< 28.51	0.300	481.4	625.9
150424A	122.5	r*	3.56 ± 0.20	0.17	20.34	0.300	481.4	625.9
150424A	124.6	r*	< 25.30	0.17	< 148.82	0.300	481.4	625.9
150424A	143.3	r*	< 21.00	0.13	< 165.35	0.300	481.4	625.9
150424A	170.3	r*	1.48 ± 0.20	0.10	14.51	0.300	481.4	625.9
150424A	180.1	r*	< 14.50	0.10	< 142.16	0.300	481.4	625.9
150424A	256.0	r*	0.56 ± 0.23	0.09	6.46	0.300	481.4	625.9
150424A	12.4	i*	239.00 ± 11.30	11.30	21.15	0.300	588.9	765.5
150424A	13.4	i*	241.00 ± 9.04	11.00	21.91	0.300	588.9	765.5
150424A	14.4	i*	212.00 ± 9.98	10.60	20.00	0.300	588.9	765.5
150424A	16.4	i*	199.00 ± 17.20	9.91	20.08	0.300	588.9	765.5
150424A	33.5	i*	55.70 ± 7.09	5.72	9.74	0.300	588.9	765.5
150424A	51.0	i*	< 25.00	3.07	< 8.14	0.300	588.9	765.5
150424A	69.1	i*	< 20.80	1.45	< 14.34	0.300	588.9	765.5
150424A	88.0	i*	< 13.10	0.76	< 17.15	0.300	588.9	765.5
150424A	124.6	i*	< 33.00	0.37	< 88.71	0.300	588.9	765.5
150424A	143.3	i*	< 27.40	0.26	< 105.39	0.300	588.9	765.5
150424A	180.1	i*	< 17.30	0.19	< 92.02	0.300	588.9	765.5
150424A	12.4	z*	274.00 ± 15.60	14.00	19.57	0.300	691.2	898.5
150424A	13.4	z*	247.00 ± 11.70	13.50	18.30	0.300	691.2	898.5
150424A	14.4	z*	222.00 ± 12.60	13.00	17.08	0.300	691.2	898.5
150424A	16.4	z*	< 767.00	12.20	< 62.87	0.300	691.2	898.5
150424A	33.4	z*	80.40 ± 9.40	7.09	11.34	0.300	691.2	898.5
150424A	51.0	z*	< 32.60	4.43	< 7.36	0.300	691.2	898.5
150424A	69.1	z*	< 27.10	2.67	< 10.15	0.300	691.2	898.5
150424A	88.0	z*	< 15.60	1.65	< 9.45	0.300	691.2	898.5
150424A	124.6	z*	< 43.00	0.81	< 53.09	0.300	691.2	898.5
150424A	143.3	z*	< 56.70	0.56	< 100.35	0.300	691.2	898.5
150424A	180.1	z*	< 22.60	0.35	< 63.84	0.300	691.2	898.5
150424A	12.4	J	361.00 ± 69.00	9.36	38.57	0.300	964.3	1253.5
150424A	13.4	J	289.00 ± 55.30	9.38	30.81	0.300	964.3	1253.5
150424A	14.4	J	250.00 ± 58.90	9.40	26.60	0.300	964.3	1253.5
150424A	33.5	J	< 129.00	8.25	< 15.64	0.300	964.3	1253.5
150424A	51.0	J	< 141.00	6.65	< 21.20	0.300	964.3	1253.5
150424A	69.1	J	< 155.00	5.02	< 30.88	0.300	964.3	1253.5
150424A	88.0	J	< 97.60	3.64	< 26.81	0.300	964.3	1253.5

Continued on next page

Table A1 – continued from previous page

150424A	123.2	J	7.06 ± 0.54	2.49	2.84	0.300	964.3	1253.5
150424A	123.7	J	6.75 ± 0.00	2.47	2.73	0.300	964.3	1253.5
150424A	143.4	J	< 129.00	1.77	< 72.88	0.300	964.3	1253.5
150424A	171.0	J	2.64 ± 0.56	1.15	2.30	0.300	964.3	1253.5
150424A	180.1	J	< 97.60	1.00	< 97.60	0.300	964.3	1253.5
150424A	256.6	J	1.55 ± 0.00	0.39	4.02	0.300	964.3	1253.5
150424A	257.1	J	1.31 ± 0.62	0.38	3.43	0.300	964.3	1253.5
150424A	33.5	H	< 203.00	7.84	< 25.89	0.300	1270.3	1651.5
150424A	51.0	H	< 203.00	7.41	< 27.40	0.300	1270.3	1651.5
150424A	69.1	H	< 222.00	6.45	< 34.42	0.300	1270.3	1651.5
150424A	88.0	H	< 140.00	5.12	< 27.34	0.300	1270.3	1651.5
150424A	123.9	H	8.19 ± 0.54	3.62	2.26	0.300	1270.3	1651.5
150424A	143.4	H	< 203.00	2.64	< 76.89	0.300	1270.3	1651.5
150424A	171.7	H	4.10 ± 0.56	1.67	2.46	0.300	1270.3	1651.5
150424A	180.1	H	< 185.00	1.48	< 125.00	0.300	1270.3	1651.5
150424A	257.8	H	1.27 ± 0.64	0.49	2.59	0.300	1270.3	1651.5
150424A	33.5	K	< 557.00	7.00	< 79.57	0.300	1662.5	2161.2
150424A	51.0	K	< 882.00	7.73	< 114.10	0.300	1662.5	2161.2
150424A	69.1	K	< 967.00	7.27	< 133.01	0.300	1662.5	2161.2
150424A	88.0	K	< 610.00	5.94	< 102.69	0.300	1662.5	2161.2
150424A	143.4	K	< 557.00	3.67	< 151.77	0.300	1662.5	2161.2
150424A	180.2	K	< 385.00	2.33	< 165.24	0.300	1662.5	2161.2
160821B	19.7	g*	6.18 ± 0.98	7.14	0.87	0.160	413.6	479.8
160821B	41.8	g*	1.35 ± 0.20	1.56	0.87	0.160	413.6	479.8
160821B	82.6	g*	< 1.44	0.14	< 10.43	0.160	413.6	479.8
160821B	206.9	g*	< 1.20	0.06	< 19.35	0.160	413.6	479.8
160821B	22.1	r*	7.27 ± 1.88	7.84	0.93	0.160	539.5	625.9
160821B	40.3	r*	2.95 ± 0.20	3.94	0.75	0.160	539.5	625.9
160821B	42.0	r*	2.21 ± 0.26	3.73	0.59	0.160	539.5	625.9
160821B	75.4	r*	0.99 ± 0.04	0.85	1.16	0.160	539.5	625.9
160821B	103.1	r*	0.63 ± 0.13	0.42	1.49	0.160	539.5	625.9
160821B	207.2	r*	< 0.82	0.14	< 5.93	0.160	539.5	625.9
160821B	215.1	r*	0.16 ± 0.05	0.13	1.19	0.160	539.5	625.9
160821B	42.1	i*	3.68 ± 0.43	5.41	0.68	0.160	659.9	765.5
160821B	82.7	i*	< 1.17	1.44	< 0.81	0.160	659.9	765.5
160821B	206.6	i*	< 0.98	0.26	< 3.82	0.160	659.9	765.5
160821B	22.6	z*	8.84 ± 2.81	9.53	0.93	0.160	774.6	898.5
160821B	41.2	z*	6.71 ± 1.58	5.90	1.14	0.160	774.6	898.5
160821B	42.3	z*	4.60 ± 0.78	5.78	0.80	0.160	774.6	898.5
160821B	40.5	J	< 6.07	7.86	< 0.77	0.160	1080.7	1253.5
160821B	78.1	J	2.96 ± 0.08	6.06	0.49	0.160	1080.7	1253.5
160821B	217.8	J	0.51 ± 0.10	0.76	0.66	0.160	1080.7	1253.5
160821B	40.2	H	< 7.27	8.08	< 0.90	0.160	1423.7	1651.5
160821B	76.7	H	3.81 ± 0.14	6.76	0.56	0.160	1423.7	1651.5
160821B	216.4	H	0.42 ± 0.13	1.12	0.37	0.160	1423.7	1651.5
160821B	41.0	K	< 11.50	8.05	< 1.43	0.160	1863.2	2161.2
160821B	88.9	K	6.03 ± 2.69	6.65	0.91	0.160	1863.2	2161.2
160821B	169.0	K	< 5.93	3.36	< 1.76	0.160	1863.2	2161.2
160821B	187.6	K	< 6.93	2.65	< 2.62	0.160	1863.2	2161.2
170428A	17.5	r*	< 260.00	8.75	< 29.71	0.454	430.4	625.9
170428A	17.5	Y	< 1210.00	11.80	< 102.54	0.454	617.9	898.5
170428A	17.5	z*	< 924.00	10.60	< 87.17	0.454	617.9	898.5
170428A	17.5	J	< 1910.00	9.24	< 206.71	0.454	862.1	1253.5
170428A	17.5	H	< 2290.00	9.79	< 233.91	0.454	1135.8	1651.5

Table A2: Short GRBs with known redshift in addition to [Fong et al. \(2015\)](#)

GRB	ΔT hours	Telescope/Instr	Filter	mag	Flux density μJy	Gal. Ext. A_V	Refs
50509B	0.37175	1.3m PAIRITEL	J	>19.30	<71.79	0.05	Bloom et al. (2006)
	0.37175	1.3m PAIRITEL	H	>19.50	<59.41		
	0.37175	1.3m PAIRITEL	Ks	>18.95	<98.36		
	0.55656	3.5m WIYN OPTIC i CCD		>20.95	<15.97		
	0.63008	3.5m WIYN OPTIC i CCD		>22.05	<5.80		
	2.35342	3.5m WIYN OPTIC r CCD		>23.84	<1.13		
	2.53008	3.5m WIYN OPTIC r CCD		>23.85	<1.12		
	2.70747	3.5m WIYN OPTIC r CCD		>24.11	<0.88		
	50.0906	Keck I LRIS-B	R	>24.60	<0.56		
	50.0906	Keck I LRIS-B	g	>25.50	<0.25		
	192.133	Keck II ESI	R	>25.10	<0.35		
	0.00828	ROTSE-IIIb	R	>17.21	<502.9		GCN#3382
	0.01828	ROTSE-IIIb	R	>18.59	<141.1		
	0.06947	ROTSE-IIIb	R	>18.68	<129.9		
	0.20753	ROTSE-IIIb	R	>19.42	<65.69		
	0.00878	RAPTOR-S	R	>18.92	<104.1		GCN#3414
	0.02128	RAPTOR-S	R	>20.12	<34.48		
	0.10667	RAPTOR-S	R	>20.92	<16.50		
	0.34528	RAPTOR-S	R	>21.82	<7.20		
	0.72833	RAPTOR-S	R	>21.92	<6.57		
	1.12111	RAPTOR-S	R	>21.72	<7.90		
	0.63692	1.2m Mercator	R	>21.12	<13.73		GCN#3384
	0.17581	0.3m NMS	I	>19.04	<92.06		GCN#3393
	0.31108	0.3m NMS	I	>19.54	<58.09		
	0.23903	Swift UVOT	uvv	>18.96	<101.5		GCN#3397
	0.23583	Swift UVOT	uvb	>20.14	<34.75		
	1.08667	Swift UVOT	uvu	>19.40	<69.38		
	11.5	1.0m ARIES	R	>22.12	<5.46		GCN#3396
	26.025	Keck-I LRIS	R	>25.70	<0.20		GCN#3409
	44.775	ESO/VLT FORS	R	>26.60	<0.07		Hjorth et al. (2005)
	94.455	ESO/VLT FORS	V	>27.50	<0.04		
	190.57	ESO/VLT FORS	V	>25.00	<0.39		
	285.37	ESO/VLT FORS	V	>24.20	<0.81		
	548.295	ESO/VLT FORS	R	>26.70	<0.07		
	549.015	ESO/VLT FORS	V	>27.50	<0.04		
	0.66133	1.2m Mercator MEROPE	R	>21.00	<12.87		Castro-Tirado et al. (2005)
	19.6613	1.2m Mercator MEROPE	R	>22.10	<4.67		
	63.9947	6m BTA SCORPIO	R	>26.00	<0.13		
	234.995	1.5m OSN CCD	I	>21.90	<4.41		
	449.945	2.2m CAHA BUSCA	R	>23.90	<0.89		
	17.3447	3.5m CAHA OMEGA2000	H	>20.20	<8.51		
	19.3613	3.5m CAHA OMEGA2000	K	>18.80	<20.17		
	20.078	3.5m CAHA OMEGA2000	J	>21.20	<5.30		

Continued on next page

Table A2 – continued from previous page

	22.478	3.5m	CAHA	H	>20.50	<6.45		
		OMEGA2000						
	41.828	3.5m	CAHA	J	>20.30	<12.14		
		OMEGA2000						
	89.9113	3.5m	CAHA	H	>20.30	<7.76		
		OMEGA2000						
	162.478	3.5m	CAHA	J	>21.70	<3.34		
		OMEGA2000						
	210.995	3.5m	CAHA	J	>22.20	<2.11		
		OMEGA2000						
	9.94486	Swift/UVOT		uvv	>21.10	<13.89		GCN#3412
	9.72417	Swift/UVOT		uvb	>21.80	<8.19		
	10.6799	Swift/UVOT		uvu	>21.80	<3.11		
	10.65	Swift/UVOT		uvw1	>22.30	<1.14		
	10.5218	Swift/UVOT		uvm2	>22.20	<0.99		
	9.8525	Swift/UVOT		uvw2	>22.70	<0.59		
050709	104.923	VLT FORS1		I	>24.10	<0.58	0.03	Watson et al. (2006)
	135.49	Subaru		K	22.10±0.70	0.96±0.87		
	177.149	1.54m Danish DFOSC		R	>24.10	<0.73		
	418.507	1.54m Danish DFOSC		R	>24.00	<0.80		
	466.886	1.54m Danish DFOSC		R	>23.80	<0.96		
	484.006	VLT FORS2		V	>25.20	<0.31		
	484.289	VLT FORS2		R	>25.00	<0.32		
	485.556	VLT FORS2		I	>23.50	<1.00		
	447.19	HST ACS		F814W	27.81±0.27	(28.38±8.01)×10 ⁻³		Fox et al. (2005)
	29.76	40in Swope		i	>20.50	<23.86		
	27.5	PROMPT-5		R	>21.00	<12.68		GCN#3569
	28.4	0.3m Bronberg		R	>19.50	<50.46		GCN#3571
	44.385	Swift/UVOT		uvv	>21.64	<8.28		GCN#3577
	29.6	PROMPT-5		R	>21.60	<7.29		GCN#3702
	201.05	PROMPT-5		R	>21.60	<7.29		
	159.441	Gemini-N		R	>25.40	<0.22		Jin et al. (2016)
	251.656	VLT FORS1		V	>24.50	<0.60		
	251.506	VLT FORS1		R	>24.60	<0.46		
	58.9231	VLT FORS2		I	24.10±0.20	0.58±0.12		
	200.023	VLT FORS1		I	>24.80	<0.31		
050724	5.6	RTT 150		R	>22.40	<12.14	1.58	Burenin et al. 2005
	58.7	ESO/VLT FORS1		R	>24.40	<1.62		Malesani et al. (2007)
	82.8	ESO/VLT FORS1		R	>24.80	<1.12		
	779.2	ESO/VLT FORS1		R	>25.70	<0.49		
	83.2	ESO/VLT FORS1		V	>25.45	<1.04		
060502B	1	0.8m Xinglong Obs		R	>20.60	<19.44	0.11	GCN#5057
	2.6424	Tautenburg Schmidt Tel.	1.34m	R	>20.20	<28.1		GCN#5062
	0.0886	0.3m AGU Japan		R	>16.00	<1345		GCN#5065
	0.3942	Swift UVOT		uvv	>20.29	<31.05		GCN#5069
	1.1167	Swift UVOT		uvb	>20.62	<26.22		
	1.4182	Swift UVOT		uvu	>21.04	<6.86		
	1.3755	Swift UVOT		uvw1	>21.29	<3.25		
	1.2781	Swift UVOT		uvm2	>21.31	<2.66		
	1.3497	Swift UVOT		uvw2	>21.29	<2.48		
	0.1977	Swift UVOT		uvwhite	>20.49	<13.84		
	0.0886	Moscow Union MASTER	Optic	R	>16.12	<1204		GCN#5073
	0.215	Moscow Union MASTER	Optic	R	>16.26	<1058		
	0.34222	Moscow Union MASTER	Optic	R	>16.00	<1345		

Continued on next page

Table A2 – continued from previous page

	0.4675	Moscow Union	Optic	R	>16.00	<1345	
		MASTER					
	0.5922	Moscow Union	Optic	R	>16.30	<1020	
		MASTER					
	5.68	152 Cassini tel	Loiano	R	>20.60	<19.44	GCN#5074
		BFOSC					
	40.8	Gemini Noth	GMOS	r	>24.70	<0.54	GCN#5077
060614	16.16	1.54m-Danish		R	19.45±0.01	51.81±0.48	0.06 Fynbo et al. (2006)
	17.77	1.54m-Danish		R	19.60±0.01	45.12±0.42	
	19.03	1.54m-Danish		R	19.64±0.01	43.49±0.40	
	20.17	1.54m-Danish		R	19.73±0.01	40.03±0.37	
	21.78	1.54m-Danish		R	19.80±0.01	37.53±0.35	
	21.6	1.54m-Danish		R	19.86±0.01	35.51±0.33	
	21.69	1.54m-Danish		R	19.88±0.01	34.87±0.32	
	21.88	1.54m-Danish		R	19.92±0.01	33.60±0.31	
	43.71	1.54m-Danish		R	21.45±0.06	8.21±0.47	
	7.41	Boyden-Obs.		R	18.58±0.11	115.50±12.31	Xu et al. (2009)
	6.95	Boyden-Obs.		R	18.92±0.17	84.41±14.31	
	9.28	Boyden-Obs.		R	18.96±0.11	81.36±8.68	
	8.81	Boyden-Obs.		R	18.97±0.10	80.61±7.78	
	9.75	Boyden-Obs.		R	19.04±0.11	75.58±8.06	
	7.95	Boyden-Obs.		R	19.33±0.30	57.86±18.42	
	32.12	Boyden-Obs.		R	20.69±0.21	16.53±3.53	
	35.45	Boyden-Obs.		R	20.75±0.26	15.65±4.23	
	15.5	CTIO		I	18.90±0.10	70.06±6.76	GCN#5259
	15.5	CTIO		J	18.20±0.10	84.11±8.12	GCN#5259
	42.72	ESO/VLT		R	20.80±0.30	15.55±4.95	GCN#5271
	335.286	HST		F606W	26.25±0.16	0.12±0.02	Yang et al. (2015)
	762.402	HST		F606W	>27.90	<0.03	
	325.711	HST		F814W	24.77±0.08	0.47±0.04	
	746.365	HST		F814W	>27.30	<0.05	
	1078.95	HST		F814W	>27.40	<0.04	
	18.4752	NTT		J	18.51±0.02	63.22±1.18	Della Valle et al. (2006)
	18.0986	NTT		Ks	17.23±0.07	90.61±6.03	
	18.25	NTT		Ks	17.26±0.08	88.14±6.74	
	40.27	NTT		Ks	18.18±0.09	37.77±3.26	
	5.8248	Siding-Spring		R	18.80±0.10	98.10±9.46	GCN#5258
	4.7232	Siding-Spring		R	19.00±0.10	81.59±7.87	
	1.7112	Siding-Spring		R	19.10±0.10	74.41±7.18	
	3.8592	Siding-Spring		R	19.10±0.10	74.41±7.18	
	2.8512	Siding-Spring		R	19.20±0.10	67.87±6.55	
	0.5304	Siding-Spring		R	19.90±0.20	35.62±7.20	
	0.6288	Siding-Spring		R	19.90±0.20	35.62±7.20	
	0.7272	Siding-Spring		R	19.90±0.20	35.62±7.20	
	0.4296	Siding-Spring		R	20.20±0.30	27.02±8.60	
	2.87903	Swift		uvb	19.48±0.13	65.22±8.30	Mangano et al. (2007)
	6.51472	Swift		uvb	19.52±0.16	62.86±9.98	
	2.96347	Swift		uvb	19.53±0.13	62.29±7.92	
	6.34639	Swift		uvb	19.56±0.14	60.59±8.34	
	3.04736	Swift		uvb	19.58±0.12	59.48±6.95	
	11.3819	Swift		uvb	19.76±0.19	50.40±9.64	
	1.42849	Swift		uvb	19.85±0.21	46.39±9.90	
	15.8465	Swift		uvb	19.93±0.22	43.09±9.68	
	20.6704	Swift		uvb	20.40±0.27	27.95±7.89	
	25.5574	Swift		uvb	20.54±0.23	24.57±5.80	
	30.3786	Swift		uvb	20.84±0.27	18.64±5.26	
	35.9508	Swift		uvb	>22.50	<4.04	
	84.1039	Swift		uvb	>22.70	<3.36	

Continued on next page

Table A2 – continued from previous page

253.072	Swift	uvb	>23.10	<2.33
1.65575	Swift	uvm2	17.78±0.18	50.40±9.09
11.5439	Swift	uvm2	18.66±0.54	22.41±14.44
16.0065	Swift	uvm2	18.76±0.33	20.44±7.26
20.8429	Swift	uvm2	19.05±0.37	15.65±6.35
25.8711	Swift	uvm2	19.80±0.60	7.84±5.79
36.9314	Swift	uvm2	21.61±0.21	1.48±0.32
1.23389	Swift	uvm2	>17.70	<54.25
1188.22	Swift	uvm2	>22.50	<0.65
85.4556	Swift	uvm2	>22.73	<0.53
7.95142	Swift	uvu	18.35±0.10	69.57±6.71
8.00875	Swift	uvu	18.46±0.21	62.86±13.41
6.17722	Swift	uvu	18.49±0.12	61.15±7.15
6.26139	Swift	uvu	18.54±0.11	58.40±6.23
1.76348	Swift	uvu	18.56±0.19	57.33±10.96
6.09306	Swift	uvu	18.57±0.12	56.81±6.64
11.3622	Swift	uvu	18.77±0.17	47.25±8.01
1.37153	Swift	uvu	18.80±0.16	45.96±7.30
15.8269	Swift	uvu	19.31±0.21	28.73±6.13
20.6505	Swift	uvu	19.35±0.19	27.69±5.30
25.5206	Swift	uvu	19.63±0.18	21.40±3.86
30.3411	Swift	uvu	20.79±0.35	7.35±2.80
35.93	Swift	uvu	21.82±0.26	2.85±0.77
84.0911	Swift	uvu	>22.20	<2.01
276.441	Swift	uvu	>23.70	<0.50
4.56994	Swift	uvv	19.25±0.21	72.84±15.54
11.4784	Swift	uvv	19.27±0.28	71.52±21.04
4.65414	Swift	uvv	19.37±0.22	65.22±14.65
1.59907	Swift	uvv	19.39±0.27	64.03±18.08
4.4855	Swift	uvv	19.51±0.25	57.33±14.84
20.7662	Swift	uvv	19.84±0.35	42.31±16.09
36.05	Swift	uvv	21.80±0.34	6.96±2.56
0.07958	Swift	uvv	>19.70	<48.13
15.9428	Swift	uvv	>19.80	<43.89
25.7374	Swift	uvv	>20.30	<27.69
30.5661	Swift	uvv	>20.30	<27.69
84.2886	Swift	uvv	>21.70	<7.63
244.256	Swift	uvv	>22.10	<5.28
1.7127	Swift	uvw1	18.33±0.25	40.03±10.37
7.78097	Swift	uvw1	18.39±0.12	37.88±4.43
5.04369	Swift	uvw1	18.45±0.27	35.84±10.12
1.31486	Swift	uvw1	18.50±0.31	34.23±11.31
11.3508	Swift	uvw1	19.04±0.26	20.82±5.63
15.8145	Swift	uvw1	19.19±0.26	18.13±4.91
20.6449	Swift	uvw1	19.37±0.22	15.36±3.45
25.5021	Swift	uvw1	19.71±0.23	11.23±2.65
30.3203	Swift	uvw1	20.52±0.32	5.33±1.83
36.3711	Swift	uvw1	21.38±0.16	2.41±0.38
84.7292	Swift	uvw1	>22.71	<0.71
254.637	Swift	uvw1	>23.10	<0.49
3.41728	Swift	uvw2	18.11±0.48	35.84±19.93
1.54212	Swift	uvw2	18.27±0.23	30.93±7.30
11.4848	Swift	uvw2	18.76±0.46	19.70±10.39
15.9451	Swift	uvw2	19.67±0.27	8.52±2.40
20.7889	Swift	uvw2	19.79±0.60	7.63±5.63
30.5792	Swift	uvw2	20.59±0.40	3.65±1.63
25.7545	Swift	uvw2	20.61±0.43	3.58±1.74
38.1025	Swift	uvw2	21.44±0.19	1.67±0.32
1189.77	Swift	uvw2	>22.50	<0.63

Continued on next page

Table A2 – continued from previous page

	85.3433	Swift		uvw2	>22.74	<0.50		
	41.5766	VLT		I	20.73±0.04	12.98±0.49		Yang et al. (2015)
	68.3582	VLT		I	21.97±0.17	4.14±0.70		
	92.6016	VLT		I	22.48±0.10	2.59±0.25		
	188.172	VLT		I	23.99±0.20	0.64±0.13		
	571.442	VLT		I	>23.90	<0.70		
	14.4	VLT		R	19.42±0.02	53.26±0.99		Della Valle et al. (2006)
	14.33	VLT		R	19.42±0.03	53.26±1.49		
	14.37	VLT		R	19.43±0.02	52.77±0.98		
	14.48	VLT		R	19.43±0.02	52.77±0.98		
	14.42	VLT		R	19.45±0.02	51.81±0.96		
	14.45	VLT		R	19.45±0.02	51.81±0.96		
	14.55	VLT		R	19.45±0.02	51.81±0.96		
	14.53	VLT		R	19.45±0.03	51.81±1.45		
	14.5	VLT		R	19.46±0.02	51.33±0.95		
	20.88	VLT		R	19.88±0.03	34.87±0.98		
	21.6	VLT		R	19.92±0.02	33.60±0.62		
	41.4199	VLT		R	21.03±0.02	12.58±0.23		Yang et al. (2015)
	44.8738	VLT		R	21.28±0.03	9.99±0.28		
	68.2078	VLT		R	22.44±0.05	3.43±0.16		
	92.8558	VLT		R	23.14±0.04	1.80±0.07		
	116.248	VLT		R	23.54±0.06	1.25±0.07		
	161.78	VLT		R	24.28±0.09	0.63±0.05		
	259.546	VLT		R	25.54±0.26	0.20±0.05		
	354.542	VLT		R	26.35±0.32	0.09±0.03		
	571.319	VLT		R	>24.60	<0.47		
	787.12	VLT		R	>25.40	<0.22		
	1073.66	VLT		R	>26.30	<0.10		
	472.276	VLT		R	>26.30	<0.10		
	41.2882	VLT		V	21.38±0.03	10.90±0.31		
	68.0436	VLT		V	22.88±0.07	2.74±0.18		
	92.6585	VLT		V	23.64±0.09	1.36±0.12		
	187.87	VLT		V	24.85±0.25	0.45±0.12		
	571.191	VLT		V	>24.80	<0.47		
061006	3824.2	VLT FORS1		I	23.05±0.12	2.20±0.26	0.87	D'Avanzo et al. (2009)
	3214.9	VLT ISAAC		K	>21.20	<2.40		
	3322.3	VLT FORS2		B	25.92±0.12	0.49±0.06		
	3705	VLT ISAAC		J	22.00±0.20	3.14±0.63		
	3823.8	VLT FORS1		V	24.56±0.07	1.24±0.08		
061201	393.2	VLT FORS2		I	> 24.80	<0.33	0.20	Stratta et al. (2007)
	321	VLT FORS2		R	> 24.90	<0.39		
	4119.1	VLT FORS2		R	> 25.90	<0.16		
	1.85	Swift/UVOT		uvv	> 21.23	<14.15		
	0.96	Swift/UVOT		uvb	> 21.14	<18.05		
	0.91	Swift/UVOT		uvu	20.86±0.54	9.15±5.89		
	1	Swift/UVOT		uvw2	19.94±0.41	10.47±4.80		
	2.4	Swift/UVOT		uvw1	20.75±0.36	6.30±2.48		
	2.95	Swift/UVOT		uvm2	21.44±0.54	2.98±1.92		
	12.7	Swift/UVOT		uvw1	22.72±0.47	1.03±0.56		
	37.1	Swift/UVOT		uvw1	>22.97	<0.82		
061217	2.8	Magellan Clay	LDSS3	r	>23.2	<2.15		Berger et al. (2007)
061210	0.225	MDM 1.3-m		I	>18.50	<102.8	0.09	GCN#5906
	0.0467	2-m Faulkes N		R	>17.00	<526.8		GCN#5920
070714B	24.7	WHT		R	23.50±0.30	1.61±0.51	0.38	GCN#6630
	105.5	Keck I LRIS		R	25.50±0.30	0.26±0.081		GCN#6652
	24	TNG NICS		K	21.00±0.30	2.75±0.87		GCN#6635
070724A	2.3064	UKIRT UFTI		K	>18.05	<40.18	0.04	Kocevski et al. (2010)

Continued on next page

Table A2 – continued from previous page

2.5368	UKIRT UFTI	J	>19.62	<22.61			
3.048	UKIRT UFTI	H	>18.88	<28.63			
3.1584	UKIRT UFTI	K	>18.35	<30.48			
17.4096	NOT StanCam	i	>23.47	<1.55			
17.7216	NOT StanCam	R	>23.72	<1.04			
18.336	NOT StanCam	B	>21.95	<6.87			
21.3504	1.3m CTIO ANDICAM	J	>20.67	<8.60			
21.3528	1.3m CTIO ANDICAM	I	>21.79	<4.84			
22.2504	VLT FORS2	i	>24.74	<0.48			
27.048	UKIRT UFTI	K	>17.47	<68.54			
68.3712	1.3m CTIO ANDICAM	J	>20.80	<7.63			
68.3712	1.3m CTIO ANDICAM	I	>21.95	<4.18			
117.979	1.3m CTIO ANDICAM	J	>19.16	<34.54			
117.979	1.3m CTIO ANDICAM	I	>21.85	<4.58			
166.164	1.3m CTIO ANDICAM	J	>19.46	<26.20			
166.164	1.3m CTIO ANDICAM	I	>21.90	<4.38			
237.737	1.3m CTIO ANDICAM	J	>19.93	<17.00			
237.737	1.3m CTIO ANDICAM	I	>20.70	<13.22			
333.734	1.3m CTIO ANDICAM	J	>19.99	<16.08			
333.619	1.3m CTIO ANDICAM	I	>21.71	<5.21			
406.534	1.3m CTIO ANDICAM	I	>21.83	<4.67			
434.772	Keck I LRIS	R	>25.10	<0.29			
434.772	Keck I LRIS	g	>23.32	<1.82			
434.93	Keck I LRIS	R	>23.39	<1.41			
434.969	Keck I LRIS	R	>23.26	<1.59			
435.017	Keck I LRIS	R	>25.39	<0.22			
435.137	Keck I LRIS	g	>25.00	<0.39			
435.218	Keck I LRIS	R	>25.37	<0.23			
435.221	Keck I LRIS	g	>25.50	<0.24			
435.413	Keck I LRIS	g	>25.70	<0.20			
435.415	Keck I LRIS	R	>25.44	<0.21			
435.614	Keck I LRIS	R	>25.44	<0.21			
435.614	Keck I LRIS	g	>25.80	<0.18			
435.398	Keck I LRIS	R	>27.40	<0.04			
435.504	Keck I LRIS	g	>26.25	<0.12			
502.198	1.3m CTIO ANDICAM	J	>19.77	<19.70			
502.2	1.3m CTIO ANDICAM	I	>21.33	<7.40			
544.699	NOT StanCam	R	>24.80	<0.38			
573.509	1.3m CTIO ANDICAM	J	>20.00	<15.94			
573.509	1.3m CTIO ANDICAM	I	>21.63	<5.61			
622.378	1.3m CTIO ANDICAM	J	>20.02	<15.64			
622.378	1.3m CTIO ANDICAM	I	>21.67	<5.41			
668.623	1.3m CTIO ANDICAM	J	>20.21	<13.13			
668.623	1.3m CTIO ANDICAM	I	>22.11	<3.61			
0.035	Swift UVOT	uvwhite	>20.40	<13.10	GCN#6660		
0.10597	Swift UVOT	uvv	>19.50	<59.78			
0.77875	Swift UVOT	uvwhite	>21.10	<6.88			
0.85042	Swift UVOT	uvv	>20.00	<37.72			
0.83153	Swift UVOT	uvb	>20.30	<32.00			
0.985	Swift UVOT	uvu	>20.00	<16.00			
0.96722	Swift UVOT	uvw1	>20.40	<6.36			
0.93514	Swift UVOT	uvm2	>20.40	<4.96			
0.89278	Swift UVOT	uvw2	>20.70	<3.58			
0.32	P60	i	>21.50	<9.54	GCN#6664		
0.371	ESO/MPG GROND	g	–	–	Nicuesa Guelbenzu et al. (2012a)		
071227	4.6	REM	R	>17.00	<506.5	0.03	GCN#7149
	4.6	REM	H	>15.50	<643.7		
	0.1852	Swift/UVOT	uvv	>20.46	<24.66		GCN#7150

Continued on next page

Table A2 – continued from previous page

	0.5546	Swift/UVOT	uvb	>21.01	<16.61		
	0.5347	Swift/UVOT	uvu	>20.33	<11.78		
	0.5152	Swift/UVOT	uvw1	>20.17	<7.84		
	0.7093	Swift/UVOT	uvm2	>21.00	<2.85		
	0.5862	Swift/UVOT	uvw2	>20.65	<3.73		
	7.7	Magellan/Baade IMACS	R	>22.30	<3.84		GCN#7151
	4.1575	ESO/MPG GROND	r	>20.60	<21.97		Nicuesa Guelbenzu et al. (2012b)
	4.1575	ESO/MPG GROND	i	>20.00	<37.94		
	4.1575	ESO/MPG GROND	z	>20.40	<26.09		
	4.1575	ESO/MPG GROND	J	>20.00	<37.52		
	4.1575	ESO/MPG GROND	H	>19.80	<44.95		
	4.1575	ESO/MPG GROND	Ks	>19.40	<64.87		
	29	ESO/MPG GROND	g	>25.50	<0.24		
	29	ESO/MPG GROND	r	>25.00	<0.38		
	29	ESO/MPG GROND	i	>24.20	<0.79		
	29	ESO/MPG GROND	z	>24.40	<0.66		
	29	ESO/MPG GROND	J	>21.50	<9.42		
	29	ESO/MPG GROND	H	>20.50	<23.59		
080905A	36	VLT FORS2	R	>25.00	<0.48	0.37	Rowlinson et al. (2010)
	14.3	VLT FORS2	R	24.26±0.31	0.95±0.31		
	8.5	NOT ALFOSC	R	24.04±0.47	1.16±0.63		
090510	6.42417	ESO/MPG GROND	g	22.88±0.56	2.79±1.89	0.06	Nicuesa Guelbenzu et al. (2012b)
	6.56639	ESO/MPG GROND	g	22.9 ±0.36	2.74±1.08		
	6.94	ESO/MPG GROND	g	22.88±0.33	2.79±0.99		
	7.19139	ESO/MPG GROND	g	23.07±0.29	2.35±0.72		
	7.31528	ESO/MPG GROND	g	23.45±0.43	1.65±0.80		
	7.43889	ESO/MPG GROND	g	23.86±0.5	1.13±0.66		
	7.565	ESO/MPG GROND	g	23.54±0.37	1.52±0.62		
	7.68861	ESO/MPG GROND	g	23.41±0.27	1.72±0.48		
	7.8125	ESO/MPG GROND	g	23.61±0.33	1.43±0.51		
	8.06222	ESO/MPG GROND	g	23.52±0.35	1.55 ±0.59		
	8.1875	ESO/MPG GROND	g	23.43±0.31	1.68±0.56		
	8.6875	ESO/MPG GROND	g	23.7 ±0.32	1.31±0.45		
	8.8125	ESO/MPG GROND	g	23.77±0.34	1.23±0.45		
	8.93611	ESO/MPG GROND	g	23.91±0.31	1.08±0.36		
	9.06333	ESO/MPG GROND	g	23.75±0.33	1.25±0.45		
	9.18806	ESO/MPG GROND	g	23.5 ±0.21	1.58±0.34		
	9.54694	ESO/MPG GROND	g	24.46±0.57	0.65±0.45		
	9.67083	ESO/MPG GROND	g	24.19±0.31	0.84±0.28		
	9.79722	ESO/MPG GROND	g	23.9 ±0.31	1.09±0.36		
	9.92083	ESO/MPG GROND	g	24.21±0.43	0.82±0.40		
	6.19417	ESO/MPG GROND	r	22.01±0.38	6.12±2.56		
	6.25083	ESO/MPG GROND	r	22.09±0.38	5.68±2.38		
	6.3175	ESO/MPG GROND	r	22.29±0.33	4.73±1.68		
	6.36972	ESO/MPG GROND	r	22.89±0.57	2.72 ±1.88		
	6.42417	ESO/MPG GROND	r	22.73±0.51	3.15±1.89		
	6.47583	ESO/MPG GROND	r	22.91±0.53	2.67 ±1.68		
	6.6925	ESO/MPG GROND	r	23.03±0.29	2.39±0.73		
	6.81667	ESO/MPG GROND	r	22.49±0.2	3.93±0.80		
	6.94	ESO/MPG GROND	r	22.86±0.31	2.80±0.92		
	7.0675	ESO/MPG GROND	r	22.62±0.23	3.49±0.82		
	7.19139	ESO/MPG GROND	r	22.77±0.24	3.04±0.75		
	7.31528	ESO/MPG GROND	r	23.09±0.32	2.26±0.78		
	7.43889	ESO/MPG GROND	r	22.71±0.24	3.21 ±0.79		
	7.565	ESO/MPG GROND	r	23.05±0.25	2.35±0.61		
	7.68861	ESO/MPG GROND	r	23.26±0.21	1.93±0.41		

Continued on next page

Table A2 – continued from previous page

7.8125	ESO/MPG GROND	r	23.23±0.25	1.99±0.51
7.93583	ESO/MPG GROND	r	23.07±0.24	2.30±0.57
8.06222	ESO/MPG GROND	r	23.3 ±0.31	1.86±0.62
8.1875	ESO/MPG GROND	r	23.17±0.25	2.10±0.54
8.31167	ESO/MPG GROND	r	23.19±0.23	2.06±0.49
8.4375	ESO/MPG GROND	r	23.11±0.21	2.22±0.47
8.56417	ESO/MPG GROND	r	23.01±0.2	2.44±0.49
8.6875	ESO/MPG GROND	r	23.19±0.23	2.06±0.49
8.8125	ESO/MPG GROND	r	23.25±0.23	1.95±0.46
8.93611	ESO/MPG GROND	r	23.48±0.29	1.58 ±0.48
9.06333	ESO/MPG GROND	r	23.38±0.25	1.73±0.45
9.18806	ESO/MPG GROND	r	23.67±0.3	1.33±0.42
9.31222	ESO/MPG GROND	r	23.52±0.27	1.52±0.43
9.54694	ESO/MPG GROND	r	23.51±0.26	1.54±0.42
9.67083	ESO/MPG GROND	r	24.07±0.46	0.92±0.48
9.79722	ESO/MPG GROND	r	23.74±0.32	1.24±0.43
6.28028	ESO/MPG GROND	i	21.85±0.4	7.01±3.12
6.36972	ESO/MPG GROND	i	22.16±0.38	5.27±2.21
6.42417	ESO/MPG GROND	i	21.86±0.35	6.95±2.64
6.47583	ESO/MPG GROND	i	21.81±0.34	7.27±2.68
6.56639	ESO/MPG GROND	i	22.35±0.31	4.42±1.46
6.6925	ESO/MPG GROND	i	22.18±0.2	5.17±1.05
6.81667	ESO/MPG GROND	i	22.79±0.45	2.95 ±1.52
6.94	ESO/MPG GROND	i	22.53±0.33	3.75±1.33
7.0675	ESO/MPG GROND	i	22.86±0.39	2.77±1.20
7.19139	ESO/MPG GROND	i	22.98±0.41	2.48±1.14
7.43889	ESO/MPG GROND	i	23.14±0.27	2.14±0.60
7.565	ESO/MPG GROND	i	22.5 ±0.2	3.85±0.78
7.68861	ESO/MPG GROND	i	22.58±0.18	3.57±0.65
7.8125	ESO/MPG GROND	i	22.81±0.26	2.90±0.78
7.93583	ESO/MPG GROND	i	22.76±0.27	3.03±0.86
8.06222	ESO/MPG GROND	i	22.84±0.26	2.82±0.76
8.1875	ESO/MPG GROND	i	22.97±0.29	2.50±0.77
8.31167	ESO/MPG GROND	i	22.99±0.33	2.45±0.87
8.4375	ESO/MPG GROND	i	23.03±0.29	2.37±0.72
8.56417	ESO/MPG GROND	i	22.91±0.3	2.64±0.84
8.6875	ESO/MPG GROND	i	23.23±0.22	1.97±0.44
8.8125	ESO/MPG GROND	i	23.08±0.2	2.26±0.46
8.93611	ESO/MPG GROND	i	23.58±0.41	1.43±0.65
9.06333	ESO/MPG GROND	i	23.01±0.28	2.41±0.71
9.18806	ESO/MPG GROND	i	23.26±0.29	1.91±0.59
9.31222	ESO/MPG GROND	i	22.99±0.15	2.45±0.36
9.54694	ESO/MPG GROND	i	23.83±0.52	1.13±0.70
9.79722	ESO/MPG GROND	i	23.23±0.29	1.97±0.60
9.92083	ESO/MPG GROND	i	23.9 ±0.57	1.06±0.73
6.19417	ESO/MPG GROND	i	21.73±0.56	7.83 ±5.29
6.2225	ESO/MPG GROND	i	21.27±0.4	11.96±5.33
6.28028	ESO/MPG GROND	i	21.41±0.4	10.51±4.68
6.3175	ESO/MPG GROND	i	21.45±0.28	10.13±2.98
6.56639	ESO/MPG GROND	i	22.09±0.32	5.62 ±1.93
6.6925	ESO/MPG GROND	i	22.4 ±0.45	4.22±2.17
6.94	ESO/MPG GROND	i	22.5 ±0.36	3.85±1.52
7.19139	ESO/MPG GROND	i	22.95±0.45	2.55±1.31
7.31528	ESO/MPG GROND	i	21.95±0.23	6.39±1.51
7.565	ESO/MPG GROND	i	22.55±0.29	3.68±1.13
7.8125	ESO/MPG GROND	i	22.88±0.37	2.72±1.10
7.93583	ESO/MPG GROND	i	22.63±0.31	3.42±1.13
8.06222	ESO/MPG GROND	i	22.26±0.24	4.81±1.19
8.1875	ESO/MPG GROND	i	22.77±0.4	3.00±1.34

Continued on next page

Table A2 – continued from previous page

	8.4375	ESO/MPG GROND	i	22.98±0.4	2.48±1.10		
	8.56417	ESO/MPG GROND	i	22.96±0.46	2.52±1.33		
	8.8125	ESO/MPG GROND	i	22.56±0.23	3.65±0.860		
	9.06333	ESO/MPG GROND	i	23.18±0.46	2.06±1.09		
	9.18806	ESO/MPG GROND	i	23.01±0.29	2.41±0.74		
	9.79722	ESO/MPG GROND	i	23.44±0.43	1.62±0.79		
	9.92083	ESO/MPG GROND	i	23.11±0.41	2.20±1.01		
100816A	0.371	ROTSE-IIIc	R	>16.60	<837.2	0.23	GCN#11103
	0.426	ROTSE-IIIc	R	>18.50	<145.5		
	2.8	TNG DOLORES	R	20.50±0.30	23.06±7.34		GCN#11104
	0.375	MASTER	R	>17.20	<481.8		GCN#11105
	0.407	TAROT	R	19.20±0.30	76.35±24.30		GCN#11106
	8.03	2.1m/McDonald Obs.	i	21.31±0.10	12.73±1.23		GCN#11108
		CQUEAN					
	11	GEMINI-N GMOS	R	22.40±0.30	4.01±1.28		GCN#11109
	0.55	Calar Alto	I	19.90±0.30	30.07±9.57		GCN#11112
	0.1655	Swift UVOT	uvwhite	18.90±0.19	73.07±13.97		GCN#11115
	1.3162	Swift UVOT	uvv	21.56±0.94	10.71±14.74		
	1.5405	Swift UVOT	uvb	21.07±0.35	19.90±7.57		
	1.3069	Swift UVOT	uvu	20.39±0.35	14.66±5.58		
	1.4317	Swift UVOT	uvw1	20.98±0.44	5.37±2.68		
	3.3429	Swift UVOT	uvm2	>21.42	<3.26		
	2.8944	Swift UVOT	uvw2	>22.19	<1.40		
	24.3	NOT ALFOSC	R	23.00±0.10	2.31±0.22		GCN#11120
	13.4	MITSUME	V	>21.00	<18.10		GCN#11126
	13.4	MITSUME	Rc	>20.50	<22.92		
	13.4	MITSUME	I	>19.90	<30.07		
	48	GTC	r	25.00±0.20	0.44±0.09		Pérez-Ramírez et al. (2013)
	96	GTC	r	25.20±0.20	0.37±0.075		
130603B	700	HST	F160W	> 26.90	< 0.07	0.06	Tanvir et al. (2013)
140903A	14.4	Gemini North GMOS	i	21.33±0.05	11.51±0.54	0.088	Troja et al. (2016)
	39.12	Gemini North GMOS	i	22.99±0.13	2.49±0.32		
	12.72	DCT LMI	r	21.63±0.06	8.87±0.50		
	37.2	DCT LMI	r	> 21.2	<13.18		
	60	DCT LMI	r	> 22.3	<4.79		
	107.76	DCT LMI	r	> 22.9	<2.75		
150423A	0.4	ESO/MPG GROND	g	23.20± 0.20	2.01± 0.41	0.03	GCN#17729
	0.4	ESO/MPG GROND	r	23.10± 0.20	2.19± 0.44		
	0.4	ESO/MPG GROND	i	22.50± 0.20	3.78± 0.77		
	0.4	ESO/MPG GROND	z	22.00± 0.20	5.97± 1.21		
	0.4	ESO/MPG GROND	J	19.30± 0.40	71.40±31.80		
	0.4	ESO/MPG GROND	H	> 18.40	<163.1		
	0.4	ESO/MPG GROND	Ks	> 17.50	< 373.1		
	0.0322	KAIT	R	>17.00	<504.9		GCN#19730
	0.9667	ESO/MPG GROND	g	23.20± 0.20	2.01± 0.41		GCN#17732
	0.9667	ESO/MPG GROND	r	23.10± 0.20	2.19± 0.44		
	0.9667	ESO/MPG GROND	i	22.80± 0.20	2.87±0.58		
	0.9667	ESO/MPG GROND	z	22.60± 0.20	3.43± 0.69		
	0.9667	ESO/MPG GROND	J	> 21.60	< 8.58		
	0.9667	ESO/MPG GROND	H	> 21.00	< 14.87		
	0.9667	ESO/MPG GROND	Ks	> 18.50	<148.5		
	4.155	JOHNSON RATIR	r	23.77± 0.23	1.18± 0.28		GCN#17736
	4.155	JOHNSON RATIR	i	23.62± 0.26	1.35± 0.36		
	4.155	JOHNSON RATIR	Zg	> 20.33	<27.76		
	1.5667	ESO/VLT FORS2	Rc	22.80± 0.10	2.38± 0.23		GCN#17738
	0.0205	Swift/UVOT	uvwhite	> 20.80	<8.97		GCN#17739
	0.0794	Swift/UVOT	uvu	> 20.20	<13.19		
	0.0205	Swift/UVOT	uvwhite	> 21.50	< 4.71		

Continued on next page

Table A2 – continued from previous page

	0.1708	Swift /UVOT	uvv	> 20.90	<16.37		
	0.1503	Swift /UVOT	uvb	> 20.90	<18.28		
	0.0794	Swift /UVOT	uvu	> 20.80	<7.59		
	0.1847	Swift /UVOT	uvw1	> 20.90	<3.97		
	1.4022	Swift /UVOT	uvm2	> 20.80	<3.38		
	0.1642	Swift /UVOT	uvw2	> 21.60	<1.54		
	10.6	MITSuME 3colorCCD-cam	g	> 20.80	<18.37		GCN#17742
	10.6	MITSuME 3colorCCD-cam	Rc	> 20.80	<14.99		
	10.6	MITSuME 3colorCCD-cam	I	> 19.90	< 27.54		
	16.0344	WHT ACAM	g	>25.30	<0.29		GCN#17747
	0.5756	Zeiss-1000-East 1-m tel	R	>22.70	<2.65		GCN#17750
	25.355	JOHNSON RATIR	r	> 24.82	<0.45		GCN#17754
	25.355	JOHNSON RATIR	i	> 24.79	<0.46		
	25.355	JOHNSON RATIR	Zg	> 22.07	<5.59		
	6.6	MITSuME 3colorCCD-cam	g	> 19.4	< 66.68		GCN#17763
	6.6	MITSuME 3colorCCD-cam	Rc	> 19.3	<59.69		
	6.6	MITSuME 3colorCCD-cam	I	> 18.4	<109.7		
	216	GMC 2.4-m OT	z	>21.00	<14.99		GCN#17803
150424A	1.6	Keck I LRIS	R	20.00± 0.30	32.52± 10.35	0.06	GCN#17745
	13.2	NOT/ALFOSC	R	20.67± 0.06	17.55± 1.00		GCN#17756
	15.54	ESO/MPG GROND	g	22.00±0.20	6.28± 1.27		GCN#17757
	15.54	ESO/MPG GROND	r	21.60± 0.10	8.92± 0.86		
	15.54	ESO/MPG GROND	i	21.40± 0.10	10.61± 1.02		
	15.54	ESO/MPG GROND	z	21.10± 0.10	13.84± 1.34		
	15.54	ESO/MPG GROND	J	20.40± 0.50	26.12± 15.28		
	15.54	ESO/MPG GROND	H	> 19.90	<41.16		
	21.295	JOHNSON RATIR	r	21.92± 0.11	6.64± 0.71		GCN#17762
	21.295	JOHNSON RATIR	i	21.65± 0.09	8.43± 0.73		GCN#17761
	21.295	JOHNSON RATIR	Zg	> 20.17	< 32.55		
	160.8	HST	J	>25.30	<0.29		GCN#18100
	333.6	HST	J	>26.90	<0.07		
	16.0842	ESO/MPG GROND	g	21.76± 0.04	7.83± 0.29		Knust et al. (2017)
	17.4014	ESO/MPG GROND	g	21.90± 0.03	6.89±0.19		
	18.6881	ESO/MPG GROND	g	21.99± 0.04	6.34±0.24		
	43.3675	ESO/MPG GROND	g	23.32± 0.10	1.86±0.18		
	66.3611	ESO/MPG GROND	g	> 23.60	< 1.44		
	89.7828	ESO/MPG GROND	g	> 24.50	<0.63		
	114.38	ESO/MPG GROND	g	> 24.90	< 0.43		
	161.938	ESO/MPG GROND	g	> 23.40	< 1.73		
	186.296	ESO/MPG GROND	g	> 23.90	<1.09		
	234.094	ESO/MPG GROND	g	> 24.20	< 0.83		
	16.0842	ESO/MPG GROND	r	21.55± 0.03	9.34± 0.26		
	17.4014	ESO/MPG GROND	r	21.60± 0.03	8.92± 0.25		
	18.6881	ESO/MPG GROND	r	21.80± 0.03	7.42± 0.21		
	43.495	ESO/MPG GROND	r	23.08± 0.07	2.28± 0.15		
	66.3611	ESO/MPG GROND	r	> 24.40	<0.68		
	89.7828	ESO/MPG GROND	r	23.92± 0.22	1.05± 0.24		
	114.38	ESO/MPG GROND	r	>25.00	< 0.39		
	161.938	ESO/MPG GROND	r	> 23.90	< 1.07		
	186.359	ESO/MPG GROND	r	> 24.10	< 0.89		
	234.156	ESO/MPG GROND	r	> 24.50	< 0.62		
	16.0842	ESO/MPG GROND	i	21.45± 0.05	10.14± 0.48		
	17.4014	ESO/MPG GROND	i	21.44± 0.04	10.23± 0.38		

Continued on next page

Table A2 – continued from previous page

18.715	ESO/MPG GROND	i	21.58± 0.05	8.99± 0.42
43.495	ESO/MPG GROND	i	23.03± 0.13	2.37± 0.30
66.3611	ESO/MPG GROND	i	> 23.90	< 1.06
89.7828	ESO/MPG GROND	i	> 24.10	< 0.88
114.38	ESO/MPG GROND	i	> 24.60	< 0.56
161.938	ESO/MPG GROND	i	> 23.60	< 1.40
186.359	ESO/MPG GROND	i	> 23.80	< 1.16
234.156	ESO/MPG GROND	i	> 24.30	<0.73
16.0842	ESO/MPG GROND	z	21.29± 0.06	11.63± 0.66
17.4014	ESO/MPG GROND	z	21.40± 0.05	10.58±0.49
18.715	ESO/MPG GROND	z	21.52± 0.06	9.400± 0.53
43.4319	ESO/MPG GROND	z	22.62± 0.12	3.414± 0.40
66.3611	ESO/MPG GROND	z	> 23.60	<1.39
89.7828	ESO/MPG GROND	z	> 23.80	< 1.15
114.38	ESO/MPG GROND	z	> 24.40	< 0.66
161.938	ESO/MPG GROND	z	> 23.30	< 1.83
186.359	ESO/MPG GROND	z	> 23.00	< 2.41
234.156	ESO/MPG GROND	z	>24.00	< 0.96
16.0914	ESO/MPG GROND	J	20.98± 0.19	15.32± 2.93
17.4083	ESO/MPG GROND	J	21.22± 0.19	12.29± 2.35
18.7219	ESO/MPG GROND	J	21.38± 0.23	10.60± 2.50
43.5017	ESO/MPG GROND	J	>22.10	< 5.46
66.3678	ESO/MPG GROND	J	>22.00	< 5.99
89.8142	ESO/MPG GROND	J	>21.90	< 6.56
114.386	ESO/MPG GROND	J	> 22.40	< 4.15
186.365	ESO/MPG GROND	J	> 22.10	< 5.46
234.163	ESO/MPG GROND	J	> 22.40	< 4.15
43.5017	ESO/MPG GROND	H	> 21.60	< 8.60
66.3678	ESO/MPG GROND	H	> 21.60	< 8.60
89.8142	ESO/MPG GROND	H	> 21.50	< 9.43
114.386	ESO/MPG GROND	H	> 22.00	< 5.95
186.365	ESO/MPG GROND	H	> 21.60	< 8.60
234.163	ESO/MPG GROND	H	> 21.70	< 7.84
43.565	ESO/MPG GROND	Ks	> 20.50	< 23.63
66.3678	ESO/MPG GROND	Ks	> 20.00	< 37.44
89.7894	ESO/MPG GROND	Ks	> 19.90	< 41.05
114.386	ESO/MPG GROND	Ks	> 20.40	< 25.98
186.365	ESO/MPG GROND	Ks	> 20.50	< 23.63
234.289	ESO/MPG GROND	Ks	> 20.90	< 16.35
0.1211	Swift/UVOT	uvu	> 21.30	<12.21
0.8019	Swift/UVOT	uvu	> 20.80	<19.35
1.7767	Swift/UVOT	uvu	20.56±0.23	24.14±5.60
0.9456	Swift/UVOT	uvu	20.91±0.17	17.49±2.96
12.6642	Swift/UVOT	uvu	> 21.30	<12.21
27.6	Swift/UVOT	uvu	>21.00	<16.10
51.5578	Swift/UVOT	uvu	> 20.80	<19.35
220.91	Swift/UVOT	uvu	> 21.30	<12.21
387.388	Swift/UVOT	uvu	> 22.10	<5.84
0.1844	Swift/UVOT	uvb	> 18.90	<110.1
1.6344	Swift/UVOT	uvb	20.42±0.25	27.15±7.03
1.0094	Swift/UVOT	uvb	> 20.90	<17.45
4.4906	Swift/UVOT	uvb	> 20.50	<25.22
4.4906	Swift/UVOT	uvb	> 21.00	<15.91
35.9467	Swift/UVOT	uvb	> 20.70	<20.98
0.0228	Swift/UVOT	vv	> 17.50	<392.8
0.205	Swift/UVOT	uvv	> 18.00	<247.8
1.2075	Swift/UVOT	uvv	> 19.10	<89.97
1.6061	Swift/UVOT	uvv	> 19.60	<56.77
0.9058	Swift/UVOT	uvv	> 19.80	<47.22

Continued on next page

Table A2 – continued from previous page

3.355	Swift/UVOT	uvv	> 19.90	<43.06			
5.6375	Swift/UVOT	uvv	> 20.10	<35.82			
9.6503	Swift/UVOT	uvv	> 19.90	<43.06			
44.6922	Swift/UVOT	uvv	> 19.90	<43.06			
0.7703	Swift/UVOT	uvw1	> 20.90	<18.16			
4.9817	Swift/UVOT	uvw1	21.27±0.19	12.92±2.47			
11.7344	Swift/UVOT	uvw1	> 22.20	<5.48			
25.7381	Swift/UVOT	uvw1	> 22.10	<6.01			
49.4342	Swift/UVOT	uvw1	> 21.80	<7.93			
207.41	Swift/UVOT	uvw1	> 22.40	<4.56			
364.036	Swift/UVOT	uvw1	> 22.60	<3.79			
0.1983	Swift/UVOT	uvw2	> 19.70	<56.07			
0.9303	Swift/UVOT	uvw2	> 21.20	<14.08			
0.8739	Swift/UVOT	uvw2	> 21.90	<7.39			
3.1444	Swift/UVOT	uvw2	21.65±0.17	9.31±1.58			
8.1253	Swift/UVOT	uvw2	21.89±0.10	7.46±0.72			
35.9161	Swift/UVOT	uvw2	> 22.60	<3.88			
59.8933	Swift/UVOT	uvw2	> 22.50	<4.25			
119.762	Swift/UVOT	uvw2	> 23.10	<2.45			
359.838	Swift/UVOT	uvw2	> 23.20	<2.23			
0.2117	Swift/UVOT	uvm2	> 19.10	<99.97			
1.4636	Swift/UVOT	uvm2	> 21.20	<14.45			
0.9378	Swift/UVOT	uvm2	> 21.70	<9.12			
20.1128	Swift/UVOT	uvm2	> 21.90	<7.58			
48.1072	Swift/UVOT	uvm2	> 22.30	<5.25			
143.458	Swift/UVOT	uvm2	> 22.50	<4.36			
340.146	Swift/UVOT	uvm2	> 22.40	<4.79			
0.0483	Swift/UVOT	uvwhite	21.30±0.23	12.46±2.94			
0.1669	Swift/UVOT	uvwhite	>20.70	<21.65			
0.2472	Swift/UVOT	uvwhite	20.94±0.16	17.36±2.76			
1.4919	Swift/UVOT	uvwhite	20.96±0.15	17.04±2.53			
2.3558	Swift/UVOT	uvwhite	20.93±0.08	17.52±1.34			
2.9342	Swift/UVOT	uvwhite	20.87±0.09	18.51±1.60			
4.7017	Swift/UVOT	uvwhite	21.09±0.10	15.12±1.46			
8.9239	Swift/UVOT	uvwhite	21.02±0.06	16.12±0.92			
81.2894	Swift/UVOT	uvwhite	> 22.80	<3.13			
84.4175	Swift/UVOT	uvwhite	> 22.70	<3.43			
87.4589	Swift/UVOT	uvwhite	> 22.20	<5.44			
93.2061	Swift/UVOT	uvwhite	> 22.30	<4.96			
99.7006	Swift/UVOT	uvwhite	> 22.60	<3.76			
1.5567	Keck I LRIS	g	20.77±0.03	19.49± 0.55			
1.56	Keck I LRIS	Rc	20.66±0.04	21.16±0.79			
159.286	HST WFC3	F606W	26.03±0.06	(151.10±8.59)×10 ⁻³		Jin et al. (2018)	
221.363	HST WFC3	F606W	26.98±0.14	(62.99±8.67)×10 ⁻³			
332.847	HST WFC3	F606W	28.03±0.37	(23.95±9.72)×10 ⁻³			
160.206	HST WFC3	F125W	25.25±0.08	(299.70±22.92)×10 ⁻³			
222.324	HST WFC3	F125W	26.32±0.21	(111.90±23.87)×10 ⁻³			
334.199	HST WFC3	F125W	27.08±0.42	(55.60±26.24)×10 ⁻³			
161.017	HST WFC3	F160W	25.08±0.07	(347.40±23.14)×10 ⁻³			
223.177	HST WFC3	F160W	25.83±0.14	(174.10±23.97)×10 ⁻³			
335.073	HST WFC3	F160W	27.10±0.44	(54.06±27.01)×10 ⁻³			
160410A	0.533	ESO/MPG GROND	g	20.60± 0.10	21.89± 2.11	0.02	GCN#19272
	0.533	ESO/MPG GROND	r	20.50± 0.10	23.86± 2.30		
	0.533	ESO/MPG GROND	i	20.70± 0.10	19.76±1.91		
	0.533	ESO/MPG GROND	z	20.50± 0.20	23.67±4.79		
	0.533	ESO/MPG GROND	J	> 20.00	<37.39		
	0.533	ESO/MPG GROND	H	> 19.60	<53.93		
	0.533	ESO/MPG GROND	Ks	> 18.00	<235.2		
	0.128	ESO/VLT X-shooter	r	20.29± 0.06	28.95±1.65		GCN#19274

Continued on next page

Table A2 – continued from previous page

	0.0253	Swift/UVOT	uvwhite	19.46± 0.10	30.39±2.93		GCN#19275
	1.3519	Swift/UVOT	uvv	> 19.70	<49.09		
	1.1808	Swift/UVOT	uvb	> 20.20	<34.49		
	0.0844	Swift/UVOT	uvu	20.50± 0.20	9.90±2.00		
	1.4658	Swift/UVOT	uvw1	> 20.30	<6.79		
	1.4089	Swift/UVOT	uvm2	> 20.80	<3.31		
	1.295	Swift/UVOT	uvw2	> 20.50	<4.16		
	0.0167	Skynet/CTIO PROMPT	I	17.30± 0.30	301.0±95.8		GCN#19277
	0.1	Skynet/CTIO PROMPT	I	19.40± 0.30	43.50±13.84		
	7.5	GMC 2.4-m OT	R	22.10± 0.20	4.58± 0.93		GCN#19280
	7.1	MITSuME 3colorCCD- cam	g	>19.80	<45.74		GCN#19285
	7.1	MITSuME 3colorCCD- cam	Rc	>19.70	<41.05		
	7.1	MITSuME 3colorCCD- cam	I	>19.10	<57.35		
	0.0078	ESO/TAROT	R	18.40± 0.30	138.30± 44.02		GCN#19287
	0.0128	ESO/TAROT	R	> 18.70	<104.9		
	0.0244	ESO/TAROT	R	> 18.70	< 104.9		
	25.3	UKIRT WFCAM	J	> 20.00	<37.39		GCN#19290
	25.3	UKIRT WFCAM	K	> 19.50	<59.07		
	17.3	NOT ALFOSC	r	24.15± 0.09	0.83± 0.07		GCN#19295
	40.37	NOT ALFOSC	r	> 25.00	<0.38		GCN#19300
	14.6	TLS	I	>21.10	<13.63		GCN#19309
	20.7	CTIO ANDICAM	I	> 20.30	<18.99		GCN#19311
	20.7	CTIO ANDICAM	J	> 17.50	<158.8		
160624A	0.7667	Gemini North GMOS-N	r	>25.50	<0.25	0.07	GCN#19565 (AG)
	3.9	MITSuME 3colorCCD- cam	g	> 20.50	<25.34		GCN#19571
	3.9	MITSuME 3colorCCD- cam	Rc	> 20.10	< 29.49		
	3.9	MITSuME 3colorCCD- cam	I	> 19.30	< 48.78		
	6	1-m Lulin	r	> 22.20	< 5.18		GCN#19575
	0.0214	Swift/UVOT	uvwhite	> 20.80	<9.66		GCN#19576
	0.0802	Swift/UVOT	uvu	> 20.00	<16.84		
	0.0214	Swift/UVOT	uvwhite	> 21.50	< 5.07		
	1.4056	Swift/UVOT	uvv	> 19.50	< 61.82		
	1.2347	Swift/UVOT	uvb	> 20.70	< 23.14		
	0.0802	Swift/UVOT	uvu	> 20.70	< 8.84		
	1.5197	Swift/UVOT	uvw1	> 20.80	< 4.72		
	1.4628	Swift/UVOT	uvm2	> 20.70	< 4.16		
	1.3486	Swift/UVOT	uvw2	> 20.30	< 5.61		
160821B	46.584	GTC	H	>23.80	<1.13	0.04	Troja et al. (2019)
	46.992	GTC	J	>24.00	<0.94		
	47.616	GTC	Ks	>23.30	<1.79		
	48.504	GTC	g*	25.67±0.15	0.21±0.03		
	95.808	GTC	g*	>25.60	<0.22		
	239.952	GTC	g*	>25.80	<0.19		
	1.92	GTC	i*	22.39±0.07	4.22±0.28		
	48.864	GTC	i*	24.56±0.12	0.57±0.07		
	95.928	GTC	i*	>25.80	<0.18		
	239.688	GTC	i*	>26.00	<0.15		
	1.824	GTC	r*	22.67±0.10	3.29±0.32		Troja et al. (2019)
	48.672	GTC	r*	25.12±0.12	0.34±0.04		
	119.64	GTC	r*	26.49±0.20	0.10±0.02		

Continued on next page

Table A2 – continued from previous page

	240.312	GTC	r*	>26.20	<0.13	
	1.992	GTC	z*	22.28±0.06	4.64±0.26	
	49.032	GTC	z*	24.31±0.17	0.71±0.12	
	90.5954	HST	F110W	24.78±0.03	0.46±0.01	Jin et al. (2018)
	252.654	HST	F110W	26.70±0.20	0.08±0.02	
	556.341	HST	F110W	>28.00	<0.02	
	89.0066	HST	F160W	24.50±0.04	0.59±0.02	
	251.065	HST	F160W	26.90±0.30	0.06±0.02	
	557.53	HST	F160W	>27.00	<0.06	
	87.45	HST	F606W	26.00±0.04	0.15±0.01	
	249.508	HST	F606W	28.00±0.30	0.02±0.01	
	555.844	HST	F606W	>27.90	<0.03	
	103.128	KeckI	Ks	24.00±0.40	0.94±0.42	Troja et al. (2019)
	217.608	KeckI	Ks	>23.85	<1.08	Kasliwal et al. (2017b)
	196.008	KeckI	Ks	>24.02	<0.92	
	1.68	NOT	r*	22.52±0.06	3.78±0.21	Lamb et al. (2019)
	1.2	NOT	r*	22.58±0.09	3.57±0.31	
	46.8	NOT	r*	24.81±0.07	0.46±0.03	
	47.76	NOT	z*	23.90±0.23	1.04±0.25	
	1.6392	Swift	uvb	>20.20	<35.44	GCN#19839
	1.4681	Swift	uvm2	>19.50	<11.63	
	1.4111	Swift	uvv	>19.10	<87.08	
	1.5253	Swift	uvw1	>19.60	<13.50	
	1.3542	Swift	uvw2	>20.10	<6.33	
	22.8	TNG	g*	24.02±0.16	0.96±0.15	Lamb et al. (2019)
	25.68	WHT	r*	23.83±0.25	1.13±0.29	Troja et al. (2019)
	26.16	WHT	z*	23.60±0.30	1.38±0.44	
170428A	10.16	2.16-m Xinglong	R	> 21.00	< 12.95	0.06 GCN#21048
	0.2056	Swift/UVOT	uvv	> 20.00	< 38.57	GCN#21049
	0.2328	Swift/UVOT	uvb	> 21.00	< 17.29	
	0.2258	Swift/UVOT	uvu	> 19.50	< 26.23	
	0.2192	Swift/UVOT	uvw1	> 19.50	< 15.25	
	0.2122	Swift/UVOT	uvm2	> 20.10	< 6.98	
	1.22	Swift/UVOT	uvw2	> 20.00	< 7.19	
	1.0667	ESO/MPG GROND	g	21.40± 0.10	10.91± 1.05	GCN#21050
	1.0667	ESO/MPG GROND	r	21.30± 0.10	11.76± 1.14	
	1.0667	ESO/MPG GROND	i	21.10± 0.10	13.98± 1.35	
	1.0667	ESO/MPG GROND	z	21.10± 0.10	13.84± 1.34	
	1.0667	ESO/MPG GROND	J	20.70± 0.20	19.82± 4.01	
	1.0667	ESO/MPG GROND	H	20.90± 0.40	16.39± 7.30	
	1.0667	ESO/MPG GROND	Ks	>20.00	< 37.43	
	25.47	JOHNSON RATIR	r	>22.30	<4.68	GCN#21051
	25.47	JOHNSON RATIR	Zg	>20.90	<16.62	
	25.47	JOHNSON RATIR	Y	>20.60	<21.85	
	25.47	JOHNSON RATIR	J	>20.10	<34.44	
	25.47	JOHNSON RATIR	H	>19.90	<41.16	
	0.0153	ESO/TAROT	R	> 17.50	<325.3	GCN#21052
	0.0314	ESO/TAROT	R	> 18.20	<170.7	
	0.0675	ESO/TAROT	R	> 19.20	<67.96	

Table A3: Rest frame light-curves of **AT2017gfo**

time days	Luminosity [erg/s/Hz]	M _{abs} AB	filter	time days	Luminosity [erg/s/Hz]	M _{abs} AB	filter
0.50	–	–	U	0.50	1.29E+27	–16.16	r
0.64	7.18E+26	–15.52	U	0.64	1.15E+27	–16.03	r
0.99	3.81E+26	–14.83	U	0.99	8.50E+26	–15.70	r
1.49	1.02E+26	–13.40	U	1.49	6.22E+26	–15.36	r
2.43	1.65E+25	–11.42	U	2.43	2.43E+26	–14.35	r
3.47	5.35E+24	–10.20	U	3.47	1.18E+26	–13.56	r
4.41	4.51E+24	–10.01	U	4.41	6.90E+25	–12.98	r
5.45	3.18E+24	–9.64	U	5.45	4.64E+25	–12.54	r
6.44	2.99E+24	–9.57	U	6.44	3.03E+25	–12.08	r
7.43	3.21E+24	–9.65	U	7.43	2.65E+25	–11.94	r
8.42	3.11E+24	–9.61	U	8.42	2.46E+25	–11.86	r
9.41	2.43E+24	–9.34	U	9.41	2.05E+25	–11.66	r
10.40	2.31E+24	–9.29	U	10.40	1.89E+25	–11.57	r
11.39	2.02E+24	–9.14	U	11.39	9.51E+24	–10.82	r
0.50	–	–	B	0.50	1.27E+27	–16.14	i
0.64	1.00E+27	–15.88	B	0.64	1.16E+27	–16.04	i
0.99	6.16E+26	–15.35	B	0.99	9.28E+26	–15.80	i
1.49	2.85E+26	–14.52	B	1.49	6.70E+26	–15.44	i
2.43	6.15E+25	–12.85	B	2.43	3.82E+26	–14.83	i
3.47	2.30E+25	–11.79	B	3.47	2.31E+26	–14.29	i
4.41	1.39E+25	–11.24	B	4.41	1.64E+26	–13.92	i
5.45	1.06E+25	–10.94	B	5.45	1.06E+26	–13.44	i
6.44	7.80E+24	–10.61	B	6.44	6.66E+25	–12.94	i
7.43	7.72E+24	–10.60	B	7.43	5.15E+25	–12.66	i
8.42	7.93E+24	–10.63	B	8.42	3.82E+25	–12.33	i
9.41	7.95E+24	–10.63	B	9.41	3.12E+25	–12.11	i
10.40	7.80E+24	–10.61	B	10.40	2.55E+25	–11.89	i
11.39	6.04E+24	–10.33	B	11.39	1.24E+25	–11.12	i
0.50	1.15E+27	–16.03	V	0.50	9.68E+26	–15.84	z
0.64	1.01E+27	–15.89	V	0.64	9.43E+26	–15.81	z
0.99	7.36E+26	–15.55	V	0.99	8.76E+26	–15.74	z
1.49	5.00E+26	–15.13	V	1.49	7.50E+26	–15.57	z
2.43	1.63E+26	–13.91	V	2.43	4.71E+26	–15.06	z
3.47	6.75E+25	–12.95	V	3.47	2.88E+26	–14.53	z
4.41	4.58E+25	–12.53	V	4.41	2.37E+26	–14.32	z
5.45	2.66E+25	–11.94	V	5.45	1.67E+26	–13.94	z
6.44	1.68E+25	–11.44	V	6.44	1.13E+26	–13.51	z
7.43	1.64E+25	–11.42	V	7.43	8.48E+25	–13.20	z
8.42	1.66E+25	–11.43	V	8.42	6.05E+25	–12.83	z
9.41	1.22E+25	–11.09	V	9.41	4.48E+25	–12.51	z
10.40	1.27E+25	–11.13	V	10.40	3.57E+25	–12.26	z
11.39	8.13E+24	–10.65	V	11.39	1.81E+25	–11.52	z
0.50	1.33E+27	–16.19	R	0.50	9.32E+26	–15.80	J
0.64	1.19E+27	–16.07	R	0.64	9.37E+26	–15.81	J
0.99	8.94E+26	–15.76	R	0.99	9.40E+26	–15.81	J
1.49	6.50E+26	–15.41	R	1.49	7.41E+26	–15.55	J
2.43	2.83E+26	–14.51	R	2.43	6.91E+26	–15.48	J
3.47	1.53E+26	–13.84	R	3.47	5.15E+26	–15.16	J
4.41	9.37E+25	–13.31	R	4.41	4.18E+26	–14.93	J
5.45	5.98E+25	–12.82	R	5.45	3.09E+26	–14.60	J
6.44	3.83E+25	–12.34	R	6.44	1.88E+26	–14.06	J
7.43	3.22E+25	–12.15	R	7.43	1.47E+26	–13.79	J
8.42	2.79E+25	–11.99	R	8.42	1.05E+26	–13.43	J
9.41	2.05E+25	–11.66	R	9.41	7.08E+25	–13.00	J
10.40	2.03E+25	–11.65	R	10.40	5.78E+25	–12.78	J
11.39	1.02E+25	–10.90	R	11.39	2.97E+25	–12.06	J

Continued on next page

Table A3 – continued from previous page

0.50	1.12E+27	-16.01	I	0.50	8.45E+26	-15.70	H
0.64	1.05E+27	-15.93	I	0.64	8.56E+26	-15.71	H
0.99	8.92E+26	-15.76	I	0.99	8.76E+26	-15.74	H
1.49	6.79E+26	-15.46	I	1.49	6.77E+26	-15.46	H
2.43	4.08E+26	-14.91	I	2.43	7.77E+26	-15.61	H
3.47	2.51E+26	-14.38	I	3.47	6.38E+26	-15.39	H
4.41	1.94E+26	-14.10	I	4.41	5.47E+26	-15.22	H
5.45	1.32E+26	-13.68	I	5.45	4.50E+26	-15.01	H
6.44	8.36E+25	-13.19	I	6.44	2.97E+26	-14.56	H
7.43	6.32E+25	-12.88	I	7.43	2.40E+26	-14.33	H
8.42	4.65E+25	-12.55	I	8.42	1.76E+26	-13.99	H
9.41	3.63E+25	-12.28	I	9.41	1.24E+26	-13.61	H
10.40	2.81E+25	-12.00	I	10.40	9.18E+25	-13.29	H
11.39	1.30E+25	-11.17	I	11.39	4.76E+25	-12.57	H
0.50	–	–	g	0.50	5.27E+26	-15.18	K
0.64	1.05E+27	-15.93	g	0.64	5.60E+26	-15.25	K
0.99	6.77E+26	-15.46	g	0.99	6.14E+26	-15.35	K
1.49	3.49E+26	-14.74	g	1.49	5.53E+26	-15.24	K
2.43	8.76E+25	-13.24	g	2.43	6.81E+26	-15.46	K
3.47	3.36E+25	-12.19	g	3.47	6.61E+26	-15.43	K
4.41	2.16E+25	-11.71	g	4.41	5.87E+26	-15.30	K
5.45	1.51E+25	-11.33	g	5.45	6.01E+26	-15.33	K
6.44	9.70E+24	-10.85	g	6.44	4.16E+26	-14.93	K
7.43	9.31E+24	-10.80	g	7.43	3.95E+26	-14.87	K
8.42	1.07E+25	-10.95	g	8.42	3.23E+26	-14.65	K
9.41	9.27E+24	-10.80	g	9.41	2.57E+26	-14.41	K
10.40	9.20E+24	-10.79	g	10.40	2.02E+26	-14.14	K
11.39	6.30E+24	-10.38	g	11.39	1.11E+26	-13.49	K

This paper has been typeset from a $\text{T}_{\text{E}}\text{X}/\text{L}^{\text{A}}\text{T}_{\text{E}}\text{X}$ file prepared by the author.

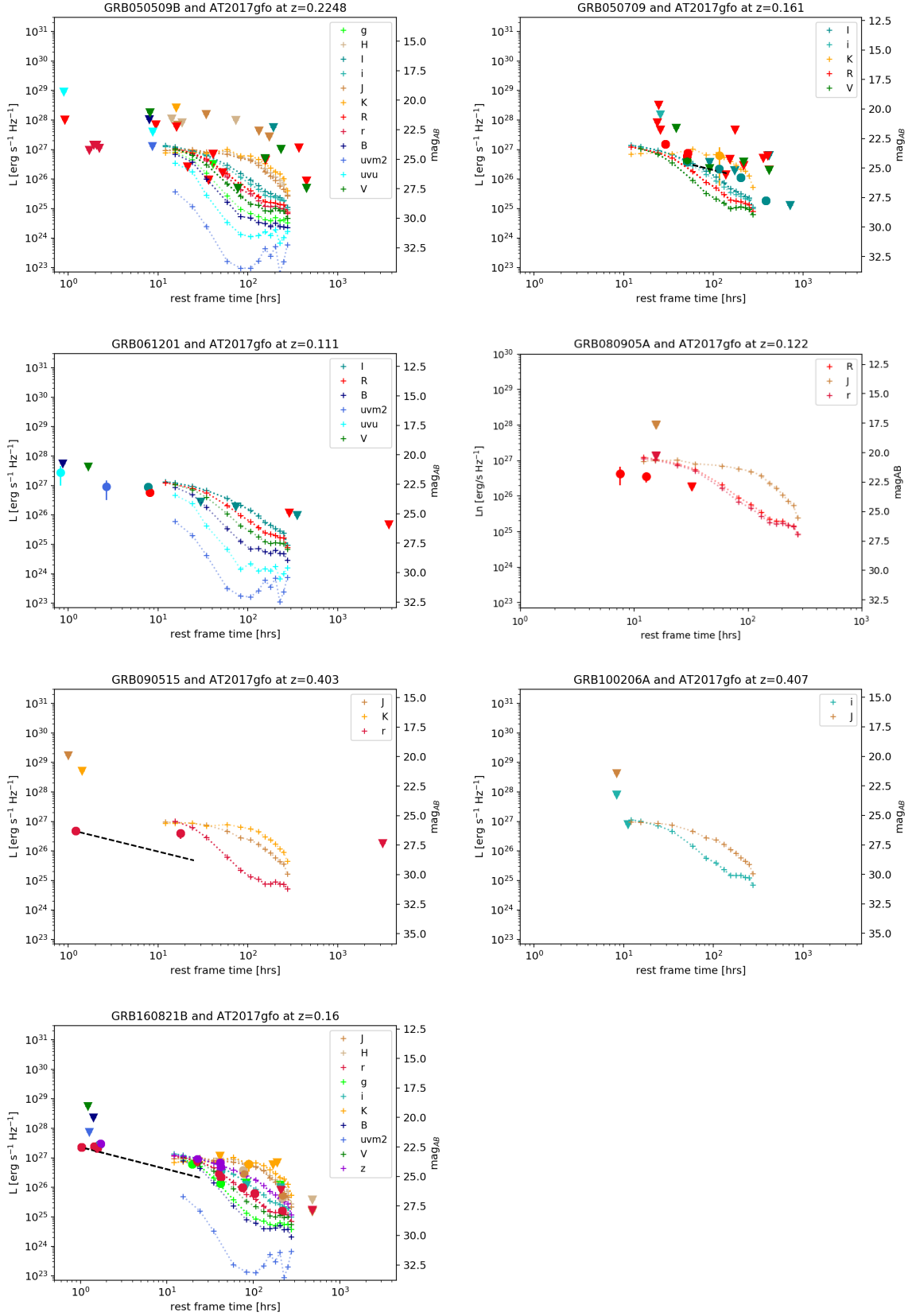


Figure A1. Short GRBs for which the optical counterpart luminosity (circles mark the detections and triangles the upper limits) are fainter than AT2017gfo luminosity (dotted lines with crosses) in at least one effective rest-frame filter (see §3.2). Note that GRB 050709, GRB 090515 and GRB160821B show evidence of a temporal decay index lower than the shallowest index predicted by the fireball model (i.e. $\alpha < 0.75$, see §4.2, black dashed line).

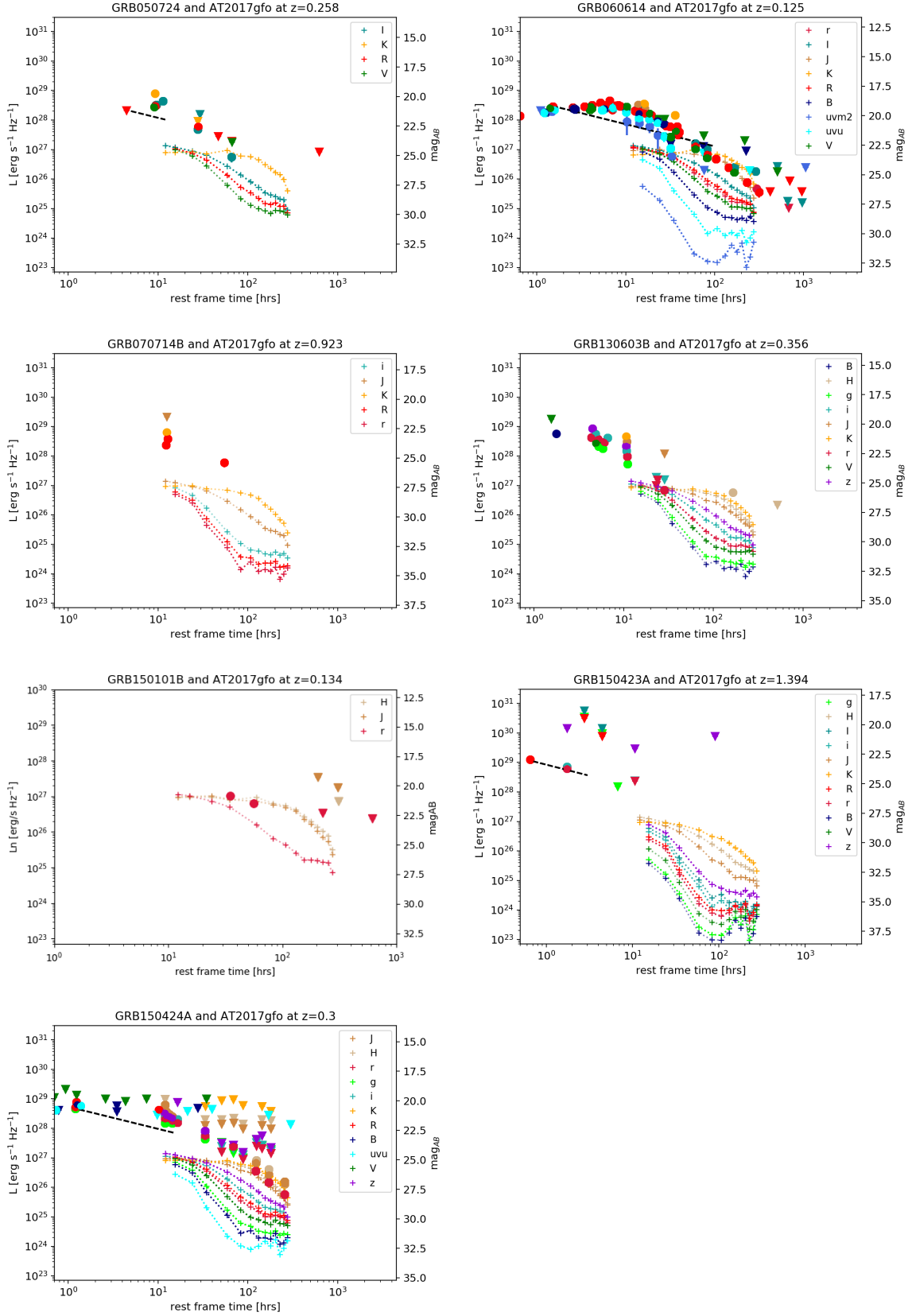


Figure A2. Same as Figure A1 but for GRB optical counterparts for which the luminosity light curves are above the AT2017gfo luminosity in any filter and for which we found evidence of an anomalous shallow decay. If this feature is due to an emerging kilonova emission, from these short GRBs we can infer the upper range of possible kilonova luminosity values (i.e. not just upper limits). We include here also the light curves of GRBs 070714B, 130603B, and 150101B for which a kilonova is claimed in the literature.

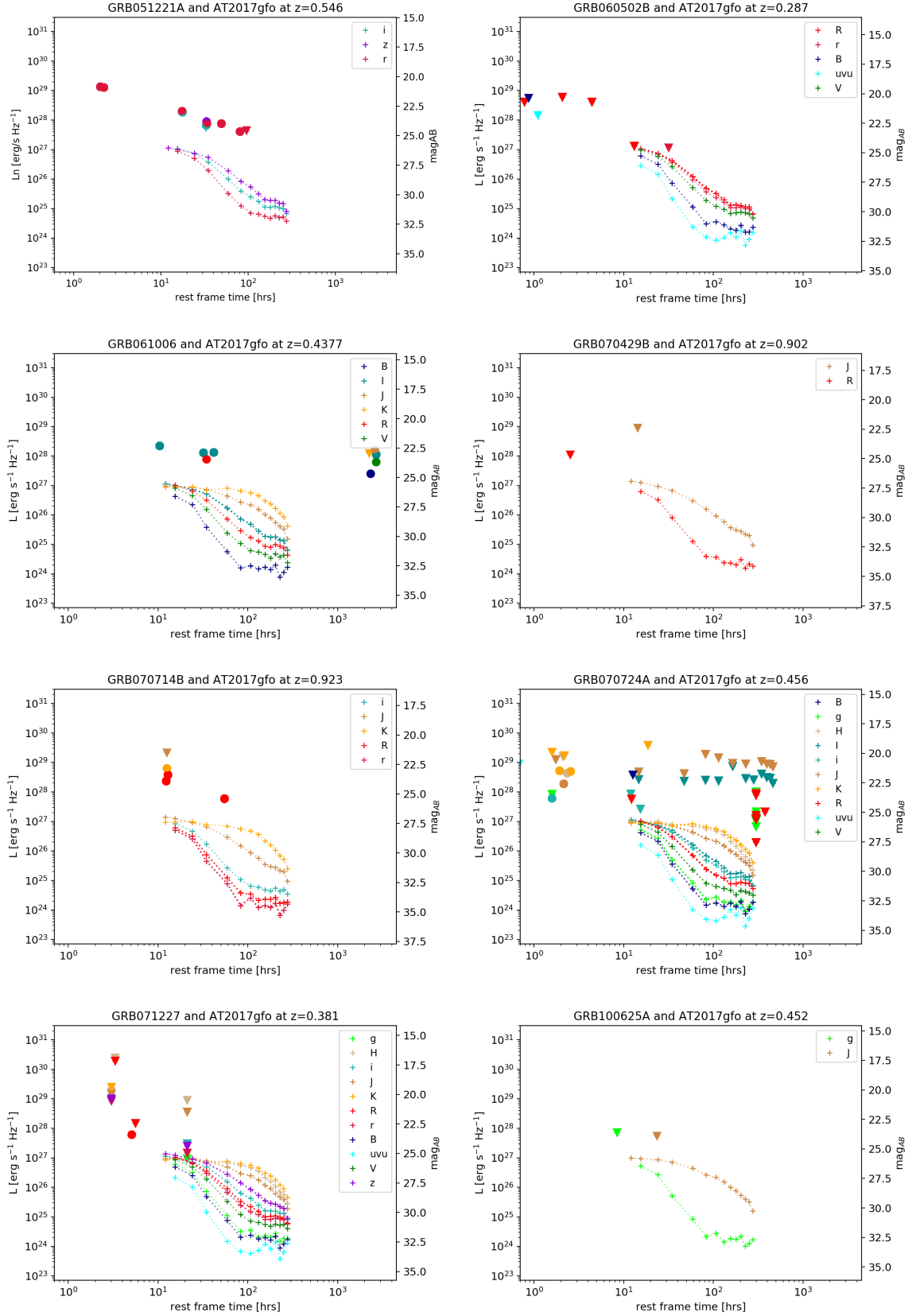


Figure A3. Short GRB optical counterparts for which the luminosity light curves are above the AT2017gfo luminosity in any filter. Circles mark the detections and triangles mark the upper limits, AT2017gfo luminosity is indicated with dotted lines with crosses.

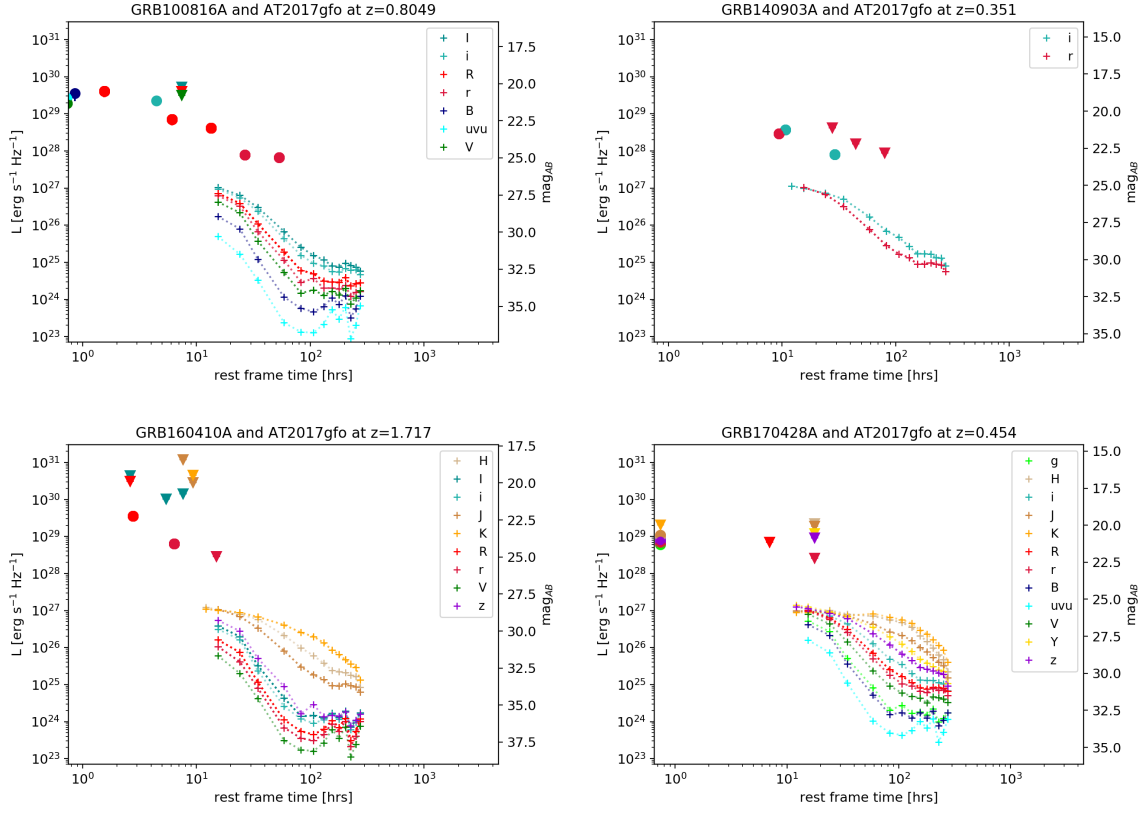


Figure A3 – continued

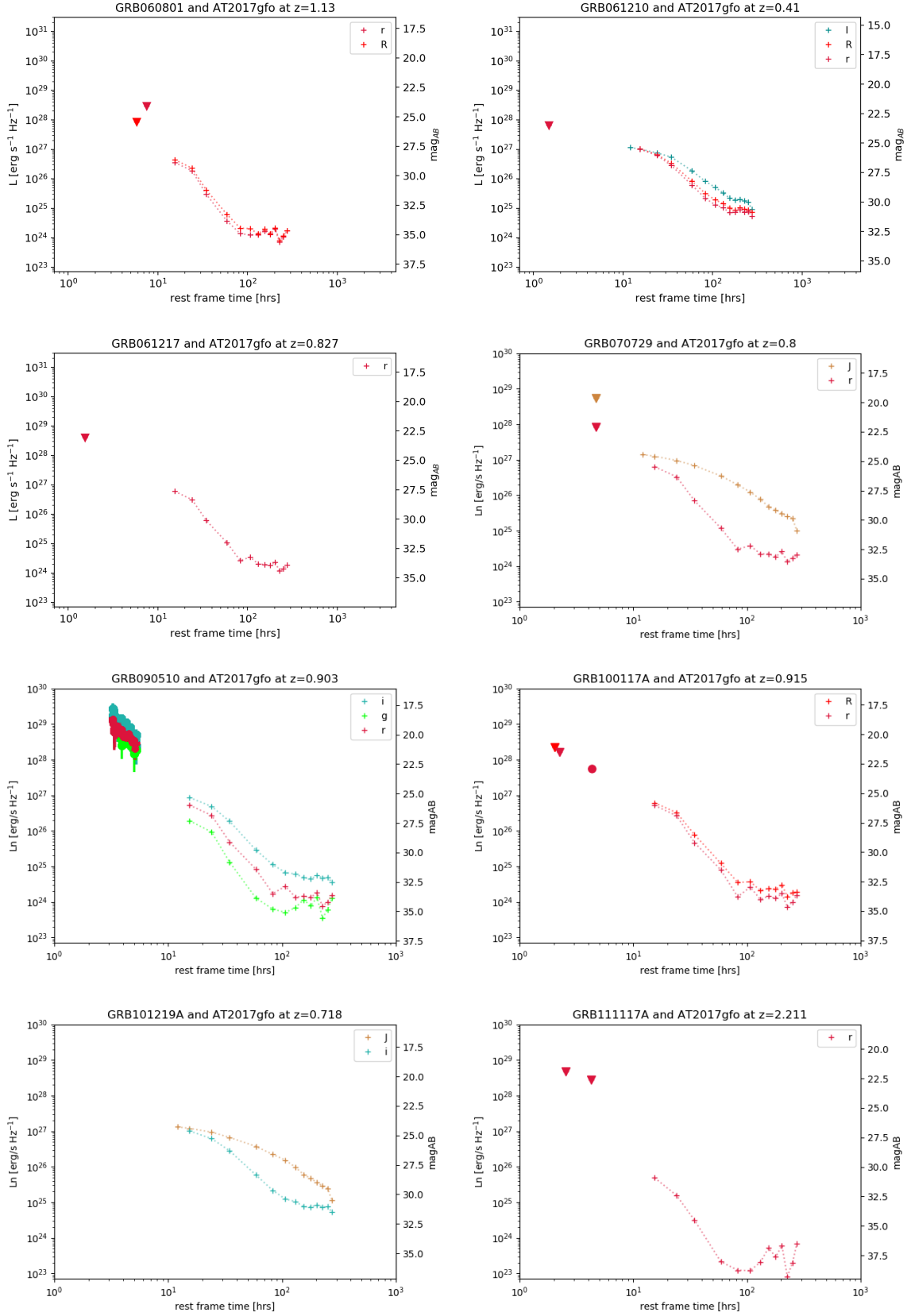


Figure A4. Short GRBs for which no **optical** data fall within the **AT2017gfo** sampled temporal window.

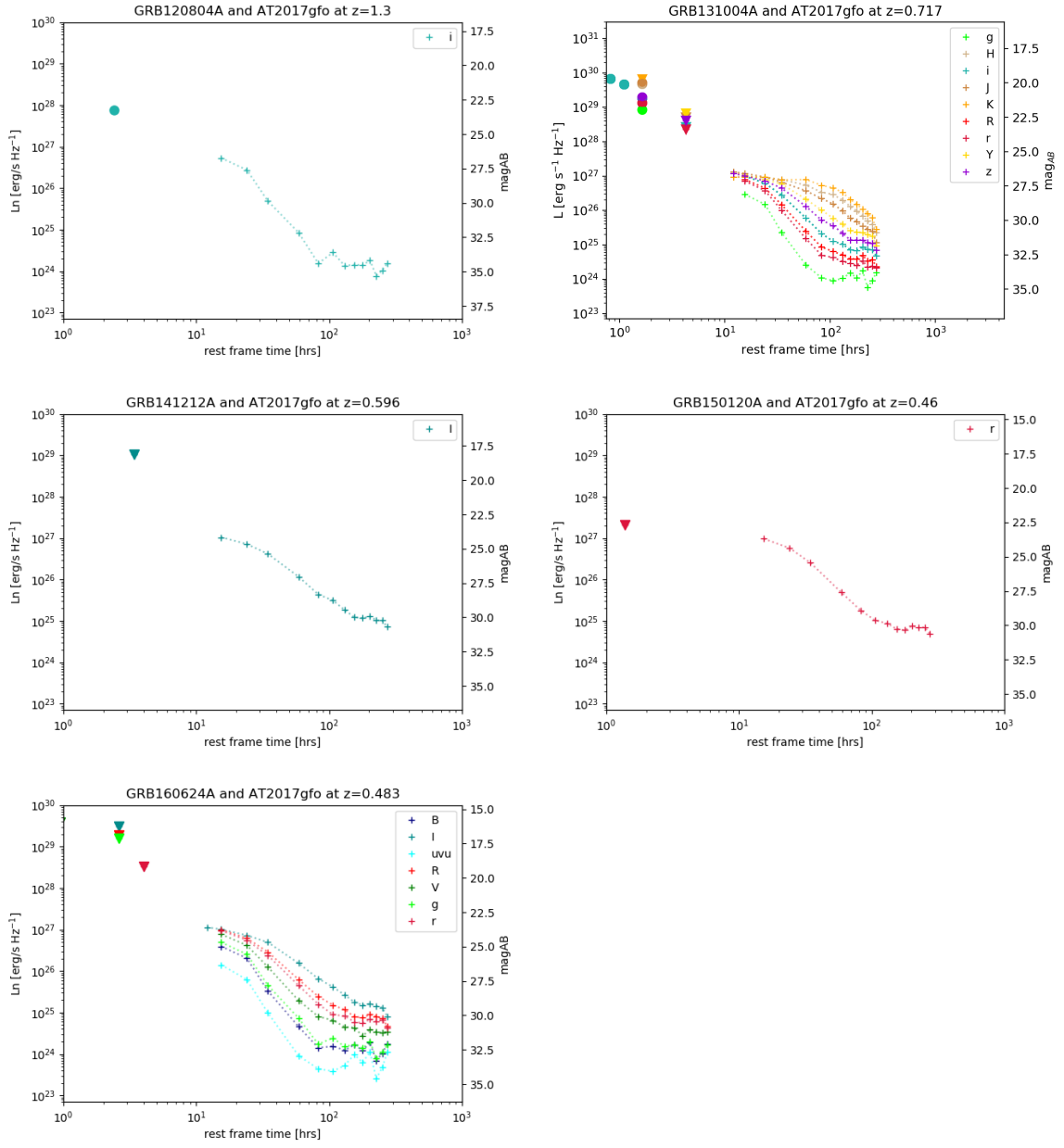


Figure A4 – continued